

INFORMATION TO USERS

This manuscript has been reproduced from the microfilm master. UMI films the text directly from the original or copy submitted. Thus, some thesis and dissertation copies are in typewriter face, while others may be from any type of computer printer.

The quality of this reproduction is dependent upon the quality of the copy submitted. Broken or indistinct print, colored or poor quality illustrations and photographs, print bleedthrough, substandard margins, and improper alignment can adversely affect reproduction.

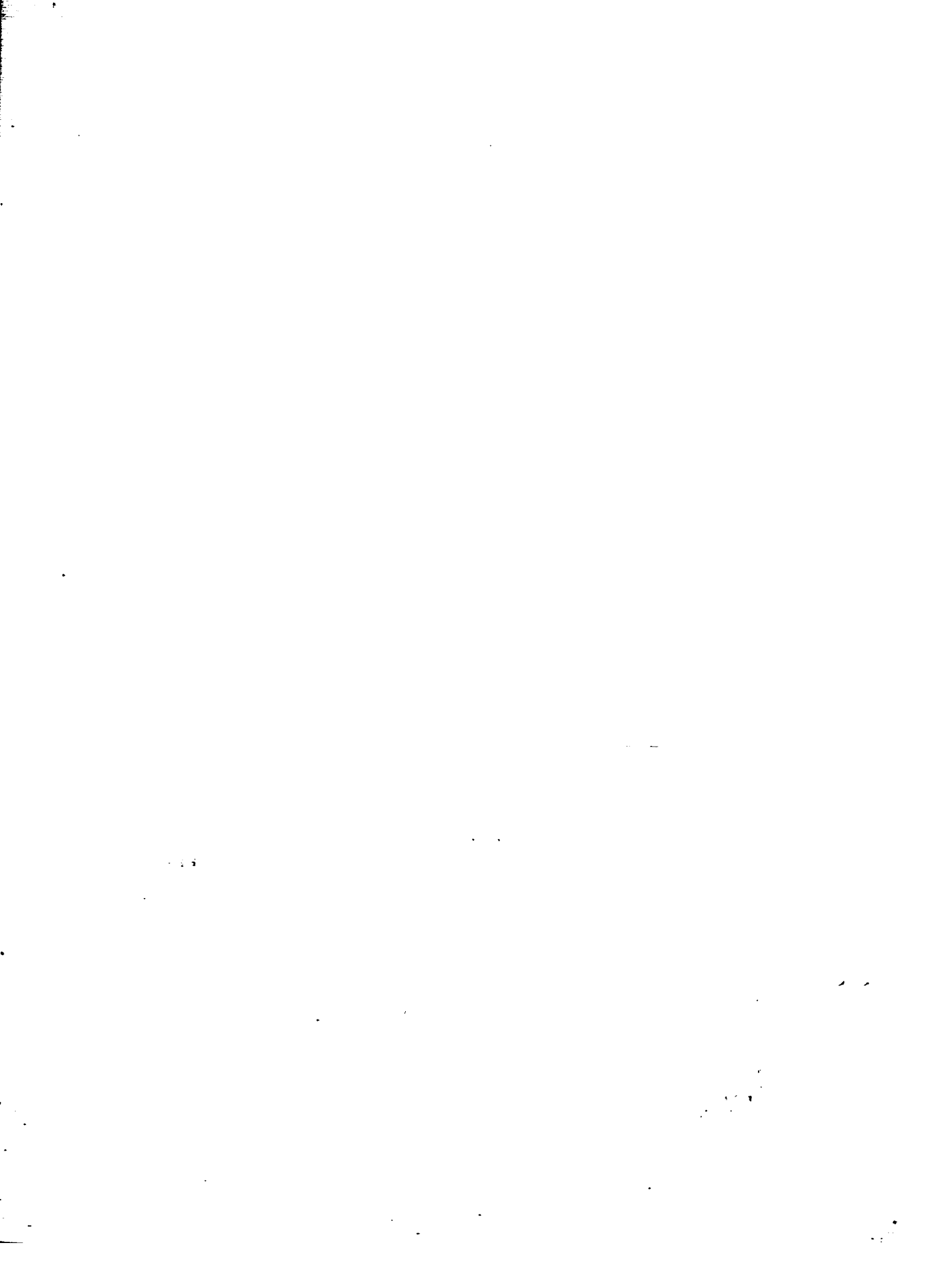
In the unlikely event that the author did not send UMI a complete manuscript and there are missing pages, these will be noted. Also, if unauthorized copyright material had to be removed, a note will indicate the deletion.

Oversize materials (e.g., maps, drawings, charts) are reproduced by sectioning the original, beginning at the upper left-hand corner and continuing from left to right in equal sections with small overlaps. Each original is also photographed in one exposure and is included in reduced form at the back of the book.

Photographs included in the original manuscript have been reproduced xerographically in this copy. Higher quality 6" x 9" black and white photographic prints are available for any photographs or illustrations appearing in this copy for an additional charge. Contact UMI directly to order.

UMI

A Bell & Howell Information Company
300 North Zeeb Road, Ann Arbor MI 48106-1346 USA
313/761-4700 800/521-0600



**UNIVERSITY OF CALIFORNIA
Santa Barbara**

Microcavity Lasers: Coherent Matter and Light

**A dissertation submitted in partial satisfaction
of the requirements of the degree of**

**Doctor of Philosophy
in
Electrical and Computer Engineering**

**by
Rajeev Jagga Ram**

Committee in Charge:

**Professor John E. Bowers, Chairperson
Professor Atac Imamoglu
Professor Herbert Kroemer
Professor Mark Sherwin**

**August 1997
[March 1998]**

UMI Number: 9838442

UMI Microform 9838442
Copyright 1998, by UMI Company. All rights reserved.

**This microform edition is protected against unauthorized
copying under Title 17, United States Code.**

UMI
300 North Zeeb Road
Ann Arbor, MI 48103

The dissertation of Rajeev Jagga Ram
is approved:



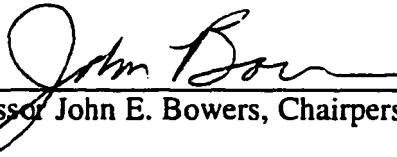
Professor Atac Imamoglu



Professor Herbert Kroemer



Professor Mark Sherwin



Professor John E. Bowers, Chairperson

August 1997

Microcavity Lasers: Coherent Matter and Light

**Copyright © by
Rajeev Jagga Ram
All rights reserved
August 1997**

**Department of Electrical and Computer Engineering
University of California
Santa Barbara, CA 93106**

Acknowledgements

I am sure that I will remember my five years in Santa Barbara as some of my happiest. This vital community of scientists and engineers taught me so much that it is difficult to express the depth of my gratitude. My advisor, John Bowers, showed unwavering support and provided me with resources and intellectual freedom for which I will always be indebted. Evelyn Hu has been a good friend and mentor. Because of her, I have always known where to find a sympathetic ear and a healing dose of enthusiasm. I hope to always count her as one of my closest friends.

I had the good fortune to interact with best engineers and people. I am grateful for discussions with Umesh Mishra on transistor physics, Bob York on radiation theory, and Atac Imamoglu on quantum measurement. They taught me more than science; by example, I learned how to invent, how to teach and how to be unafraid of new ideas. Without Edgard Goobar this thesis would not have been written. I learned from him how to conduct an experiment. Edgard's experiments were always carefully designed, executed with painstaking attention to detail and thoroughly checked and rechecked. I have been fortunate to have such teachers.

For as long as I have known them, I have been bouncing ideas of Ali Shakouri and Holger Schmidt. Our discussions have ranged over the landscape of philosophy and religion, science and methodology, love and death. I have really had fun. I thank Pat Corvini for tennis and long arguments about politics and economics. Daniel Tauber and Mason Thomas for being my oldest friends in Santa Barbara. Alexis Black for being my newest and closest friend. Ron Davis for reminding me about the closeness of art and science. Tom Reynolds, Lance Rushing, Daniel Lasasosa, and Eva Strzelecka were always there to offer help and a friendly ear. There are too many people to whom I owe a debt of friendship.

I would like to thank the National Science Foundation, DARPA, Rome Laboratories, Hewlett-Packard, and the Hertz Foundation for supporting my research.

Most importantly, I must thank my family. They made me secure within myself. Without them I could not have ventured far.

To my teachers,

Vita

January 7, 1970: Born, Hull, United Kingdom
June 1991: B.S., Appl. Physics, California Instit. of Technology
Sept. 1992–Sept. 1996: Research Assistant, UC Santa Barbara
January 1997: Ph.D., Electrical Engineering, UC Santa Barbara

Publications and Conference Presentations

R. J. Ram, L. Yang, K. Nauka, M. Ludowise, Y. M. Houg, D. E. Mars, J. J. Dudley, and S. Y. Wang, "Analysis of Wafer Fusing for 1.3 μ m Vertical Cavity Surface Emitting Lasers", *Applied Physics Letters*, **62**, (1993).

J. J. Dudley, D. I. Babic, R. Mirin, L. Yang, B. I. Miller, R. J. Ram, E. L. Hu and J. E. Bowers, "Low Threshold, Electrically Injected InGaAsP (1.3 μ m) Vertical Cavity Lasers on GaAs Substrates," *IEEE 51st Annual Device Research Conference*, Santa Barbara, California, paper III B (1993).

R. J. Ram, L. Yang, K. Nauka, S. J. Rosner, M. Ludowise, Y. M. Houg, D. E. Mars, J. J. Dudley and S. Y. Wang, "Characterization of Wafer Fusing for Hybrid Optoelectronics," *Electronics Materials Conference*, Santa Barbara, California, paper S2 (1993).

R. J. Ram and R. A. York, "Frequency Conversion and Parametric Oscillation in Linear Active Arrays," *Progress in Electromagnetics Research Symposium*, Pasadena, California, paper 5A7 (1993).

R. A. York and R. J. Ram, "Quasi-Optical Frequency Conversion Arrays," *IEEE/Cornell Conference on Advanced Concepts in High Speed Semiconductor Devices and Circuits*, Ithaca, New York, paper VI (1993).

R. J. Ram, D. I. Babic, R. A. York and J. E. Bowers, "Classical Analysis of Microcavity Lasers," *Optical Society of America Annual Meeting*, Toronto, Ontario, Canada, paper WDDD (1993).

D. I. Babic, R. J. Ram, J. E. Bowers, M. R. Tan and L. Yang, "Transverse Modes in Cavities with Distributed Bragg Reflectors," *Optical Society of America Annual Meeting*, Toronto, Canada, paper MLL (1993).

J. J. Dudley, D. I. Babic, R. Mirin, L. Yang, B. I. Miller, R. J. Ram, E. L. Hu and J. E. Bowers, "Wafer Fused Long-Wavelength Vertical Cavity Lasers," *IEEE Lasers and Electro-Optics Society Annual Meeting*, San Jose, California, paper SCL (1993).

R. J. Ram and R. A. York, "Parametric Oscillation in Nonlinear Dipole Arrays," *IEEE Trans. on Antennas and Propagation*, **42**, (1994).

J. J. Dudley, D. I. Babic, R. Mirin, L. Yang, B. I. Miller, R. J. Ram, T. Reynolds, E. L. Hu, and J. E. Bowers, "Low Threshold, Wafer Fused Long Wavelength Vertical Cavity Lasers," *Applied Physics Letters*, **64**, (1994).

L. Yang, K. Carey, M. Ludowise, W. Perez, D. E. Mars, J. Fouquet, K. Nauka, S. J. Rosner, R. J. Ram, J. J. Dudley, D. I. Babic and J. E. Bowers, "Wafer Bonding of InP and GaAs: Interface Characterization and Device Applications," *InP and Related Materials*, paper (1994).

D. I. Babic, R. J. Ram, J. E. Bowers, M. Tan, L. Yang, "Scaling Laws in Gain Guided Vertical Cavity Lasers," *Applied Physics Letters*, **64**, (1994).

J. E. Bowers, D. I. Babic, J. J. Dudley and R. J. Ram, "Long Wavelength Vertical Cavity Lasers," *Fifth Optoelectronics Conference*, Makuhari Messe, Chiba, Japan, paper 14D3-1 (1994).

J. J. Dudley, D. I. Babic, R. J. Ram, L. Yang, J. E. Bowers, and E. L. Hu, "Long Wavelength Surface Emitting Lasers on GaAs Substrates," *Engineering Foundation Third Conference on High Speed Optoelectronic Devices for Communications and Interconnects*, San Luis Obispo, California, paper__ (1994).

R. J. Ram, D. I. Babic, R. A. York, and J. E. Bowers, "Limitations to Controlling Spontaneous Emission in Microcavities with Distributed Mirrors," *IEEE Semiconductor Laser Conference*, Maui, Hawaii, paper T3.5 (1994).

E. Goobar, R. J. Ram, R. Nagarajan, J. E. Bowers, L. A. Coldren, A. Karlsson, G. Bjork, "Quantum Noise and Facet Correlations in Semiconductor Lasers," *IEEE Semiconductor Laser Conference*, Maui, Hawaii, paper PD1 (1994) & *Quantum Optics*, Davos, Switzerland, paper __ (1994).

A. Imamoglu and R. J. Ram, "Semiconductor Lasers Without Population Inversion," *Optics Letters*, **19**, 1744, (1994).

R. J. Ram, D. I. Babic, R. A. York, and J. E. Bowers, "Spontaneous Emission in Microcavities with Distributed Mirrors," *IEEE Lasers and Electro-Optics Society Annual Meeting*, Boston, Massachusetts, paper _ (invited) (1994).

R. J. Ram, D. I. Babic, R. A. York and J. E. Bowers, "Spontaneous Emission in Microcavities with Distributed Mirrors," *IEEE Journal of Quantum Electronics*, **31**, (1995).

R. J. Ram, E. Goobar, M. Peters, L. A. Coldren, and J. E. Bowers, "Measurements of Spontaneous Emission Factor in Electrically Pumped Microcavity Lasers," *Quantum Optoelectronics Topical Meeting*, Dana Point, California, paper (1995).

R. J. Ram, K. L. Campman, H. Schmidt, A. Imamoglu, A. C. Gossard and J. E. Bowers, "Intersubband Semiconductor Lasers without Population Inversion," *Conference on Lasers and Electro-Optics/Quantum Electronics and Lasers Symposium*, joint session, Baltimore, Maryland, (1995).

R. J. Ram and A. Imamoglu, "The Exciton Boser," *Coherence and Quantum Optics*, Rochester, New York, paper (1995).

E. F. Goobar, R. J. Ram, R. Nagarajan, J. E. Bowers, L. A. Coldren, "Intensity Noise and Facet Correlation in Fabry-Perot Laser Diodes with Low Facet Reflectivities," *Applied Physics Letters*, **68**, (1995).

A. Imamoglu, K. L. Campman, H. Schmidt, R. J. Ram, J. E. Bowers and A. C. Gossard, "Lasers without Inversion in Quantum Well Intersubband Transitions," *International Conference on Coherence and Nonlinear Optics*, St. Petersburg, Russia, paper (invited) (1995).

A. Imamoglu and R. J. Ram, "Condensation Effects in the Exciton Boser," *International Symposium on Quantum Mechanics*, Hatoyama, Japan, paper (1995).

R. J. Ram and A. Imamoglu, "Cooperative Phenomena in Microcavity Excitons: The Exciton Boser," *Quantum Optics in Wavelength Scale Structures*, Cargese, Corsica, paper (1995).

R. J. Ram, J. J. Dudley, J. E. Bowers, L. Yang, K. Carey, S. J. Rosner and K. Nauka, "GaAs to InP Wafer Fusion," *Journal of Applied Physics*, (1995).

R. J. Ram, C.-K. Sun, J. Ko, G. Wang, E. Goobar, M. Oesterich, J. E. Bowers, and A. Imamoglu, "Dynamics of Condensing Polaritons," *Physics of Quantum Electronics, 26th Winter Colloquium on Quantum Electronics*, Snowbird, Utah, (invited) (1996).

R. J. Ram, E. Goobar, M. Peters, L. A. Coldren and J. E. Bowers, "Spontaneous Emission Factor in Post Microcavity Lasers," *Photonics Technology Letters* (1996).

A. Imamoglu and R. J. Ram, "Quantum Dynamics of Exciton Lasers," *Physics Letters A* (1996)

R. J. Ram, R. Sporer, H.-R. Blank, P. Maccarini, H.-C. Chang and R. A. York, "Chaos in Microwave Antenna Arrays," *International Microwave Symposium*, San Francisco, California, paper (invited) (1996).

A. Imamoglu, R. J. Ram, S. Pau, and Y. Yamamoto, "Nonequilibrium Condensates and Lasers Without Inversion," *Physical Review A* (1996).

A.. Imamoglu and R. J. Ram, "From Bose-Einstein Condensation of Excitons to Semiconductor Lasers," *International Quantum Electronics Conference*, Sydney, Australia, paper (invited) (1996).

E. Goobar, R. J. Ram, J. Ko, G. Bjork, M. Oestreich, J.E. Bowers, and A. Imamoglu, "Three Coupled Bosonic Modes in a Microcavity," *International Quantum Electronics Conference*, Sydney, Australia, paper MF3 (1996).

R. J. Ram, C.-K. Sun, J. Ko, G. Wang, E. Goobar, M. Oesterich, J. E. Bowers, and A.. Imamoglu, "Dynamics of Condensing Polaritons," *International Quantum Electronics Conference*, Sydney, Australia, paper MF5 (1996).

Abstract

Microcavity Lasers: Coherent Matter and Light

by

Rajeev Jagga Ram

It has recently become possible to engineer the optical environment of charge carriers in semiconductors thereby strongly altering their interaction with light. This control may allow us to drastically improve the performance of semiconductor lasers. This dissertation reexamines the dynamics of semiconductor lasers in light of this new found control.

Spontaneous light emission seeds the laser oscillator and at the same time bleeds potentially useful energy into nonlasing optical modes. It is the interplay of these two processes that is responsible for the abrupt change in received power from a laser diode below and above threshold. Below threshold light is radiated in all directions and in many colors; only a fraction of this light is captured by a detector. At threshold the photon number builds up so that stimulated light emission becomes the dominant process. The spontaneous emission coupling factor is a measure of this dual role played by spontaneous emission processes; it is equal to the fraction of total spontaneous emission that is radiated into the lasing mode. A simple model is developed to calculate the spontaneous emission factor. The ultimate and expected performance for semiconductor lasers which have nearly all spontaneous emission emitted into the lasing mode is discussed.

When the coupling between the optical field and the electronic system is very large the spontaneous emission process becomes reversible. In semiconductors this occurs when quantum well excitons are placed within a high-finesse microcavity resonator. This system of coupled excitons and photons cannot exhibit electronic inversion or optical gain. Despite the absence of optical gain it is possible for this device to emit coherent light so long as a coherent matter state is developed first. A model for such a matter laser is developed. Finally, low-temperature optical spectroscopy is used to determine the viability of such coherent matter lasers.

Table of Contents

Introduction	1
1.1 Single Mode Lasers.....	1
1.2 Microcavity Lasers.....	6
1.3 Polariton Lasers	11
Controlling Spontaneous Light Emission in Semiconductors.....	13
2.1 Spontaneous Light Emission	13
2.2 Modified Spontaneous Emission.....	21
2.3 Semiconductor Microcavities	28
2.4 Microcavity Exciton-Polaritons.....	44
2.5 Summary.....	52
Semiconductor Microcavity Lasers.....	55
3.1 Microcavity Lasers.....	55
3.2 Spontaneous Emission Factor	58
3.3 Thresholdless Lasers?.....	67
3.4 Limits to Practical Laser Performance	71
3.5 Summary.....	84
Microcavity Polariton Lasers	87
4.1 Polariton Matter Lasers.....	87
4.2 Resonant Polariton Laser.....	91
4.3 Non-resonant Polariton Laser	97

4.4 High-Density Polaritons.....	108
4.5 Summary.....	111
Coherent Matter and Light: Cooperation Between Bosons	115
5.1 Summary of Completed Work.....	115
5.2 The Future Development of the Boser.....	117
5.2 Lasers are Bosers	119
References.....	123

Chapter 1

INTRODUCTION

1.1 Single Mode Lasers

Cable television distribution, and long-distance telephony both rely on the directionality, spectral purity, and intensity of laser light. These applications rely on the build-up of a large number of identical photons in a single optical mode. A laser employs stimulated light emission to 'place' photons in a single mode. Before the onset of stimulated emission (when there are not enough photons nearby), conventional semiconductor devices emit light into many cavity modes. Light from these modes travels in many directions and has a broad frequency spectrum. As more electrons are excited in the semiconductor, the number of emitted photons in the various modes increases. The mode which has the strongest electronic transition and has the smallest optical loss is best at maintaining a large photon number. Furthermore, the emission rate into this mode increases due to stimulated emission. Eventually the photon number in the single mode is so large and the stimulated emission rate so fast that nearly all of the excited electrons relax by emitting identical photons into one mode. The onset of strong stimulated emission is coincident with the increase in directionality and reduction in spectrum associated with single mode emission.

2

Stimulated emission in a laser is not the only way to obtain light in a single mode. The number of optical modes into which excited electrons can emit light is determined by the geometry of the optical cavity and the energy distribution of the excited electrons. In semiconductors, excited electrons are distributed over a range of kinetic energy. The different kinetic energy states correspond to different transition energies; the electron distribution broadens as the temperature and electron density increase. These electrons only emit light if there is an optical mode that is resonant with the electronic transition – if there is a place for the photons to go. The frequency of the optical modes is determined by the size of the optical cavity. Large cavities have many closely spaced modes whereas a very small cavity may support only a single mode. Figure 1.1 shows the transition spectra and optical modes for various cavity sizes and electron distributions. Figure 1.1a shows the mode spacing and transition spectrum for a conventional semiconductor laser. Figure 1.1b and 1.1c both exhibit single mode emission even without stimulated emission. Figure 1.1b has a broad emission spectrum corresponding to emission from free electrons. Figure 1.1c has a narrow emission spectrum characteristic of excitonic emission. These three structures have profoundly different properties. In this section, we describe the conventional semiconductor laser. In Section 1.2, we will introduce semiconductor microcavity lasers. Section 1.3 introduces the polaritons that are formed when excitons couple to a single cavity mode.

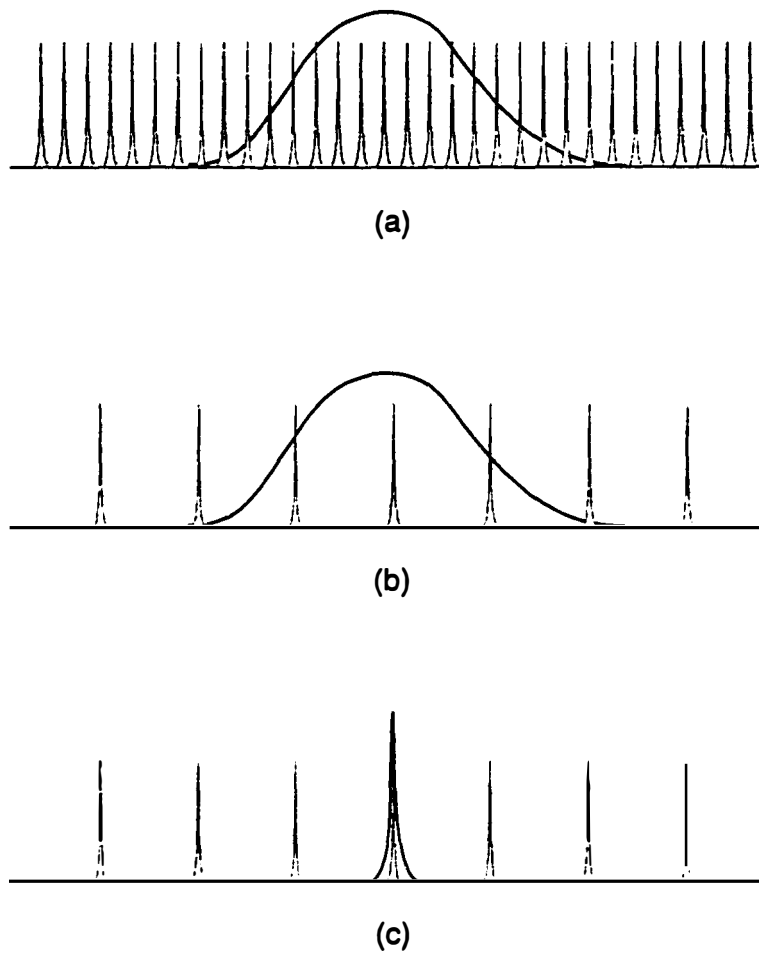


Fig. 1.1 The optical mode distribution and transition spectra for various cavity sizes and electron distributions.

A conventional semiconductor laser structure is shown in Fig.1.2 (Zhao, 1994). The optical cavity is defined by two end mirrors and a waveguide which confines the light as the photons bounce between the mirrors. The cavity length for this laser is $300\mu\text{m}$. The longitudinal mode spacing is 1\AA . The waveguide is

$5\mu\text{m}$ wide and $1\mu\text{m}$ deep. The transverse optical modes are spaced by 10 \AA . The excited electrons in this structure are confined to a thin InGaAs quantum well layer that is inside the optical cavity. Typically, the electrons in the InGaAs quantum well can participate in optical transitions from 950 nm to 990 nm . There are 10^6 optical modes that are accessible to the excited electrons. These include the bound states of the waveguide as well as the radiation modes. A small detector is used to collect the light that leaks out of the optical cavity. Figure 1.3 shows the light power versus the injected current at 77K ; the injected current is responsible for exciting the electrons. The collection efficiency is small when the electrons are relaxing into all 10^6 modes since these photons travel in many different directions once they leave the laser structure and only a few reach the detector. In practice, the change in the measured efficiency is also affected by nonradiative emission processes in which the excited electrons give their energy to the crystal lattice (phonon emission) or to other electrons (Auger), but since we are looking at a low-temperature strained quantum well laser we can ignore these nonradiative effects. The onset of stimulated emission increases the collection efficiency as nearly all of the radiated photons are leaking out of a single cavity mode and therefore travel in the same direction. The abrupt change in the measured efficiency that occurs when we go from multimode to single mode emission defines the laser threshold.

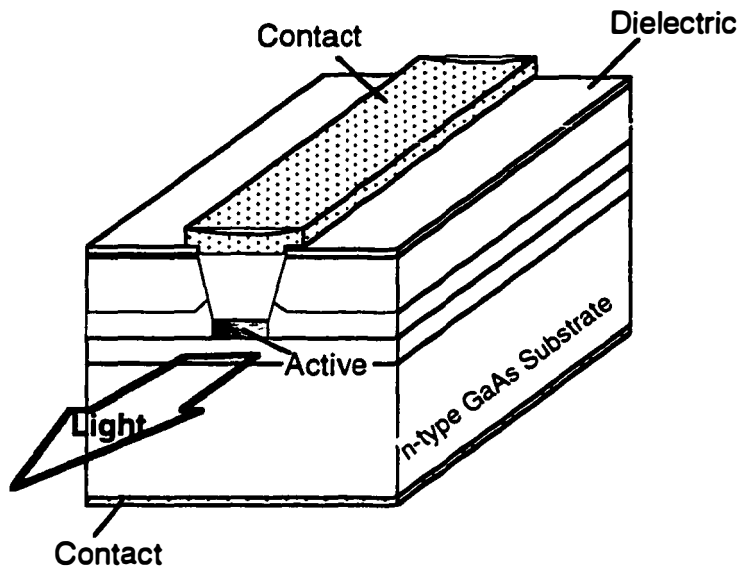


Fig. 1.2. A conventional buried-heterostructure edge-emitting laser structure.

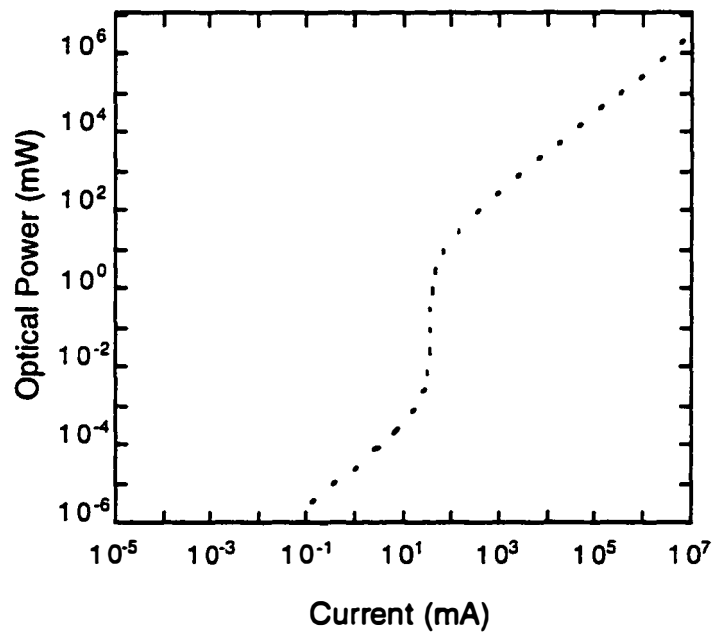


Fig. 1.3. The optical power versus injected current for a conventional buried-heterostructure edge emitting laser operating at 77 K. The figure is based on (Coldren, 1995).

1.2 Microcavity Lasers

Once the optical cavity becomes sufficiently small, only one optical mode is within the emission bandwidth. Figure 1.4 shows the structure that we study in Chapter 3 (Ram, 1996). The optical cavity is defined by two high reflectivity mirrors constructed from multiple GaAs/AlGaAs layers. The cavity length is $0.3\ \mu\text{m}$ or one optical wavelength at the emission wavelength of $0.98\ \mu\text{m}$ for a cavity which has a refractive index of 3.5. The excited electrons are confined to three InGaAs quantum wells in the center of the optical cavity. The longitudinal mode spacing for this short cavity is 90 nm. In this particular structure, the transverse dimension is still large, but the short cavity and transverse waveguide size have effectively limited the number of modes to only 100. The measured light versus injection current is shown in Figure 1.5. The discontinuity at threshold is observed to be smaller than in the conventional semiconductor laser (Fig. 1.3). As the number of optical modes decreases, the collection efficiency at the detector becomes larger. Figure 1.6 shows the optical power versus injected current for various numbers of optical modes within the emission spectrum. For a single mode optical cavity, the collection efficiency is the same before and after the onset of stimulated emission. The change in slope efficiency which is the hallmark of laser action, as it commonly defines laser threshold (DiGiorgio, 1970 and Rice, 1994), does not exist in single mode lasers. The absence of a threshold in a single mode laser is accompanied by a profound change in the electronic interaction with light.

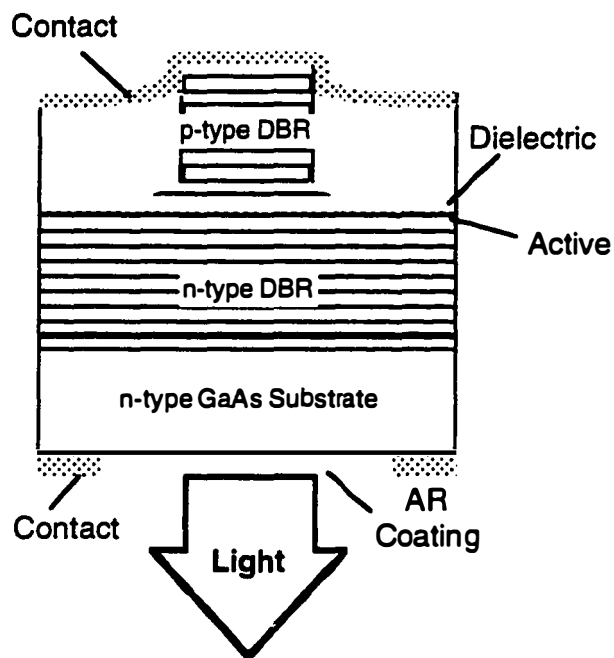


Fig. 1.4 A typical etched-post microcavity laser.

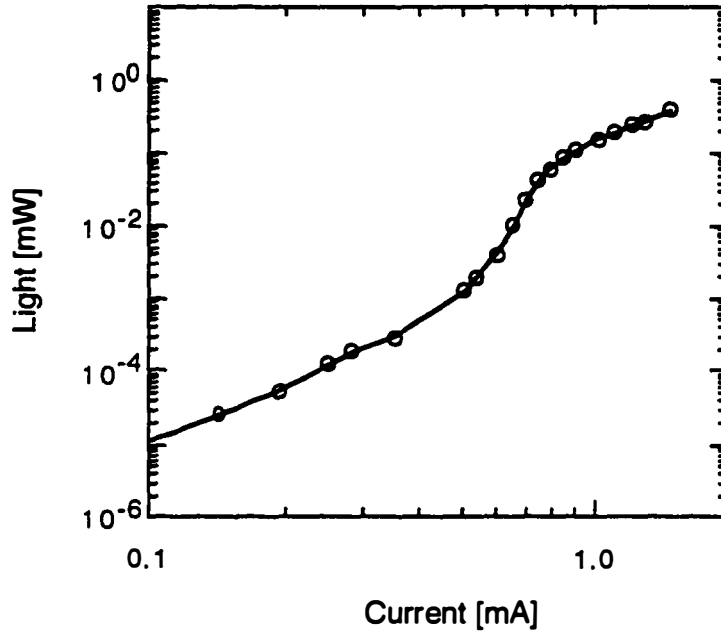


Fig. 1.5 The optical power in the lasing mode versus the injected current for a 9- μm diameter microcavity laser at a heat-sink temperature of 126 K.

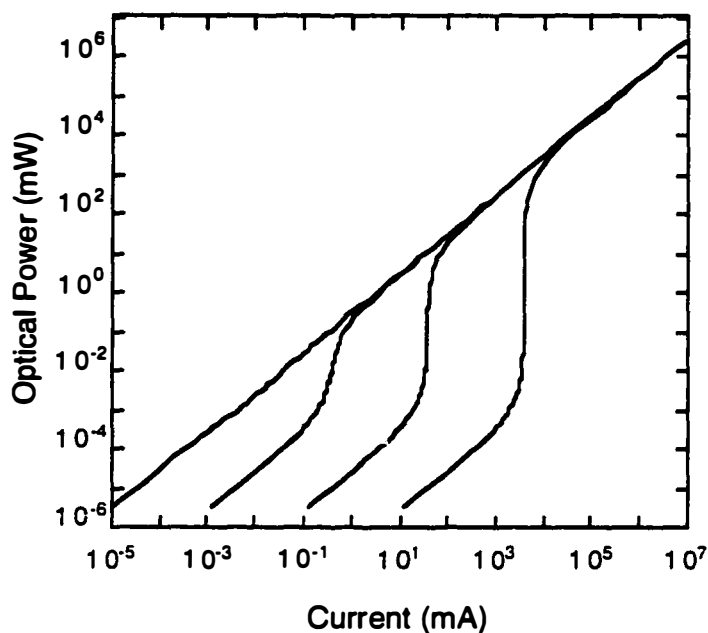


Fig. 1.6 The optical power in the lasing mode versus current for lasers with 10^6 , 10^4 , 10^2 and 1 optical mode. The efficiency changes more drastically as the number of accessible modes becomes larger.

The elimination of absorption is a vivid example of this change. In conventional laser media an incident light beam is absorbed by low energy electrons. The power in the transmitted light beam is observed to decrease as a result of this absorption. This reduction in the incident power occurs because electrons are excited by the light and eventually dissipate this energy by heating the semiconductor or emitting light into other optical modes. In the absence of nonradiative relaxation processes (i.e. no lattice heating), absorption is simply a redistribution of energy out of the incident mode into other optical modes (Loudon, 1992); this redistribution is mediated by the electrons. A single mode

optical cavity has no other modes into which the electrons can scatter the incident light. All of the incident photons, therefore, eventually leave the cavity in the same mode that they entered (again only in the absence of nonradiative relaxation). In steady state, there is no reduction of the incident optical power - no measured absorption. This occurs regardless of the number of excited carriers, i.e. without population inversion.

There is a significant reduction of the threshold current shown in Figure 1.6 as the number of accessible modes decreases (Bjork, 1991). Emission into cavity modes that do not eventually lase is an energy loss process for the excited electrons. This electron loss process requires more pumping in order to build-up a large photon number in the one mode that will lase. In this way, the reduction of cavity size has the same benefits as reducing the nonradiative relaxation rates; both processes improve the efficiency of the laser. However, if these nonradiative processes are very fast, reducing the cavity dimension will not have a significant effect on overall efficiency.

In Chapter 3, we develop a simple formalism for analyzing the optical mode distribution in microcavity semiconductor lasers. A rate equation model which shows a simple method for treating the mode counting problem is developed. Measurements of light versus current on the microcavity structure described above are used to estimate the number of optical modes that the electrons can access. We conclude this chapter with a discussion of nonideal effects such as nonradiative recombination, leakage currents, and optical scattering losses.

1.3 Polariton Lasers

In the microcavity laser, energy is transferred from excited electrons to a single optical mode. However, the excited electrons are more strongly coupled to other electrons with different momenta than to the optical mode - momentum scattering times are typically 1 ps (Wang, 1995) and spontaneous emission times are 5 ns in GaAs. The strong scattering between electrons means that the electron loses phase information about the photons that have previously been radiated. This scattering prevents a coherent exchange of energy back and forth between the excited electron and the cavity mode. Electrons and holes bound together in an exciton recombine much faster than free electrons and holes. For example in GaAs quantum wells, the exciton spontaneous emission rate is 20-40 ps (Andreani, 1991). This strong coupling between exciton and photon is measurable as an enhanced absorption. The photons in the microcavity are reabsorbed before the excitons lose their phase memory and before the photon leaks out of the cavity. This allows a coherent exchange of energy between the excitons and the cavity mode. This system of coupled excitons and photons is called a polariton (Weisbuch, 1992).

In the strong coupling microcavity, the cavity photon exists only as part of a polariton. Laser action requires the build-up of photon populations by stimulated emission of polaritons (Imamoglu, 1996). Since these polaritons are also part exciton they have a nonzero rest mass. The collection of a large number of massive particles in a single quantum state is analogous to the Bose-Einstein condensation. In Chapter 4, we present a semiclassical analysis of these matter lasers. We conclude with a discussion of laser action in a microcavity that

exhibits strong coupling. The microcavity structure used to study the high-density dynamics of polaritons is shown in Fig. 1.7. The structure is similar to the microcavity laser structure in Chapter 3 and Fig.4. Both the matter laser and microcavity laser are realized in very similar structures. Determining whether the device is a matter laser or an optical laser is the experimenter's dilemma.

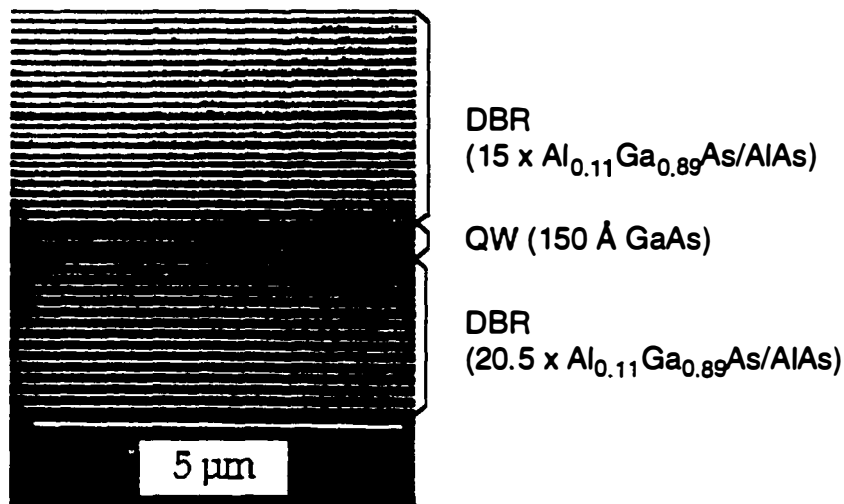


Fig. 1.7 An SEM micrograph of a microcavity sample with a one wavelength optical resonator and high reflectivity distributed Bragg reflectors. The quantum well and cavity are designed for optimal exciton-photon coupling at 10 K.

Chapter 2

CONTROLLING SPONTANEOUS EMISSION IN SEMICONDUCTORS

2.1 Spontaneous Light Emission

The spectroscopy of atomic radiation was essential to the development of quantum theory early in this century. Discrete lines in spontaneous emission spectra suggested an atom with discrete electronic states. The early models of electrons undergoing classical orbits around nuclei could not be reconciled with such spectra. Classically, the atom should radiate a continuous frequency spectrum as the electron spirals into the nucleus. Discretizing electronic energy levels and treating the bound electron as a 'stationary', but distributed charge density reconciled the observed data with the classical theory of radiation.

Before the formulation of the modern theory of radiation, with its attendant notion of the quantum vacuum, the spontaneous emission rate could be calculated by a judicious application of classical radiation theory to the quantum mechanical charge distribution. In the following chapter we treat spontaneous emission as classical radiation from an oscillating charge density. Following the treatment of French and Taylor (French, 1978), the quantum theory is employed only to

calculate the dipole moment as the electron undergoes a transition between quantum states. This approach is then extended to spontaneous emission inside microscopic semiconductor resonators. Surprisingly, this semiclassical approach is able to predict not only the spontaneous emission rates in microscopic resonators, but also nonperturbative effects such as polariton formation (Haroche, 1992). Accurate prediction of the modified spontaneous emission rate in these semiconductor resonators requires careful modeling of the multilayer mirrors that are employed. A simple approximate theory is developed to simulate our microwave and optical experiments.

Semiclassical theory of spontaneous emission

Light originates from the acceleration of electric charges. Classically, the electric charge is taken to be a point particle. Quantum theory treats the electron as a spatially spread charge density that is described by the wavefunction of the electron. The charge density is stationary in a state, $\psi(E)$, of definite energy E ; and is described by a dipole moment $\mathbf{D} = -q \int \mathbf{r} \psi^* \psi dV$. If, instead, the electron is in a superposition of two states with definite energy,

$$\psi = \psi_i e^{-iE_i t/\hbar} + \psi_f e^{-iE_f t/\hbar}, \quad (2.1)$$

the resulting charge density is not stationary

$$\mathbf{D} = -q \int \mathbf{r} [\psi_i^* \psi_f e^{i\omega t} + \psi_i \psi_f^* e^{-i\omega t}] dV; \quad (2.2)$$

it oscillates at a frequency ω such that $\omega = (E_i - E_f)/\hbar$. This oscillating charge distribution loses energy through light generation and the electron eventually relaxes into the low energy state. We can apply the classical theory of radiation to this oscillating charge density and calculate spontaneous emission rates and

radiation patterns. Figure 2.1 shows an example for atomic hydrogen $1s \rightarrow 2p$ transition as the electronic charge oscillates from one side of the atom to the other.

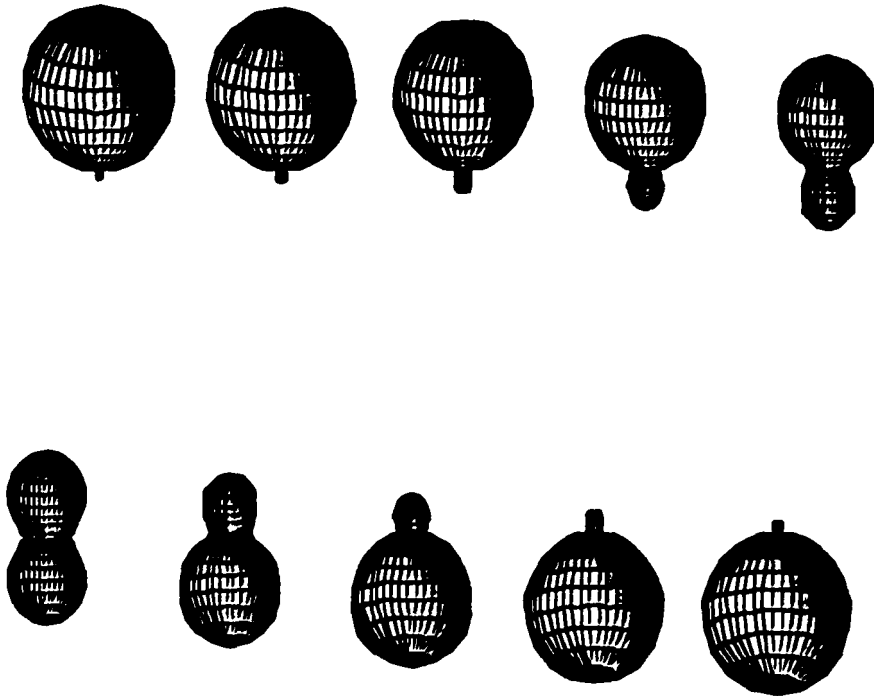


Fig. 2.1 The instantaneous electronic charge distribution for a hydrogen atom undergoing a $2p$ to $1s$ transition.

A useful metaphor for this situation is a damped mechanical oscillator. The equation of motion for the charge displacement, a , is

$$\ddot{a} + \gamma\dot{a} + \omega^2 a = 0. \quad (2.3)$$

where $|\mathbf{D}| = qa$. The damping constant (γ) is the rate that energy is lost by the oscillating charge as radiated light. If we assume that the rate of energy loss is much slower than the oscillation frequency – γ^{-1} is typically 1 ns and the

oscillation period for visible light is approximately 1 fs – we can readily calculate the instantaneous power radiated by the electron. Treating this oscillating charge as a source current ($\mathbf{J} = \dot{\mathbf{D}}$) in Maxwell's equations we can calculate the radiated electric and magnetic fields. An integration of the total energy carried away by electromagnetic fields yields the total radiated power (Haroche, 1992)

$$P = \frac{q^2 a^2 \omega^4}{12\pi\epsilon_0 c^3}. \quad (2.4)$$

The rate of spontaneous emission is

$$\gamma = \frac{P}{\hbar\omega} = \frac{q^2 a^2 \omega^3}{12\pi\epsilon_0 \hbar c^3} = \frac{1}{4\pi\epsilon_0} \frac{8\pi^3 q^2 a^2}{3\hbar \lambda^3} = 5.57 \frac{a^2}{\lambda^3} \text{ ns}^{-1}. \quad (2.5)$$

This expression could also be found quantum mechanically by employing Fermi's golden rule for radiation from a two state system into a three dimensional radiation field density of states. These two approaches yield the same result since they both rely on a quantum mechanical calculation of the charge density and an essentially classical calculation of the radiation field - the 3D density of photon states used in Fermi's golden rule is obtained from a solution of Maxwell's equations with free space boundary conditions, i.e. plane waves. The mechanical oscillator model will allow us to introduce driving fields and easily determine their influence on the spontaneous emission rate and oscillation frequency. For this reason, we will employ the semiclassical approach throughout the chapter and focus our attention on the calculation of the relevant accelerating charge density in a semiconductor.

NOTE TO USERS

Page(s) not included in the original manuscript are unavailable from the author or university. The manuscript was microfilmed as received.

UMI

be determined from Eq. (2.5). In Section 2.3, we will use this similarity between classical and quantum scale sources to construct scale models of semiconductors.

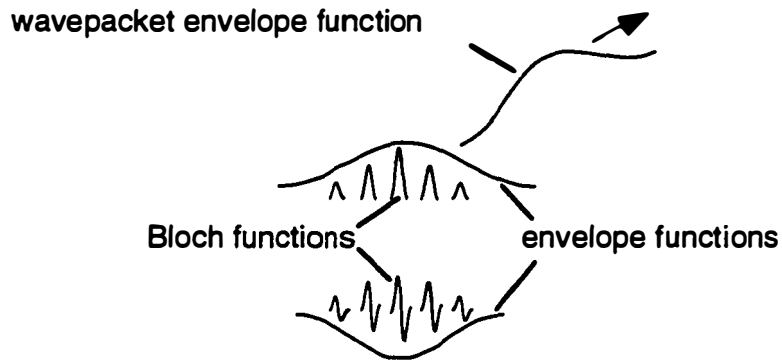


Fig. 2.2. Schematic of electron distribution in a semiconductor quantum well. z -axis perpendicular to the plane of the quantum well.

In this thesis, we will be studying radiation from a high density plasma of electrons and holes (such as in a semiconductor laser) or from a gas of electrons and holes bound together by their Coulomb interaction to form excitons. Fig. 2.2 provides a detailed picture of the charge density in the electron-hole plasma. The envelope functions in the z -direction are solutions of the effective mass Hamiltonian for an electron or hole in a finite square well potential. The wavepacket envelope in the x - and y -directions is approximated to be a plane wave, i.e. the coherence length assumed to be large. Fig. 2.3 shows the electronic charge density as a function of time for the electron-hole recombination process, an interband transition. The simulation is performed for a quantum well that is ten lattice sites wide. The electronic charge density at each lattice site undergoes oscillations with an amplitude approximately equal to one lattice constant.

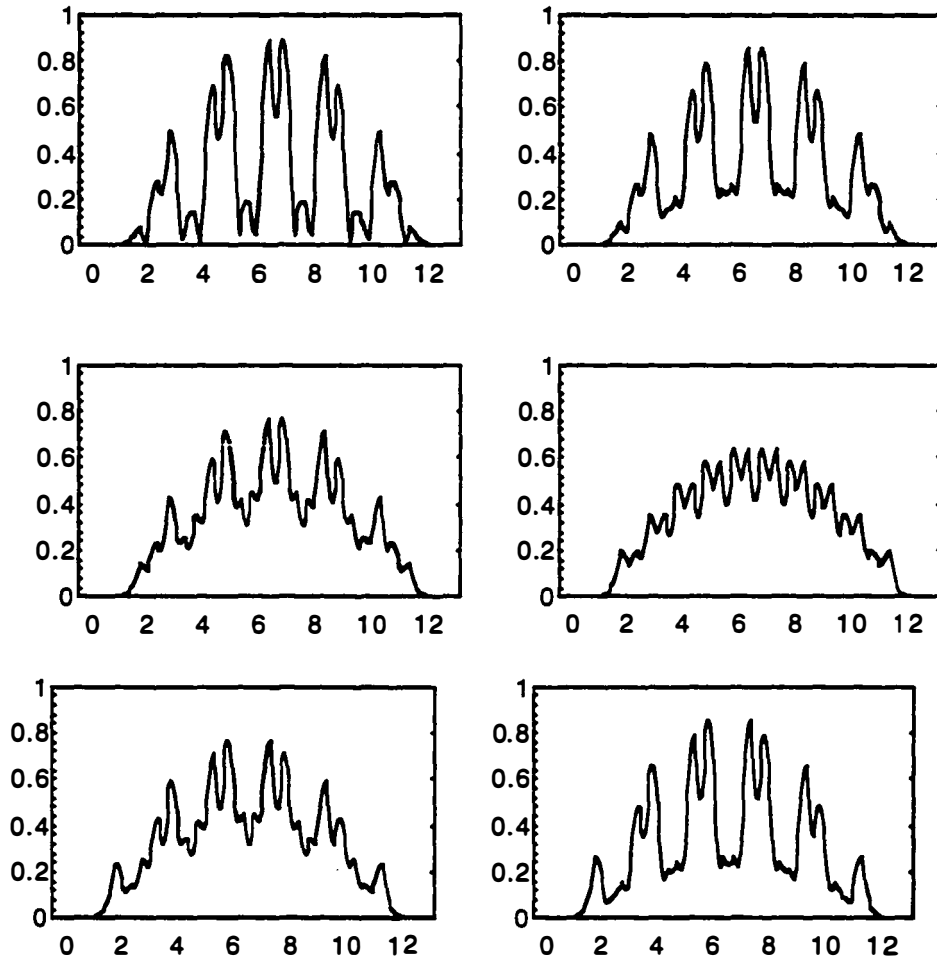


Fig. 2.3. The instantaneous electronic charge distribution for interband recombination of a free electron and hole. The horizontal axis is position along the z-axis.

The envelope functions are more difficult to picture for the electrons and holes bound together in the exciton. As a starting point, the much heavier hole is assumed to be localized to a single lattice site. The envelope functions for the electron trapped in the attractive potential of the hole are exactly like the electron orbitals for the hydrogen atom. Spontaneous emission from the exciton requires

the electron to fall into the hole – just as in an interband transition. Since the hole is localized, only the charge density at the single lattice site oscillates (see Fig. 2.4). The size of the dipole per lattice site is considerably greater than in the free electron-hole case since the Coulomb interactions concentrate the charge near a single lattice site. This picture adequately describes the enhancement of excitonic transitions and the radiation pattern.

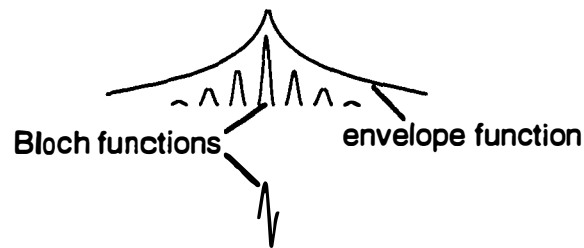


Fig. 2.4 Schematic of charge distribution for a localized exciton. Upper diagram is for the electron and the lower is for the hole.

The radiation pattern of the spontaneous emission depends on the spatial extent of the oscillating charge; an extended charge density radiates a narrow beam of light and a localized charge density radiates in all directions. Photoluminescence experiments confirm that a quantum well exciton radiates efficiently in all directions. In recent experiments by Wang, *et al.* (Wang, 1995), excitons were generated by resonant excitation along a specific direction. The rise time of the luminescence at a different angle, i.e. different photon momentum was measured. The rise time was measured to be an order of magnitude faster than the exciton lifetime. This efficient coupling of spontaneous emission into all directions is a measure of exciton scattering from one momentum state to another.

The heavy exciton mass and the small photon momentum means that even weak exciton scattering - energy exchange by as little as $50 \mu\text{eV}$ - is sufficient to scatter the exciton into all necessary momentum states. In other words, even weak exciton scattering will effectively localize the exciton.

Equipped with this picture of the charge density we can estimate the spontaneous emission rates for both the free electron-hole pair and the exciton. Since these calculations all rely on Eq. (2.5) it is assumed that the charge is oscillating in an infinite, homogeneous environment. Placement of dielectric interfaces or conductors will clearly change the local electric and magnetic fields. In the following section, we will determine how the placement of such boundaries also changes the total radiated power and therefore the spontaneous emission rate.

2.2 Modified Spontaneous Emission

The fields radiated away by a dipole oscillating in an infinite, homogeneous environment never return to perturb the oscillating charge. If we place the dipole near a reflective boundary, i.e. a conductor or a dielectric interface, then the fields radiated by the charge can return to influence the charge's own motion. If the field returns in phase with the charge motion, it will drive the charge to greater amplitude oscillations. If the field returns out of phase with the charge motion, it will damp the charge oscillation. In this way, the placement of the reflective boundary alters the power radiated by the dipole. Purcell (Purcell, 1946) observed that the spontaneous emission rate was, in fact, sensitive to the placement of reflectors adjacent to a radiating charge and could be "controlled" with the inclusion of appropriate boundary conditions. Recently, several

researchers have investigated spontaneous emission rate modifications for optical transitions in semiconductors (Bjork, 1991 and Yokoyama, 1992 and Ram, 1995).

The mechanical oscillator model of Eq. (2.3) can easily be extended to include the influence of the reflected driving fields, E_r ;

$$\ddot{a} + \gamma \dot{a} + \omega^2 a = qE_r(\omega, r)/m . \quad (2.6)$$

Following Haroche(Haroche, 1992), we use the ansatz that the dipole displacement varies as $a(t) = a_0 \exp(-i\Omega t)$. Again we assume that the spontaneous emission rate is much slower than the oscillation frequency of the charge. The spontaneous emission rate under the influence of the reflected field is then

$$\gamma' = \gamma + \frac{3\gamma}{2} \text{Im} \left(\frac{4\pi\epsilon_0 c^3}{q\omega^3 a_0} E_r \right) \quad (2.7)$$

and the new oscillation frequency is

$$\omega' = \omega - \frac{3\gamma}{4} \text{Re} \left(\frac{4\pi\epsilon_0 c^3}{q\omega^3 a_0} E_r \right) \quad (2.8)$$

Determination of the modified spontaneous emission rate is primarily a matter of determining the field reflected by the nearby boundaries.

Method of images

A charge radiating near an ideal conductor is driven by a reflection of its own field. This reflected field accumulates a phase delay as it propagates to the conductor and back; there may also be an additional phase shift imparted by the reflector itself. The driving field in the mechanical oscillator model is this phase-shifted reflection of the original field. If we place the oscillating charge between two such conductors we must keep track of the field as it bounces between the

conductors and then drives the charge. The driving field in this case consists of a phase-shifted reflection of the original field after one round trip, two round trips, etc. The method of images is a convenient way to keep track of all these reflected field components. A dipole adjacent to a single conductor is equivalent to a two dipole system – the oscillating charge density and its image. A dipole between two conducting plates is equivalent to an infinite array of image dipoles. The location of each dipole along the z-axis is given by

$$z_n = nL_c + (-1)^n z_0 \quad (2.9)$$

where L_c is the cavity length and z_0 is the location of the physical dipole relative to the cavity center. Fig. 2.5 shows the equivalent image dipole arrays for these and other geometries.

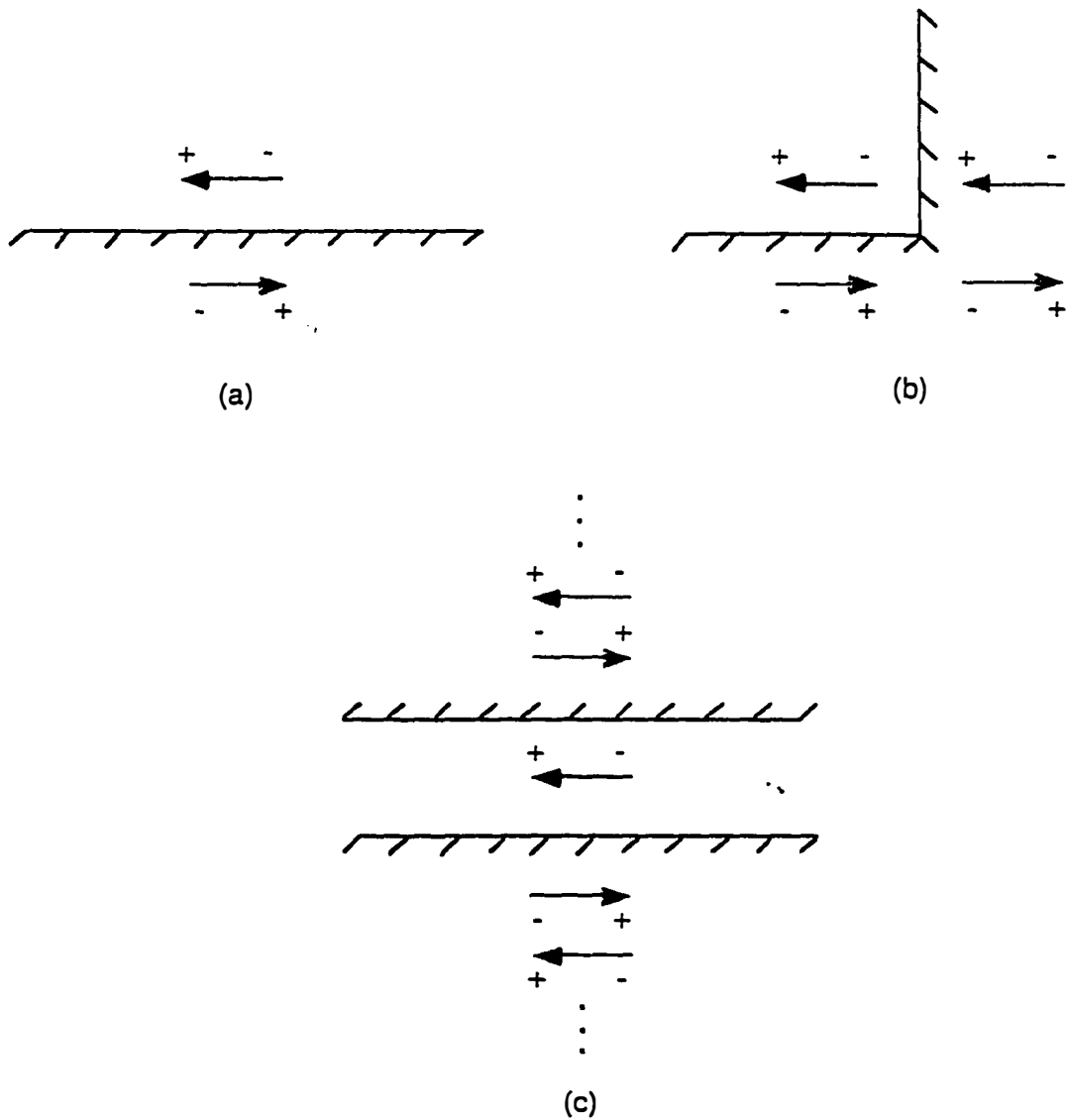


Fig. 2.5 The equivalent image arrays for a dipole (a) adjacent to a single mirror and (b) a corner reflector, and (c) inside a cavity.

Finite reflectivity resonators can be approximated by reducing the charge on the image dipole. The n th dipole will have a moment of

$$D_n = D_o (r_1 r_2)^{|n|/2} \quad \text{for } n \text{ even} \quad (2.10)$$

$$= D_o \frac{2(r_1 r_2)^{(|n|+1)/2}}{\left(1 + \frac{n}{|n|}\right) r_2 + \left(1 - \frac{n}{|n|}\right) r_1} \quad \text{for } n \text{ odd.}$$

For a symmetric resonator with $r_1 = r_2$ the above expressions simplify to

$$D_n = D_o r^{|n|}. \quad (2.11)$$

Fig. 2.6 shows the spontaneous emission rate of a free electron-hole dipole at the center of an ideal cavity. The spontaneous emission rate is plotted as a function of cavity length. Clearly the most significant alteration of spontaneous emission rate occurs when the reflected driving fields are large; this occurs for high reflectivity mirrors and small cavity lengths, i.e. small dipole to image separations.

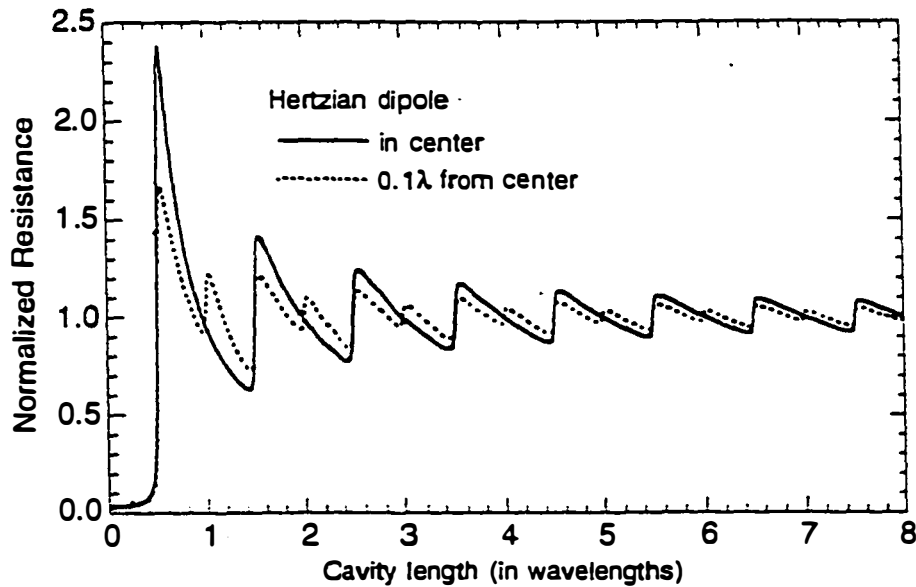


Fig. 2.6 The calculated spontaneous emission rate for a free electron-hole pair at the center of an optical cavity. The spontaneous emission rate is plotted as a function of the cavity length.

Since the method of images applies only when the reflective boundary is an ideal conductor, it offers only a rough simulation of experiment. Realizable boundaries distort the reflected fields. Metallic boundaries with finite conductivity have reflectivities less than unity and phase-shifts upon reflection that depend on incident angle. Dielectric boundaries have angle dependent reflectivities that are described by the Fresnel equations. The simple image construction does not strictly apply to any of these boundaries.

Modal Decomposition

An alternative to the image method treatment is to decompose the reflected fields in terms of a complete set of modes. The set of plane waves and the set of cavity modes are the two most commonly employed basis sets used to decompose the reflected field. High reflectivity resonators with short cavity lengths are best described by a cavity mode decomposition since the dipole will radiate into only a few of these modes. Low reflectivity resonators weakly alter the free-space behavior of the dipole so plane waves are a more natural choice. For the moment we will focus on the cavity mode description.

The equation of motion for the charge density is the same as above with the decomposition of the reflected field into a set of cavity modes (E_m),

$$\ddot{a} + \gamma\dot{a} + \omega^2 a = \frac{q}{m} \sum_m E_m . \quad (2.12)$$

The cavity modes are again described by a harmonic oscillator equation known as the Helmholtz equation,

$$\ddot{E}_m + \Gamma_m \dot{E}_m + \omega_m^2 E_m = -\frac{q}{\epsilon_0} \ddot{a} . \quad (2.13)$$

The cavity 'oscillators' are driven by the polarization of the oscillating charge.

In the limit that only a single cavity mode is coupled to the radiating dipole, the dipole oscillator and cavity mode represent two coupled simple harmonic oscillators. An initially excited dipole radiates energy into the single cavity mode. This energy is coherently reabsorbed by the dipole so long as the photon does not leave the cavity or the dipole scatters. The dipole then reradiates the energy back into the cavity mode. The back-and-forth transfer of energy between the dipole and cavity mode is observable as oscillations in the light leaving the cavity. The oscillation frequency increases as the dipole-field coupling increases; as the emission and absorption rates increase. In the frequency domain the oscillation is observed as two separate emission lines. This process can also be understood from the perspective of supermodes for the coupled harmonic oscillators. The coupled system is described by supermodes that are superpositions of the dipole and cavity states. When the dipole resonant frequency is equal to the cavity mode frequency, the two supermodes are split in energy by the coupling strength between the dipole and field. These supermodes have been extensively studied for atomic vapors coupled to a single mode in a high-Q resonator (Kimble, 1991).

Typically, spontaneous emission involves the excitation of many cavity modes by the oscillating charge. When the energy is initially in the dipole oscillator, the supermodes of the dipole-cavity system are all coherently excited. Since the cavity modes have many different oscillation frequencies, the energy initially in the dipole spreads out over all the accessible cavity modes. This energy returns to reexcite the dipole at the beat frequency between supermodes. The time required for the dipole-cavity supermodes to all constructively interfere is greater than the

electron scattering time and the photon lifetime. Therefore, the reexcitation of the dipole is not typically observed and instead energy appears only to leave the dipole. This one-way transfer of energy from the dipole oscillator to a multiplicity of cavity modes is what we observe as spontaneous light emission. Engineering the optical environment of the radiating dipole allows us to specify the number of accessible modes and to fundamentally alter the nature of spontaneous light emission by the dipole.

2.3 Semiconductor Microcavities

Semiconductor microcavities in the form of vertical cavity surface emitting lasers (VCSELs) have driven the development of wavelength scale semiconductor resonators with high reflectivity mirrors (Coldren, 1995). Epitaxial growth of semiconductors enables the fabrication of high quality layered structures with layer thickness accuracy to a few hundredths of a wavelength. The use of heterostructures enables the confinement of dipoles in an optical cavity to spatial dimensions which are a small fraction of a wavelength. This remarkable control has enabled us to engineer the optical cavity so as to restrict the number of accessible modes and even to realize 'reversible' spontaneous emission (Weisbuch, 1992). Again, the semiclassical oscillator formalism presented above will be used to describe spontaneous emission in semiconductor microcavities.

Distributed Bragg reflectors

Using the reflected fields we can determine the modified spontaneous emission rate in a semiconductor microcavity. Unfortunately, high reflectivity

mirrors in semiconductor microcavities are only realized by employing multilayer dielectric mirrors known as distributed Bragg reflectors (DBRs). These multilayer stacks require as many as 40 layers that are each a quarter wavelength thick. High reflectivities are realized by constructive interference of the fields reflected by the dielectric discontinuity between each layer. Since DBRs rely on the interference of light, their reflectivity exhibits a complex dependence on the frequency and angle of the incident light — as can be seen from Fig. 2.7. The high reflectivity region is called the stopband and the low reflectivity region is called the passband.

In this section we employ image methods to develop simple models of the modified spontaneous emission in a DBR microcavity. The complexity of the DBR boundary has previously required a modal decomposition approach to semiconductor microcavities; this plane wave decomposition employed in (Bjork, 1991) is numerically intensive. The image method that we develop below is the basis for a complete analytic treatment that can be found in (Ram, 1995). Here we chose only to introduce the simplified model and present a qualitative discussion of its limitations.

We seek to approximate the DBR reflectivity with the simplest possible reflector - the hard mirror. A hard mirror is defined as a reflector with a constant complex reflectivity (Babic, 1993),

$$r_h = r_c \exp(-i\phi). \quad (2.14)$$

The hard mirror reflection is independent of both incident angle and frequency. r_c can be either a positive or negative real number. We choose this simple hard mirror reflector since it is the most general boundary that can be represented by a single image dipole.

In addition to specifying r_h , we have the freedom to displace the hard mirror by some distance, L_{pen} (Fig. 2.8). As seen from this distance, the hard mirror has a phase variation that is dependent on both the frequency and the incident angle

$$r'_h(k_z) = r_c \exp(-i\phi) \exp(2ik_z L_{pen}) = r_c \exp(-i\phi') \quad (2.15)$$

where the phase (ϕ') varies linearly with the frequency and with the cosine of the incident angle

$$k_z = \frac{n_i \omega}{c} \cos \theta_i \approx \frac{n_i \omega}{c} \left(1 - \frac{\theta^2}{2} \right). \quad (2.16)$$

The primed variables, r'_h and ϕ' , indicate that the reference plane is a distance L_{pen} away from the hard mirror and n_i is the cavity index. L_{pen} is used as a fitting parameter for the phase variation in a DBR. As seen from the dashed curves in Fig. 2.7a,b, the DBR resembles the hard mirror only for angles and frequencies well within the band stop, where the power reflectivity, r_c^2 , is approximately constant. r_c can be either positive or negative depending on the reflected phase shift from the DBR on exact resonance. Since a normally incident plane wave at the center of the stopband (with a wave vector of k_c) must have only a 0 or π phase shift upon reflection, the phase of the hard mirror (ϕ) must compensate for the displacement, i.e. $\phi = 2k_c L_{pen}$;

$$r'_h(k_c) = r_c \exp(-2ik_c L_{pen}) \exp(2ik_c L_{pen}). \quad (2.17)$$

By far the most common mistake made in implementing the hard mirror approximation is in neglecting the extra phase shift of the hard mirror reflection.

It is also important to realize that the two L_{pen} s used in Fig. 2.7a and 2.7b were different. In general, the effective distances obtained from the variation of the phase as a function of incidence angle at the Bragg frequency, $L_D = \frac{1}{2k_c} \frac{\partial^2 \phi'}{\partial \theta_i^2}$, and the phase as a function of frequency at normal incidence, $L_r = -\frac{c}{2n_i} \frac{\partial \phi'}{\partial \omega}$,

will be different (Babic, 1995). L_D is the relevant hard mirror construction for the method of images. The relevant hard mirror boundary is then

$$r'_h(\theta_i, \omega = \omega_c) = r_c \exp(-i(k_c - k_c)2L_D) \quad (2.18)$$

This hard mirror boundary has a reflectivity that is independent of the incident angle in both amplitude and phase; it does not distort the incident field. This

simple boundary is suitable for defining a single image dipole. Figure 2.8 shows the equivalent image array for an oscillating charge adjacent to a single DBR. The hard mirror construction is used to determine the placement of the image charge.

Spontaneous emission in a distributed mirror microcavity

With the construction of the equivalent array, we can immediately determine the field profile within the resonator by using a superposition of the field radiated by the n^{th} image dipole (Balanis, 1982):

$$\begin{aligned} E_{\text{radial}} &= -2 \frac{qD_n k^3}{4\pi\epsilon_0} \cos\theta \left[\frac{i}{(kr)^2} - \frac{1}{(kr)^3} \right] e^{+ikr} \\ E_{\theta} &= \frac{qD_n k^3}{4\pi\epsilon_0} \sin\theta \left[\frac{1}{kr} + \frac{i}{(kr)^2} - \frac{1}{(kr)^3} \right] e^{+ikr} \\ E_{\phi} &= 0. \end{aligned} \quad (2.19)$$

such that

$$kr = \frac{2\pi}{\lambda} \sqrt{(nL'_c + (-1)^n |z_0| - y)^2 + x^2}. \quad (2.20)$$

Here θ is measured relative to the direction of the dipole moment. L'_c is the effective cavity spacing, $|z_0|$ is the distance from the real dipole to the midpoint of the cavity. Fig. 2.9 shows the total reflected electric field in the plane perpendicular to the hard mirrors ($\theta_i = \pi/2$) for a horizontal dipole. The fields are plotted for dipoles placed at various positions within the optical cavity. The radiated field is largest when the dipole is at a peak in the standing wave pattern and smallest when the dipole is at a null in the standing wave pattern. These two cases represent constructive and destructive interference, respectively, of the fields driving the charge oscillation.

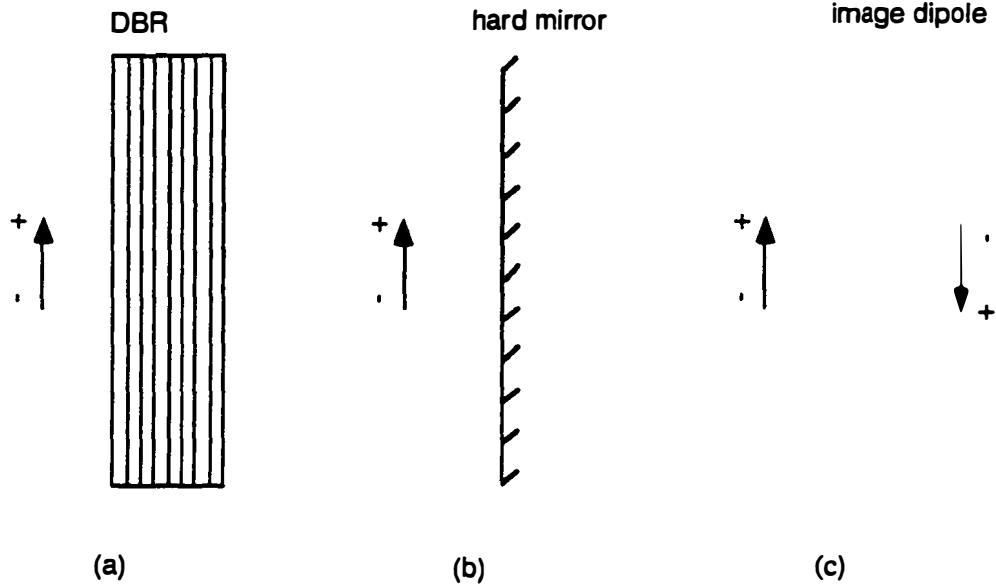


Fig. 2.8 The equivalent array of image dipole radiators to a dipole adjacent to a single hard mirror.

The spontaneous emission rate at the various dipole positions can be calculated by using the reflected fields described by Equation (2.19) in Equation (2.7). The DBR resonator is described by a large linear array of image dipoles. As a starting point, we consider a dipole radiating next to a single DBR. Using the hard mirror approximation (Eq. (2.18)) to calculate the reflected fields, we can express the modified spontaneous emission rates for a dipole oriented parallel and perpendicular to the mirrors as

$$\frac{\gamma'_{\perp}}{\gamma} = 1 + \frac{3}{2} \text{Im} \left[r_c e^{i\phi} e^{-ikd} \left(\frac{i}{(kd)^2} - \frac{1}{(kd)^3} \right) \right] \quad (2.21)$$

$$\frac{\gamma'_{\parallel}}{\gamma} = 1 + \frac{3}{2} \frac{r_c}{(2kd)^3} [4kd \cos(2kd - \phi) - 2 \sin(2kd - \phi)] \quad (2.22)$$

and

$$\frac{\gamma'_{\parallel}}{\gamma} = 1 + \frac{3}{2} \text{Im} \left[r_c e^{i\phi} e^{-ikd} \left(\frac{1}{(kd)^2} + \frac{i}{kd} - \frac{i}{(kd)^3} \right) \right] \quad (2.23)$$

$$\frac{\gamma'_{\parallel}}{\gamma} = 1 + \frac{3}{4} \frac{r_c}{(2kd)^3} \left[4kd \cos(2kd - \phi) + 2(4k^2 d^2 - 1) \sin(2kd - \phi) \right], \quad (2.27)$$

where, as in Eq. (2.14), $\phi = 2(k_c - k)L_r + 2kL_D$ also $d = z + L_D$ where z is the distance from the dipole to the DBR.

The radiation adjacent to the hard mirror differs significantly from that adjacent to an ideal conducting mirror. Fig. 2.10 shows γ'_{\perp}/γ and $\gamma'_{\parallel}/\gamma$ as a function of z for an idealized reflector and several DBRs, $L_D = 0.0, 0.1$ and $0.2\mu\text{m}$. We see that modulation of the emission rates by the reflector is diminished with increasing L_D . As the penetration depth increases the driving field radiated by the image dipole is smaller – since the image dipole is further away. The large DBR penetration depth prevents the dipole spontaneous emission rate from being affected by the microcavity. The control afforded by epitaxial growth of cavities and mirrors cannot be used to realize the necessary effective cavity lengths to achieve strict control of the spontaneous emission rates.

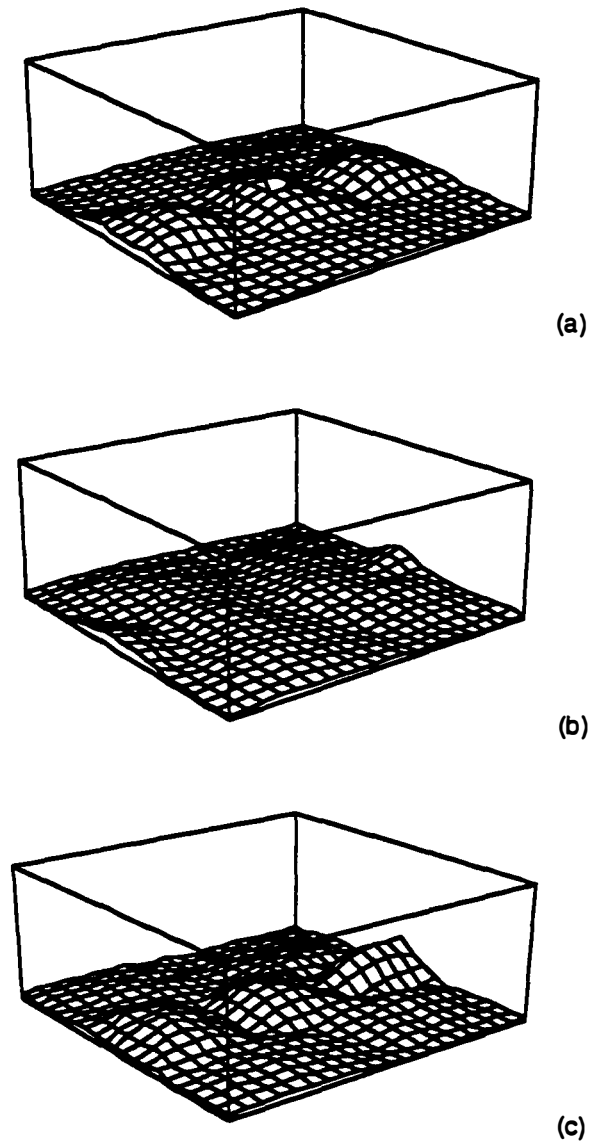


Fig. 2.9 The intracavity electric field radiated by a dipole at the center of a small optical cavity. The cavity is defined by two finite reflectivity mirrors that are separated by $3\lambda/2$. The radiating dipole is placed at the (a) center of the cavity, (b) $\lambda/4$ from the center at a null in the standing wave and (c) $\lambda/2$ from the center at a peak in the resonant optical mode.

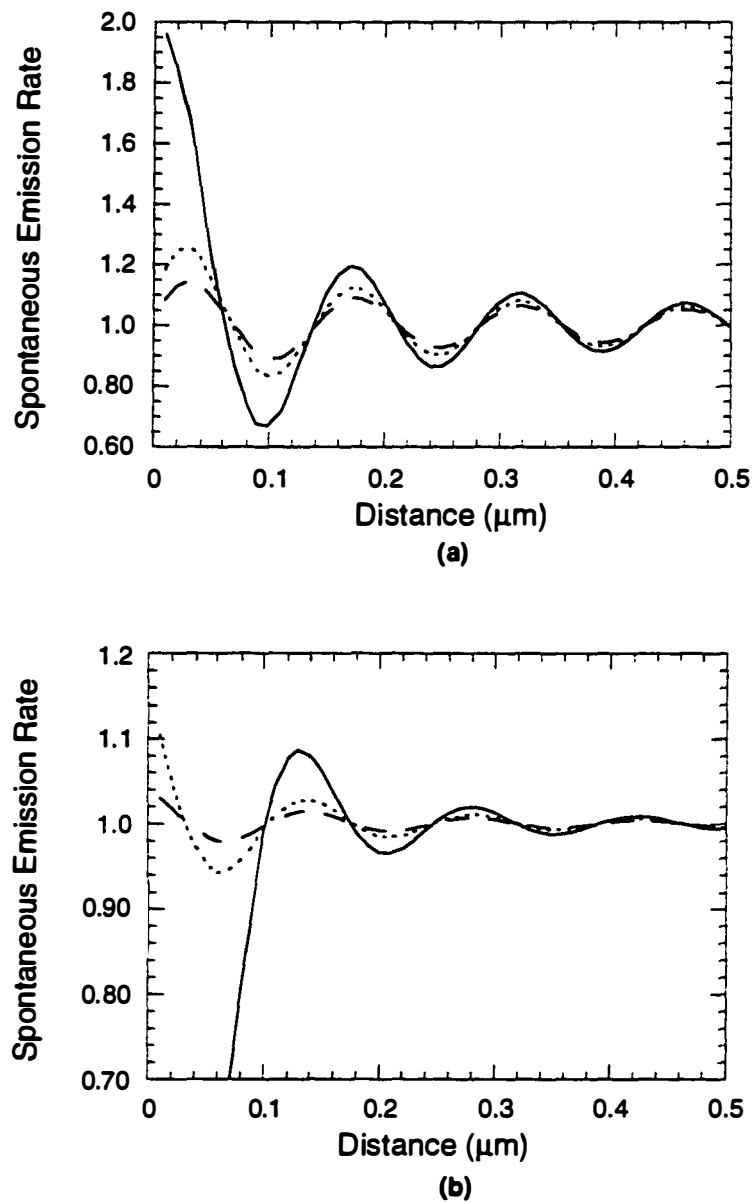


Fig. 2.10 The spontaneous emission rate for a dipole adjacent to a single DBR. The spontaneous emission rate is plotted as a function of the distance between the dipole and mirror. The dipole is oriented (a) parallel and (b) perpendicular to the plane of the mirrors. The calculations are performed for (solid) $L_D = 0.0 \mu\text{m}$, (dotted) $L_D = 0.1 \mu\text{m}$ and (dashed) $L_D = 0.2 \mu\text{m}$.

Additionally, DBRs exhibit high reflectivities only for near normal incidence. At large angles the DBR reflectivity is low. Spontaneous emission into the passband of the DBR cannot be avoided even for small, high reflectivity microcavities. Fig. 2.11 shows the spontaneous emission intensity in an actual DBR resonator and for the equivalent hard mirror resonator. At large angles the spontaneous emission is essentially unaffected by the microcavity. The DBR image theory is expected to overestimate its influence on the dipole spontaneous emission rate.

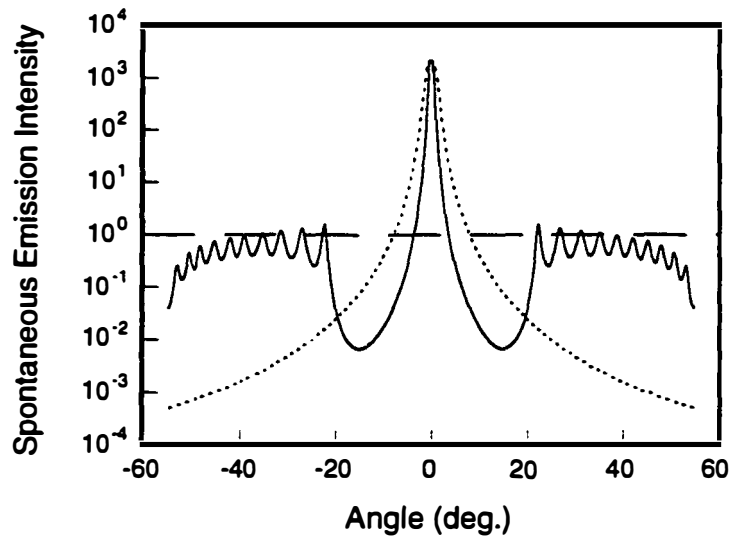


Fig. 2.11 The spontaneous emission rate intensity versus emission angle for a dipole at the center of a half-wavelength cavity. The intensity is plotted for a dipole in a cavity with ideal mirrors (dotted) and with two GaAs/AlAs distributed Bragg reflectors (solid). The intensity is normalized to free space (dashed).

Measurements at optical frequencies do not lend themselves to careful testing of the DBR image theory; measuring the dependence of spontaneous emission lifetime on the distance from a quantum well to a DBR requires the growth of many samples. Instead we have examined a scale model of a semiconductor microcavity where the measurements are performed at GHz instead of THz frequencies.

Our experiments use a dipole antenna as the radiation source. Power is delivered to the antenna through a semi-rigid waveguide. As with spontaneous emission, the cavity alters the coupling strength into individual modes as well as the density of modes. The power radiated by the antenna can be monitored by monitoring the power delivered through the waveguide that is used to feed the dipole. A network analyzer directly relates the delivered power to the radiation resistance of the antenna.

For a given array size, the driving-point impedance can be expressed as a summation of the dipole self-impedance and contributions from mutual coupling between the physical dipole and images (Balanis, 1982). The location of each dipole along the z-axis is again given by

$$z_n = nL'_c + (-1)^n z_o \quad (2.28)$$

where L'_c is the effective cavity length and z_o is the location of the physical dipole relative to the cavity center. The driving point impedance is then

$$Z_{in} = R_{in} + jX_{in} = \sum_n \left(\frac{I_n}{I_o} \right) Z_{no} = \sum_n r_h^{|n|} Z_{no} \quad (2.29)$$

where Z_{no} is the self-impedance of the (physical) dipole, and $Z_{m,n}$ is the mutual impedance between the dipole and its n th image separated by a distance (z_n to z_o). Dipole-cavity resonance occurs when $X_{in} = 0$. For thin, center-fed dipoles of length l and radius a , a single expression for both the self and mutual impedance can be found using the induced EMF method (Ram, 1994),

$$Z_{no} = j \frac{\eta}{4\pi} \int_{-l/2}^{l/2} \frac{\sin k(l/2 - |\chi|)}{\sin^2(kl/2)} \left[\frac{e^{-jkR_i}}{R_i} + \frac{e^{-jkR_o}}{R_o} - 2 \cos(kl/2) \frac{e^{-jkR_e}}{R_e} \right] d\chi \quad (2.30a)$$

where

$$R_m = \sqrt{(|z_n - z_o| + a)^2 + (\chi + ml/2)^2}. \quad (2.30b)$$

Equations (2.29) and (2.30) provide a simple means for investigating the influence of mutual coupling on the dipole impedance as a function of array spacing and frequency. The real part of the self-impedance is the free-space radiation resistance from the dipole and each of the mutual coupling terms represents perturbations on the free-space radiation rate.

We use a microwave vector network analyzer to directly measure radiation rates from a dipole antenna. Figure 2.12 shows the measurement set-up for the microwave measurements. These measurements were made at 11.4 GHz with an HP8720 vector network analyzer, using an unbalanced 2.7 cm dipole, center-fed from a semi-rigid coaxial cable. Figure 2.13 shows a sample measurement of the radiation resistance versus dipole position in a cavity constructed from two copper sheets measuring 30 cm on a side. The theoretical result from Eq. (2.30) is also shown for comparison. Both curves have been normalized to the respective impedances measured without a cavity, and show very good correlation in the behavior of impedance with location. Note that the extrapolated radiation

40
resistance does not get to zero at the cavity walls because of the finite conductivity of the copper and the residual losses in the antenna.

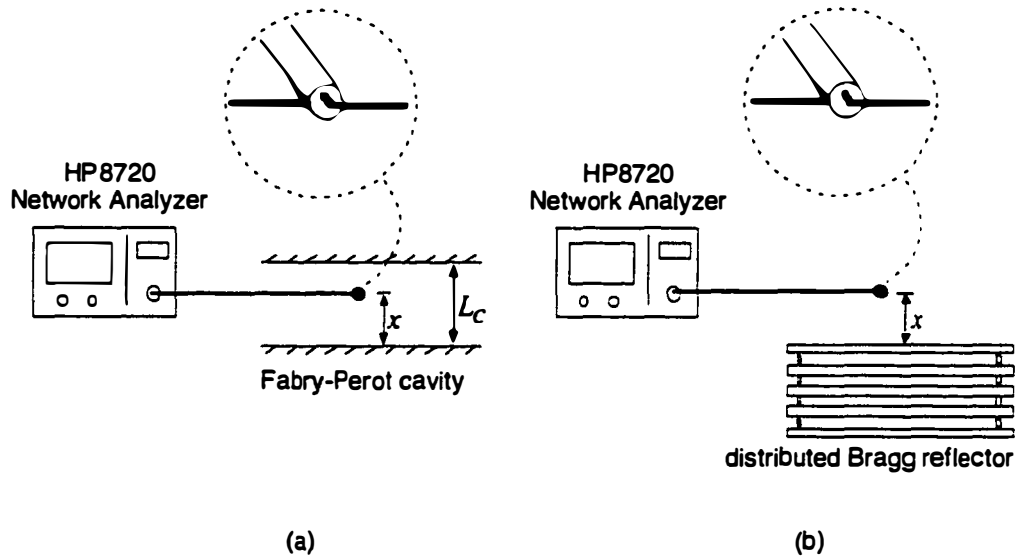
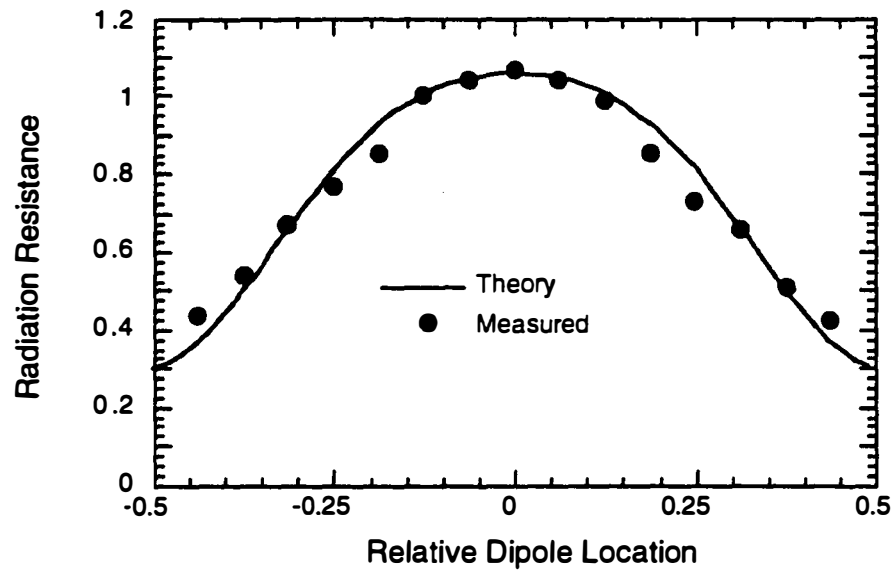
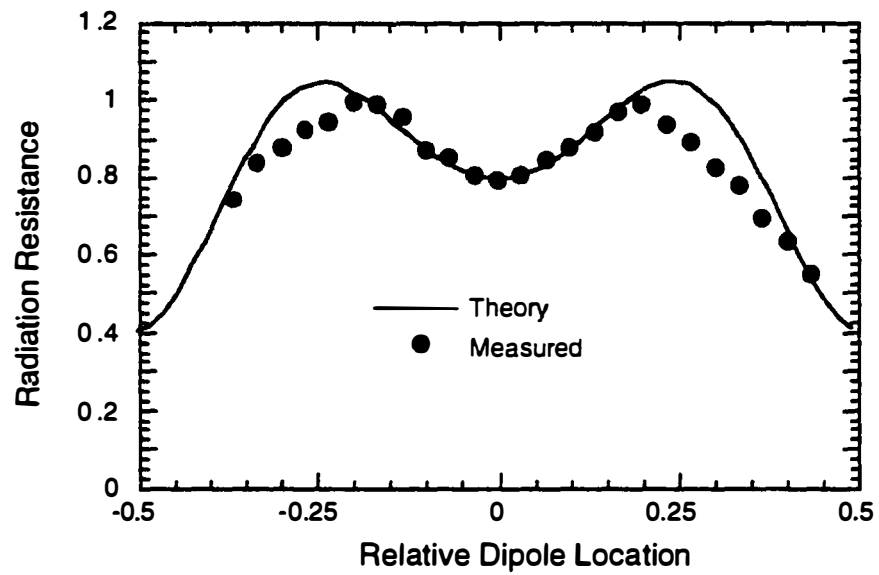


Fig. 2.12 The measurement set-up



(a)



(b)

Fig. 2.13 The measured radiation resistance for a small dipole antenna inside a cavity defined by two copper plates.

This same measurement approach was used to test the influence of a single DBR on the radiation resistance of a dipole. Since the induced EMF method does not have explicit dependence on the incidence angle, it is difficult to introduce the effects of a finite mirror band width into this treatment. The method of complex images (Shubair, 1995) allows one to apply the induced EMF method to the exact DBR, but we wish only to establish how well a single image element approximates the DBR boundary. Since we neglect the fact that the mirror has a finite band stop, our theory is expected to overestimate the achievable inhibition or enhancement by the DBR.

The alteration of the dipole emission rate at 3.71 GHz by a single dielectric DBR was observed. The millimeter wave DBR consisted of 5.5 periods of air and Rexolite 1422 (a nearly lossless dielectric with an index of refraction of 1.56). The Bragg wavelength for this DBR was 8.08 cm (3.71 GHz). The peak reflectivity was .9848 (assuming no losses). This structure had $L_D = 2.343$ cm.

The radiation resistance was compared to the results of the induced EMF method using a two element array modeled according to the hard mirror construction described above (Fig. 2.14). Both curves have been normalized to the respective impedances measured in free space, and show very good correlation in the behavior of impedance with location. It is important to note that there are no fitting parameters in the theoretical curve. Using only the high and low indices, the dimensions of the DBR and the dimensions of the dipole antenna, the theory curve was specified exactly. Upon comparison, we see that the agreement greater than a quarter wavelength away is good suggesting that our technique for the construction of the equivalent dipole array is reasonable. The

experiment confirms that an image element constructed according to the hard mirror construction approximates the DBR's influence on the dipole emission rate.

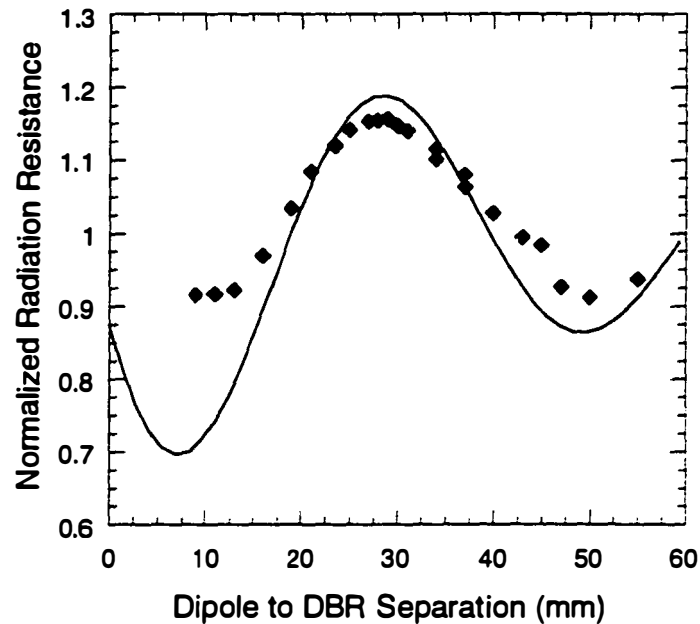


Fig. 2.14 The measured radiation resistance for a small dipole adjacent to a single distributed Bragg reflector. The dashed line shows the calculated radiation resistance using the equivalent hard mirror construction.

The hard mirror resonator – and the image theory developed above – overestimate the influence of the microcavity on the spontaneous emission rate. Despite a short cavity length and high reflectivity mirrors the semiconductor microcavity is unable to influence the spontaneous emission rate significantly. The DBR microcavity cannot completely alter the environment for the dipole, the passband is effectively a hole in the resonator and the effective cavity length is large. Given the limitations of the optical environment we must pay more careful

attention to the radiation pattern of the electrons. In the next section, we realize single mode coupling by fundamentally altering the distribution of the oscillating charges in momentum space.

2.4 Microcavity Exciton-Polaritons

Distributed Bragg reflectors are the ideal mirrors for surface emitting laser applications. They offer high reflectivities at their resonant frequency and can be easily integrated into short cavity laser structures. In a conventional semiconductor laser, threshold is determined by the optical losses seen only by the lasing mode. The optical environment must be optimized only for this single mode – in only one direction and for one frequency. In a microcavity laser, the optical environment must affect the modes in every direction and of every color. As we saw in Section 2.3, DBRs are not suited for such demanding applications.

An alternative approach is to modify the emission properties of the oscillating charges so as to couple light into only a few directions. In Section 2.1, we presented a picture of the exciton as a localized oscillating charge radiating in all directions. The exciton was able to radiate into all directions because the scattering between different exciton momentum states was strong and the energy required to scatter from a state radiating in one direction to a state radiating in a different direction was never more than $50 \mu\text{eV}$. The same argument applies to free electrons and holes which also have fast momentum scattering times and can radiate in all directions. Suppressing scattering events between neighboring momentum states would effectively restrict the modes into which an oscillating charge could radiate.

Equation (2.8) describes a characteristic shift in the resonance energy of a dipole coupling to light. This shift varies with the momentum of the oscillating charges. When the energy and momentum for the oscillating charge and the emitted photon are the same, there is optimal coupling and a correspondingly large shift in dipole energy. At different momenta the coupling is effectively smaller and the shift becomes smaller. Since the different momentum states experience different energy shifts, strong-coupling to light is a way to change the energy required to scatter from one momentum state to another. For a free electron-hole, the coupling can shift the energy only by $40 \mu\text{eV}$; this shift is small and does not effectively suppress the scattering between momentum states. These free electron-hole pairs still radiate into all directions, i.e. couple to many optical modes. Excitons couple more strongly to light. The strong-coupling energy shift is 100 times larger than for free electron-hole pairs. These excitons couple more strongly to the light field than to other momentum states. By suppressing momentum scattering, single mode emission becomes possible even in a DBR microcavity (Weisbuch, 1992).

Exciton-Polaritons in GaAs

The microcavity structure (Fig. 2.15) investigated consists of a top mirror with 15 $\text{Al}_{0.11}\text{Ga}_{0.89}\text{As}/\text{AlAs}$ periods, a $\text{Al}_{0.3}\text{Ga}_{0.7}\text{As}$ cavity of thickness $L_c = \lambda$ and a bottom mirror with 20.5 $\text{Al}_{0.11}\text{Ga}_{0.89}\text{As}/\text{AlAs}$ periods (Goobar, 1996). A single GaAs quantum well (QW) of thickness $L_{\text{QW}} = 150 \text{ \AA}$ is placed at the center of the cavity which has its resonance aligned to the heavy-hole exciton (HHx) absorption line at around 10 K. The reflectivity of the structure was studied by illuminating the

sample with a white light source and measuring the reflection with an optical spectrum analyzer. The “empty cavity” linewidth was measured at 200 K when the exciton absorption was detuned from the cavity resonance. The measured spectra at this temperature exhibited a resonance linewidth of $\Delta E_c = 0.6$ meV. This linewidth was also verified in measurements done on a true empty cavity, e.g. a separately grown sample consisting in only the cavity and the mirrors. At 10 K, the HHx and light-hole exciton (LHx) photoluminescence linewidths were $\Delta E_{HHx} = 0.45$ meV and $\Delta E_{LHx} = 1$ meV, respectively. The separation between the two PL peaks was 7 meV. An impurity bound exciton 1 meV below the HHx resonance could also be observed.

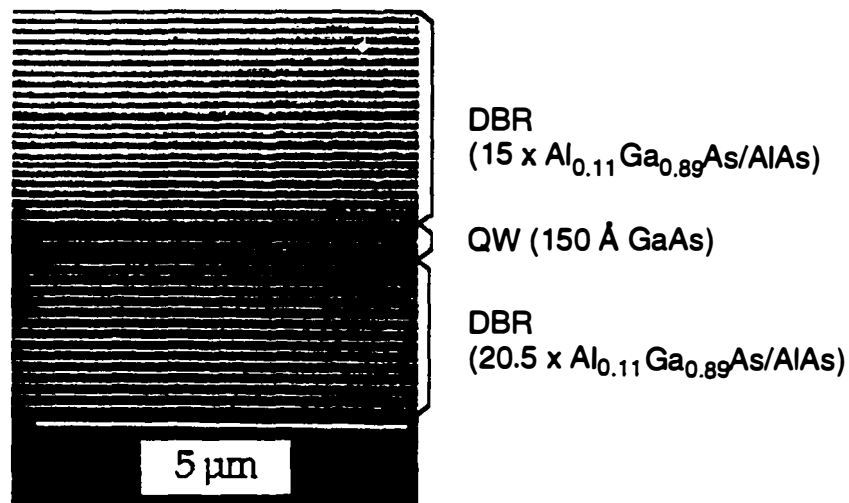


Fig. 2.15 A SEM micrograph of a microcavity sample with a one wavelength optical resonator and high reflectivity distributed Bragg reflectors. The quantum well and cavity are designed for optimal exciton-photon coupling at 10 K.

Due to the growth inhomogeneity, the thickness of the cavity becomes gradually smaller toward the edge of the wafer. Consequently, the resonance of the cavity $E_c(r)$ shifts toward higher energies. In the strong coupling regime, as $E_c(r)$

approaches the heavy-hole $E_{HHx}(r)$ and light-hole $E_{LHx}(r)$ excitonic resonances, anticrossings between the interacting modes occur. The anticrossings are a result of the strong coupling between the exciton and the single optical mode. As described in Section 2.2, the exciton dipole and the cavity field represent two coupled harmonic oscillators. The coupled oscillators are described by supermodes called polaritons. Two polariton branches are constructed from superpositions of the exciton and photon states (Weisbuch, 1992). When the dipole resonant frequency equals the optical mode frequency, i.e. at zero detuning, the two supermodes are split by an energy proportional to the coupling strength between harmonic oscillators.

The anticrossings are more clearly observed in Fig. 2.17 where the reflectivity minima vs. position and detuning, $E_C(r) - E_{HHx}(r)$, are presented. The dots are the measured energy values of the reflectance minima at 10 K. Two anticrossings are observed; the 3.7 meV splitting due to the C - HHx coupling at zero detuning is the largest reported for a single QW in the GaAs material system. The narrower 2.4 meV splitting at 7 meV detuning is due to the C - LHx coupling. The smaller C - LHx splitting is due to the lower oscillator strength of the LHx. From these measurements the ratio of the HHx oscillator strength to that of the LHx is 2.4, which is in good agreement with both theoretical and experimental values reported previously (Fisher, 1995, Andreani, 1990 and Savona, 1995). The supermode splitting can be calculated as $2\hbar\Omega_{HHx(LHx)} = 2\hbar e \sqrt{f_{HHx(LHx)} / 2n_C^2 \epsilon_0 m_0 L'_C}$ (Savona, 1995), where $f_{HHx(LHx)}$, n_C , and $L'_C = L_C + 2L_D$, are the oscillator strength of the HHx (LHx), the refractive index in the cavity and the effective cavity length including the penetration depth in the DBR mirrors, respectively; ϵ_0 , m_0 and e are the dielectric constant for vacuum, the electron mass and the electron charge, respectively. According to (Andreani, 1994), for a 150 Å GaAs/Al_{0.3}Ga_{0.7}As QW, $f_{HHx} = 40 \cdot 10^{-5} \text{ \AA}^{-2}$ and $f_{LHx} = 16.7 \cdot 10^{-5} \text{ \AA}^{-2}$. Using $n_C = 3.4$, and the calculated $L'_C = 860 \text{ nm}$ (Babic, 1993), the splitting values $2\hbar\Omega_{HHx} = 3.3 \text{ meV}$ and $2\hbar\Omega_{LHx} = 2.1 \text{ meV}$ are obtained, which are in reasonable agreement with our measurements.

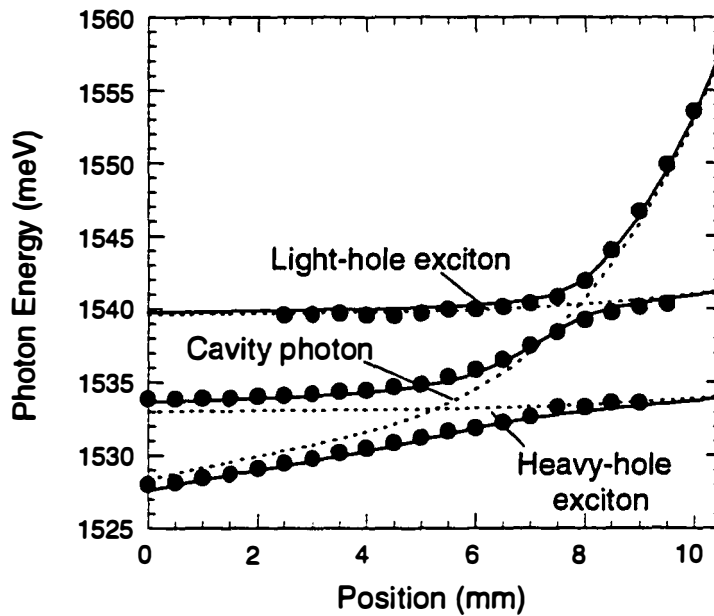


Fig. 2.17 Reflectivity vs. detuning by translation of the wafer. The dots are the measured energy minima at 10 K. The solid lines are the calculated eigenvalues. The dashed lines are curve fits to the measured functions $E_C(r)$, $E_{HHx}(r)$ and $E_{LHx}(r)$ of the bare states which are used as input parameters in the calculation.

In the same figure the calculated polariton energies (solid lines) and curve fits to the measurements of the uncoupled *bare states* vs. position (dashed lines) are presented. The cavity resonance energy $E_C(r)$ was measured by raising the temperature of the sample to 200 K (effectively decoupling the exciton and photon systems). The exciton resonance energies $E_{HHx}(r)$ and $E_{LHx}(r)$ were measured through PL measurements on a separately grown sample without Bragg mirrors. The calculated polariton energies are determined by solving the system of three coupled

differential equations. Two equations represent the LHx and HHx dipole oscillators (similar to Eq. (2.12)) and one equation represent the single cavity mode, Eq. (2.13).

In the PL measurements, the microcavity is excited non-resonantly with a CW GaAs semiconductor laser emitting at 780nm. Since the exciton peaks shift faster than the cavity mode as temperature is increased from 10 K to 140 K, the excitons can be tuned into resonance with the cavity, as can be observed in Figure 2.18. These measurements were performed at $r \approx 5.5$ mm, corresponding to a 0.41 meV detuning at 10 K. The dotted traces are the energy values of the measured luminescence peaks as a function of temperature detuning. Again, two anti-crossings are observed with the same separation as in the previous figure. On the same figure, the calculated energies and plots of the energies of the bare states vs. temperature $E_c(T)$, $E_{HHx}(T)$, and $E_{LHx}(T)$ are presented. $E_c(T)$ is a curve fit to the measurements of the cavity resonance vs. temperature made with the true empty cavity, whereas $E_{HHx}(T)$, and $E_{LHx}(T)$ were fitted to measurements of PL vs. temperature on the separate sample mentioned above.

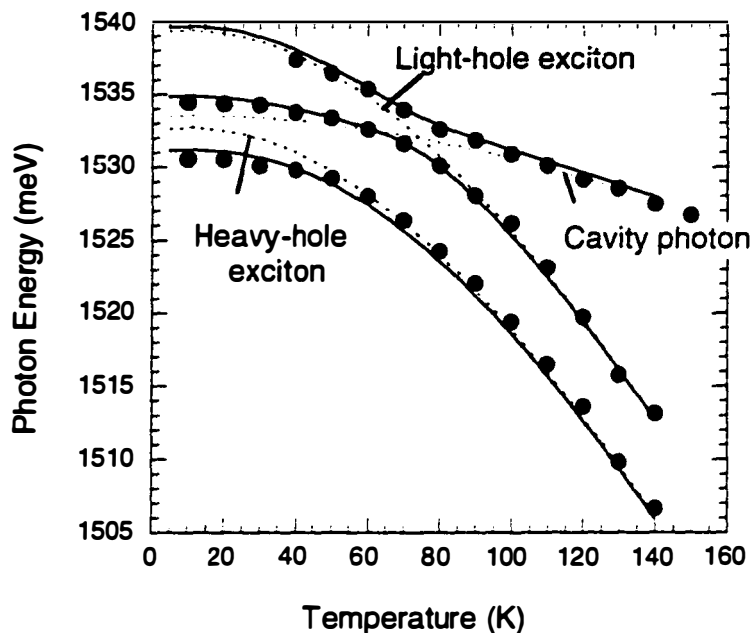


Fig. 2.18 Photoluminescence vs. detuning by changing the temperature of the sample. The dots are measured photon energies at a fixed position. The solid lines are the calculated eigenvalues. The dashed lines are curve fits to the measured functions $E_C(T)$, $E_{HHx}(T)$, and $E_{LHx}(T)$ of the bare states which are used as input parameters in the calculation.

The position and temperature dependence of the bare states $E_C(r, T)$, $E_{HHx}(r, T)$ and $E_{LHx}(r, T)$ were measured as explained above. The PL measurements on the QW sample, $E_{HHx}(r, T)$ and $E_{LHx}(r, T)$ were made at the center of the wafer only. It is assumed however that L_{QW} exhibits the same relative inhomogeneity vs. radial position on the wafer as the cavity does, such that $\delta L_{QW}(r)/L_{QW} = -\delta E_C(r)/E_{C0}$. In order to account for this effect the excitonic energies are corrected as

$$\delta E_i(r) = -\frac{\hbar^2 \pi^2}{m_R L_{QW}^2} \cdot \frac{\delta L_{QW}(r)}{L_{QW}}, \quad (2.31)$$

where $i = HHx$ or LHx . The reduced masses are $m_{R,LHx} = 0.037m_0$, and $m_{R,HHx} = 0.059m_0$, where m_0 is the electron mass in vacuum.

The agreement between the measured polariton energies and the coupled oscillator theory suggest that both excitons couple only to a single cavity mode. The 3.7 meV and 2.4 meV energy shift in the polariton spectra indicate the energy separation between neighboring momentum states. These shifts are two orders of magnitude large than for electron-hole pairs in a similar microcavity. The reduced momentum scattering and subsequent reduction in the number of accessible modes allows us to accurately model the polaritons with a system of only three oscillators. Single mode coupling is realized for these microcavity excitons.

2.5 Summary

In this chapter, we have discussed the alteration of spontaneous emission rates achievable with semiconductor microcavities. Our goal is to achieve single mode emission – to suppress spontaneous emission into all modes other than the lasing mode. As discussed in Chapter 1, increasing the efficiency implies reducing the total spontaneous emission rate and therefore the number of accessible modes. Semiconductor microcavities are severely limited in their ability to alter the spontaneous emission properties for free electron-hole pairs. Free electrons and holes can couple to photons with a broad range of momenta. This means that radiation into the passband and the angular dependence of the DBR reflectivity (the penetration depth) are both important to the spontaneous emission process. In an effort to limit the interaction of the oscillating charge with all nonresonant

plane waves, we have explored the possibility of isolating neighboring momentum states. This technique only works for dipoles with sufficiently strong field coupling that a significant energy shift could be realized. The large dipole moment for quantum well excitons makes them ideal candidates for this sort of ‘momentum space bandgap engineering.’ In fact, measurements on excitons within a semiconductor microcavity indicate that the excitons strongly interact with only a single plane wave mode. The strong interaction of the excitons with a single optical mode enabled the formation of polaritons.

The remainder of this thesis will explore coherent light generation by both electron-hole pairs and excitons within microcavities. The next chapter defines the advantages and further explores the practical limitations of achieving single mode lasers with free electron-hole sources. As we have described in this chapter, within a semiconductor microcavity only excitons are able to realize single mode emission. The consequences of using excitons (bosons) instead of electron-hole pairs (fermions) as the coherent light source is the focus of Chapter 4.

plane waves, we have explored the possibility of isolating neighboring momentum states. This technique only works for dipoles with sufficiently strong field coupling that a significant energy shift could be realized. The large dipole moment for quantum well excitons makes them ideal candidates for this sort of 'momentum space bandgap engineering.' In fact, measurements on excitons within a semiconductor microcavity indicate that the excitons strongly interact with only a single plane wave mode. The strong interaction of the excitons with a single optical mode enabled the formation of polaritons.

The remainder of this thesis will explore coherent light generation by both electron-hole pairs and excitons within microcavities. The next chapter defines the advantages and further explores the practical limitations of achieving single mode lasers with free electron-hole sources. As we have described in this chapter, within a semiconductor microcavity only excitons are able to realize single mode emission. The consequences of using excitons (bosons) instead of electron-hole pairs (fermions) as the coherent light source is the focus of Chapter 4.

NOTE TO USERS

Page(s) not included in the original manuscript are unavailable from the author or university. The manuscript was microfilmed as received.

UMI

Chapter 3

SEMICONDUCTOR MICROCAVITY LASERS

3.1 Microcavity Lasers

The semiconductor lasers used in CD players have cavity lengths – the distance between mirrors – of $300\mu\text{m}$ and waveguides measuring $3\mu\text{m}$ across and $1\mu\text{m}$ high. Relative to most gas and solid state lasers, semiconductor lasers are extremely small – approximately 10^{13} times smaller volume. For comparison, a bucket of water is 10^{13} times smaller than the Mediterranean Sea. Relative to the wavelength of light they emit, $0.85\mu\text{m}$, CD lasers are large. Since the refractive index of GaAs is approximately 3.5, the wavelength inside the optical cavity is only $0.24\mu\text{m}$. The laser cavity is approximately one thousand wavelengths long and almost one hundred square wavelengths in cross section. Before the onset of stimulated emission, the excited electrons in these lasers spontaneously emit light into approximately one million closely spaced cavity modes. All of these modes compete for photons and one eventually lases. From that point on, this one mode receives all of the additional photons radiated by the excited electrons. Competition for photons is not this tough in all semiconductor lasers.

Vertical cavity surface emitting lasers (VCSELs) have much smaller cavity volumes (Fig. 3.1). The cavity length is typically one wavelength. The short

cavity length ensures that there is only one longitudinal mode accessible to the excited electrons. The spacing between longitudinal modes is given by

$$\Delta\lambda = \frac{\lambda^2}{2L + \lambda}. \quad (3.1)$$

A GaAs VCSEL emitting at a wavelength of $0.98\mu\text{m}$ has a mode spacing of 93nm , or twice the width of the gain spectrum at room temperature. Associated with this single longitudinal mode are a continuum of radiation modes and several transverse modes that are accessible to the excited electrons. The dimensions of the waveguide determines the transverse mode structure. When the transverse dimension is only $0.1\mu\text{m}$, the microcavity is a true single mode cavity (Baba, 1991 and Vurgaftman, 1995). This mode does not have to compete for photons.

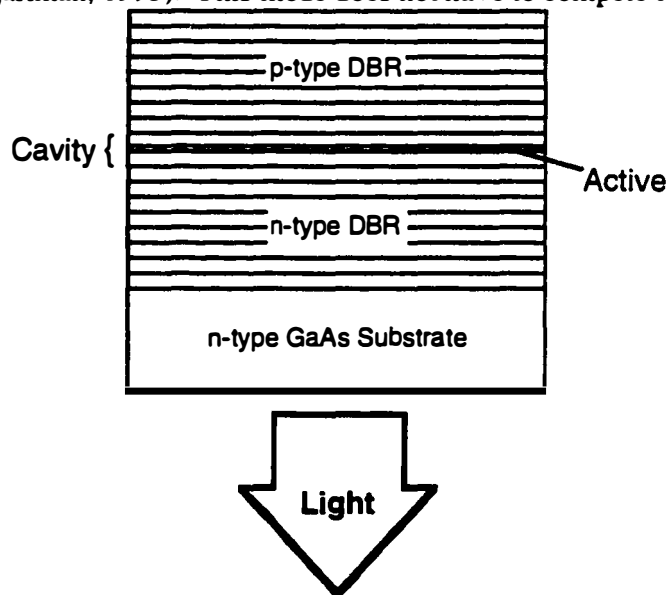


Fig. 3.1 Schematic of a surface emitting laser structure.

When studying semiconductor lasers, we must keep track of both the number of excited electrons and the number of photons. Energy is pumped into the

electrons by an injected current, I . This injected current consists of an excited electron that enters the active region and a low energy electron that leaves the active region. Neglecting nonradiative recombination processes and assuming a single mode cavity, the energy lost by the electron appears as light in the cavity mode either by spontaneous emission or stimulated emission. The stimulated emission rate is proportional to the number of photons already within the cavity mode whereas the spontaneous emission rate is independent of the photon number. These photons can either leave the cavity or be reabsorbed by low energy electrons. All of these processes are summarized by the following set of coupled rate equations for the excited electron (N) and photon number (P).

$$\begin{aligned}\frac{dN}{dt} &= \frac{\eta_i I}{q} - W_{st}P + W_{ab}P - W_{sp} \\ \frac{dP}{dt} &= W_{st}P - W_{ab}P + W_{sp} - \frac{P}{\tau_p}\end{aligned}\quad (3.2)$$

where $\eta_i I$ is the fraction of the injected current that enters the active region and τ_p is the lifetime of a photon in the optical cavity. Under steady state conditions ($d/dt = 0$), the two equations state that

$$P = \frac{\eta_i \tau_p}{q} I . \quad (3.3)$$

The photon number in the single mode is proportional to the injected current regardless of the emission mechanism, whether spontaneous emission or stimulated emission. The slope efficiency of a single mode laser without nonradiative recombination does not depend on the emission mechanism. Once energy is added to the device by the injected current it can only be removed by light generation into the single optical mode; spontaneous emission into other modes, lattice heating, or Auger processes are not options. This laser does not

have the turn-on or threshold of conventional multimode lasers which require stimulated emission for single mode operation. Realizing such a thresholdless laser in the laboratory requires small optical cavities which limit the number of modes. It also requires careful attention to processes such as surface recombination, diffusion out of the active region, trap and Auger recombination – essentially any process which competes with light generation into the single optical mode.

In Section 3.2, we introduce the general formalism for treating multimode semiconductor lasers. The formalism presented in this chapter corrects several inconsistencies in the treatment of spontaneous emission found in the literature. Section 3.3 discusses the potential benefits and limitations of true single mode lasers. Section 3.4 presents the first experimental analysis of the threshold process in lasers with small cavity volumes – only one hundred cubic wavelengths in volume. We also discuss the scaling of nonideal effects such as optical scattering and carrier diffusion as we reduce the cavity dimension.

3.2 Spontaneous Emission Factor

A theory for multimode semiconductor lasers can be constructed by extension of Equation (3.2). Additional modes result in the following coupled system of equations, one for the excited electrons and one for the photon number in each optical mode,

$$\begin{aligned}\frac{dN}{dt} &= \frac{\eta_i I}{q} - \sum_m W_{st,m} P_m + \sum_m W_{ab,m} P_m - \sum_m W_{sp,m} \\ \frac{dP_m}{dt} &= W_{st,m} P_m - W_{ab,m} P_m + W_{sp,m} - \frac{P_m}{\tau_{p,m}}\end{aligned}\quad (3.4)$$

In steady state, the total power in all of the optical modes is again proportional to the injected electrical current

$$\sum_m \frac{P_m}{\tau_m} = \frac{\eta_i I}{q} \quad (3.5)$$

Collection of light from all optical modes is not possible for conventional semiconductor lasers. The finite size of the detector used to collect the laser light and the scattering and absorption of light by the electrical contacts and the measurement apparatus make collecting all of the light nearly impossible. The light in only a few cavity modes reaches the detector. After all, we design the measurement apparatus to collect light primarily from the lasing mode. If we designate P_0 as the photon number in the lasing mode and assume that the photon number for all other modes is small, we can reduce the large system of equations to only two equations,

$$\begin{aligned}\frac{dN}{dt} &= \frac{\eta_i I}{q} - W_{st,0} P_0 + W_{ab,0} P_0 - \sum_m W_{sp,m} \\ \frac{dP_0}{dt} &= W_{st,0} P_0 - W_{ab,0} P_0 + W_{sp,0} - \frac{P_0}{\tau_p}\end{aligned}\quad (3.6)$$

Because the number of photons in the nonlasing modes is small, we have neglected their absorption and stimulated emission. Spontaneous emission into these modes, however, cannot be neglected.

In the literature, this simple formalism has been complicated by the introduction of a spontaneous emission factor (Yamamoto, 1991 and Yokoyama,

1992). The spontaneous emission factor represents the fraction of spontaneous emission that enters the lasing mode

$$\beta = \frac{W_{sp,0}}{\sum_m W_{sp,m}}. \quad (3.7)$$

When the excited electrons radiate the same amount of spontaneous emission into every accessible cavity mode, the spontaneous emission factor can be approximated as the reciprocal of the total number of modes (M)

$$\beta = \frac{W_{sp}}{\sum_m W_{sp,m}} = \frac{W_{sp}}{\sum_m W_{sp}} = \frac{1}{M}. \quad (3.8)$$

This approximation is only useful for lasers with many closely spaced cavity modes at nearly the same transition energies.

The above rate equations can be expressed in terms of the spontaneous emission factor

$$\begin{aligned} \frac{dN}{dt} &= \frac{\eta_l I}{q} - W_{st,0} P_0 + W_{ab,0} P_0 - \sum_m W_{sp,m} \\ \frac{dP_0}{dt} &= W_{st,0} P_0 - W_{ab,0} P_0 + \beta \sum_m W_{sp,m} - \frac{P_0}{\tau_p} \end{aligned} \quad (3.9)$$

It is truly unfortunate that the semiconductor laser community has adopted a formalism which replaces the single term in (3.6) with the ratio of two summations. In order to conform to the published literature we will use the spontaneous emission factor.

Rate Equation Analysis

So far, we have not considered the specific light emission processes in semiconductor media. The rate equations expressed above have not explicitly

stated a dependence of either W_{st} , W_{ab} , and W_{sp} on the number of excited electrons. In this chapter, we are interested in small cavity lasers (Fig. 3.1). The laser cavity consists of two high reflectivity distributed Bragg reflectors (DBRs). These mirrors are separated by a cavity length of one wavelength, $0.3\mu\text{m}$ at the lasing wavelength of $0.98\mu\text{m}$. The excited electrons responsible for light emission are confined to InGaAs quantum wells. In order to model the performance of these lasers we must consider the electronic band structure of the semiconductor and the distribution of the electrons in these bands. Following the treatment of (Coldren 1995), we develop the concepts of bimolecular recombination, logarithmic gain models and gain saturation.

The rate of spontaneous emission into all optical modes is usually modeled as a bimolecular process – $\sum_m W_{sp,m} = BN^2$. The total spontaneous emission rate increases quadratically with the density of excited electrons. As more excited electrons enter the active region of the laser they distribute themselves over a greater range of kinetic energies. Figure 3.2 shows the spontaneous emission spectra versus electron density calculated in (Coldren, 1995). Increasing the electron density increases the number of electrons at high kinetic energies. These electrons can emit into cavity modes that were not previously accessible thereby opening new pathways for spontaneous emission. Not only the value of the bimolecular recombination coefficient, but also the quadratic dependence of the spontaneous emission rate relies on the existence of optical modes into which the electrons can radiate. Here, we consider lasers with relatively large transverse cavity dimensions so there are enough accessible modes to justify the bimolecular recombination model.

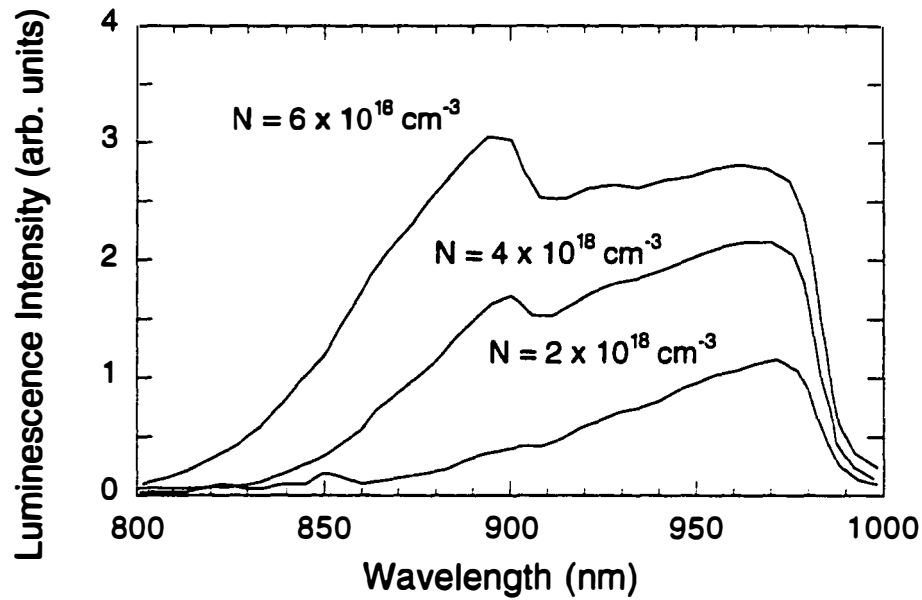


Fig. 3.2 Spontaneous emission spectra for various densities of excited electrons. The spontaneous emission spectrum broadens as the total electron density increases.

Stimulated emission and absorption both depend linearly on the number of photons in the optical mode. The conventional rate equation analysis lumps these two processes into a single gain term; $W_{st} - W_{ab} = \nu_g g(N)$. Since this gain is expressed in units of inverse centimeters the group velocity of the photons is used to establish a net photon generation rate. In a simple two level model – which is generally not applicable to semiconductor media, the stimulated emission rate is $W_{st} = \nu_g K N_2$ and the absorption rate is $W_{ab} = \nu_g K N_1$ where K is a constant of proportionality. The net gain is $g = K(N_2 - N_1)$. We can recover the stimulated emission rate from the net gain by using the population inversion factor (n_{sp}); $W_{st} = n_{sp} \nu_g g$. This equation defines the population inversion factor. For example, the population inversion factor for the two level system is $n_{sp} = N_2 / (N_2 - N_1)$.

As the relative number of excited electrons increases the population inversion factor approaches unity. In a semiconductor, the net gain has a nontrivial dependence on the electron density. Figure 3.3 shows the net gain versus carrier density for an 80Å InGaAs quantum well. The figure shows the gain seen by a single mode at a well defined frequency. Initially the increase in the overall number of excited electrons also causes an increase in the number of electrons that emit into the optical mode. As the electron density increases, the electronic states that coincide with this optical mode become full and the gain starts to saturate. This density dependence is often approximated by a logarithmic gain function – $g(N) = g_0 \ln \left[\frac{N + N_s}{N_{tr} + N_s} \right]$ (Corzine, 1990).

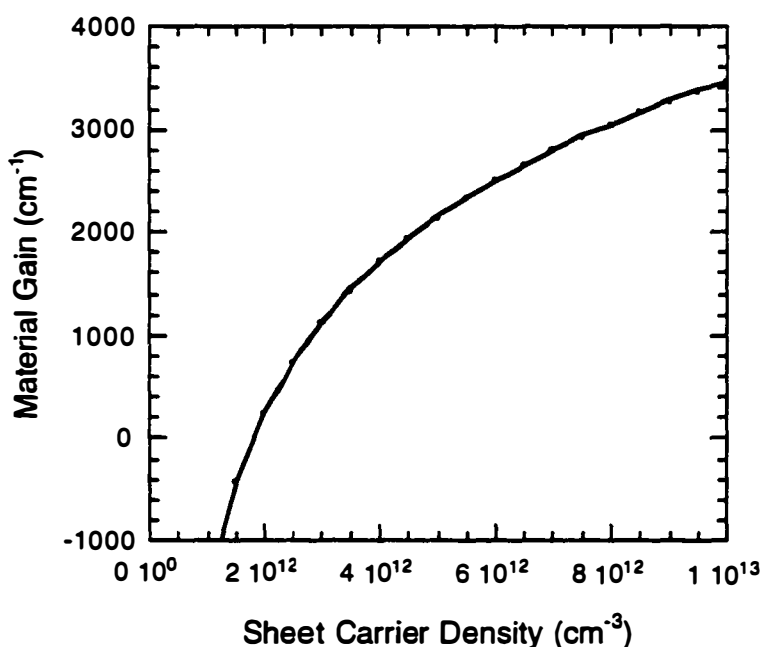


Fig. 3.3 Net gain versus the density of excited electrons.

The bimolecular recombination model, the net gain and the spontaneous emission factor can all be used to generate the conventional multimode rate equations for the excited electron and photon numbers (N and P_0) and densities (n and p_0).

$$\begin{aligned}\frac{dN}{dt} &= \frac{\eta_i I}{q} - v_g g(N) P_0 - BN^2 \\ \frac{dP_0}{dt} &= \Gamma v_g g(N) P_0 + \Gamma \beta BN^2 - \frac{P_0}{\tau_p}\end{aligned}\quad (3.10)$$

$$\begin{aligned}\frac{dn}{dt} &= \frac{\eta_i I}{q V_{ac}} - v_g g(n) p_0 - B' n^2 \\ \frac{dp_0}{dt} &= \Gamma v_g g(n) p_0 + \Gamma \beta B' n^2 - \frac{p_0}{\tau_p}\end{aligned}\quad (3.11)$$

where Γ is the confinement factor and V_{ac} is the active region volume. The two bimolecular recombination coefficients are related according to $B' = V_{ac} B$. These rate equations are given for both the excited electron number and the photon number as well as the electron and photon densities.

Spontaneous Emission Factor

By definition β is the fraction of radiative current contributing to spontaneous emission into the lasing mode: $\beta = (I_{sp}|_{laser}) / (I_{sp}|_{total})$. The spontaneous emission rate into the lasing mode is equal to the stimulated emission rate when the cavity contains a single photon; therefore $\beta = I_{st}|_{P_0=1} / I_{sp}|_{total}$.

For the simple case of a linear gain model,

$$g(N) = g_o(N - N_o), \quad (3.12)$$

and a constant carrier lifetime,

$$\sum_m W_{sp.m} = \frac{N}{\tau_{sp}}, \quad (3.13)$$

the expression reduces to the well known form (Bjork, 1991)

$$\begin{aligned}\beta &= \frac{I_{st}|_{p_0=1/V_{cm}}}{I_{sp}|_{total}} = n_{sp} \frac{g_o(N - N_o)v_R}{V_{cav}N/\tau_{sp}} \\ &= \frac{N}{N - N_o} \frac{g_o(N - N_o)v_R}{V_{cav}N/\tau_{sp}} = \frac{g_o v_R \tau_{sp}}{V_{cav}}\end{aligned}\quad (3.14)$$

where, g_o is the gain coefficient, N_o is the transparency carrier density, and τ_{sp} is the spontaneous lifetime. The microcavity alters both the confinement factor and the total spontaneous emission rate. For this simple model, β is found to be independent of electron density – as the electron density increases, the emission into the lasing mode and the total spontaneous emission rate increase by the same amount.

A realistic gain model, however, shows that β decreases with increasing electron density. Using bimolecular recombination and a logarithmic gain model we see that (Ram, 1996)

$$\beta = \frac{I_{st}|_{p_0=1/V_{cm}}}{I_{sp}|_{total}} = n_{sp} \frac{g_o \ln \left[\frac{N + N_s}{N_{tr} + N_s} \right] v_R}{V_{cav} B N^2} . \quad (3.15)$$

The spontaneous emission coupling factor explicitly depends on the carrier density. As the electron density increases, the spontaneous emission spectrum broadens and the gain saturates. Figure 3.4 plots the spontaneous emission factor versus carrier density for a typical InGaAs quantum well surface emitting laser.

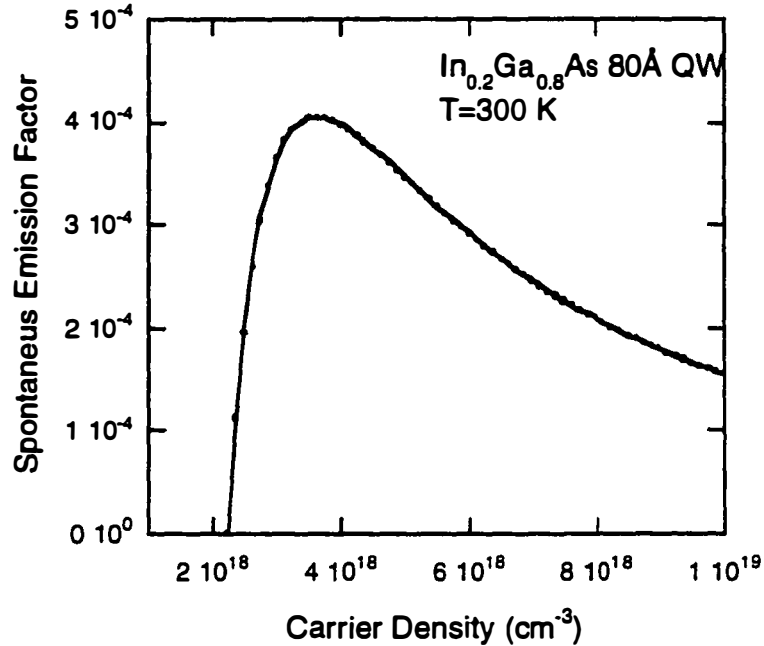


Fig.3.4 The spontaneous emission factor versus the density of excited electrons.

The spontaneous emission factor increases as the cavity volume decreases. This is because the peak field amplitude for a single cavity photon increases as the cavity shrinks. The increased field amplitude results in a larger electron-photon coupling and a subsequent increase in the gain and spontaneous emission rate into the optical mode. The explicit volume dependence in (3.15) is a result of this enhanced interaction. In addition to this explicit dependence on cavity size, there is an implicit dependence in the bimolecular recombination coefficient. A small cavity offering only a few accessible cavity modes will have a smaller recombination coefficient (spontaneous emission rate) and a larger β .

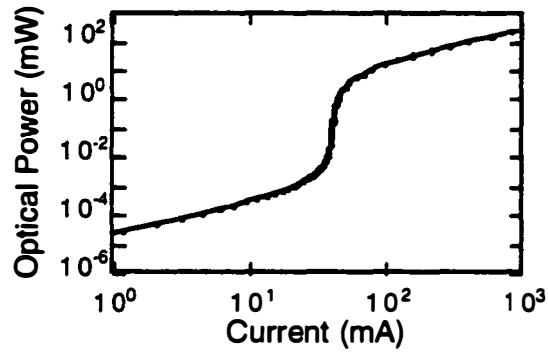
Microcavity lasers attempt to optimize β by exploiting this implicit dependence on the cavity volume.

3.3 Thresholdless Lasers ?

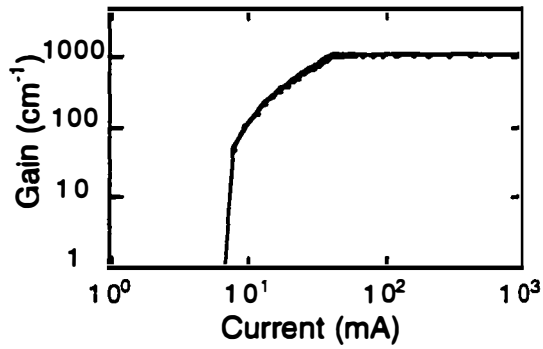
Of all device parameters, laser threshold is most sensitive to changes in the spontaneous emission factor. Laser threshold is defined by a balance between the exponential increase in photon number due to stimulated emission and the loss of photons due to scattering and finite reflectivity mirrors (Siegman, 1986)

$$\Gamma g(N) \nu_r = \frac{1}{\tau_p}. \quad (3.16)$$

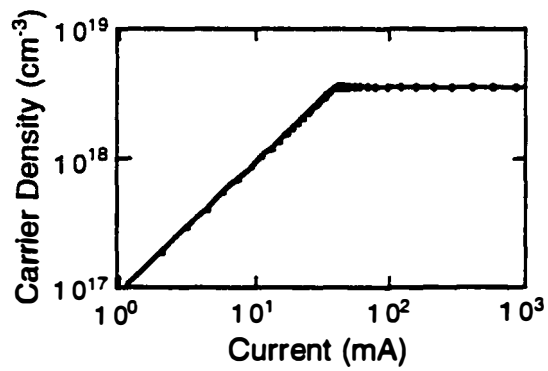
If the rate of photon generation could exceed the optical losses, stimulated emission would cause a 'runaway' in the number of photons. Such an exponentially increasing photon number cannot be supported by the finite number of excited electrons supplied by the injection current. The net steady-state gain can never exceed the threshold gain defined by (3.16). The excited electron density cannot exceed the density corresponding to this threshold gain. Figure 3.5 shows the optical power, net gain, and carrier density versus the injection current for a conventional InGaAs laser with $\beta = 10^{-6}$. Indeed, the electron density and net gain appear to clamp at their threshold values. Coincident with the clamping of the electron density is a rapid increase in the efficiency of photon generation in the lasing mode. The stimulated emission rate into the lasing mode at this threshold point is so high that any additional electrons supplied by the injection current are quickly converted into photons in the lasing mode. Laser threshold essentially defines the electron density required to obtain single mode emission.



(a)



(b)



(c)

Fig. 3.5 (a) Optical power, (b) excited electron density, and (c) net gain versus injection current for a conventional edge-emitting laser structure with a $\beta=10^{-4}$.

The above analysis is *not* applicable to true single mode microcavity lasers without nonradiative recombination. Equation (3.16) overestimates the excited electron density required for nearly single mode emission. Figure 3.6 shows the photon number and carrier density versus injection current for various β , but the same optical loss. A microcavity with only a single accessible optical mode ($\beta = 1$) always has single mode emission regardless of the carrier density. Threshold is not a meaningful concept in this case. As we show below, the threshold condition expressed in Eq. (3.16) is only valid in the limit $\beta \rightarrow 0$.

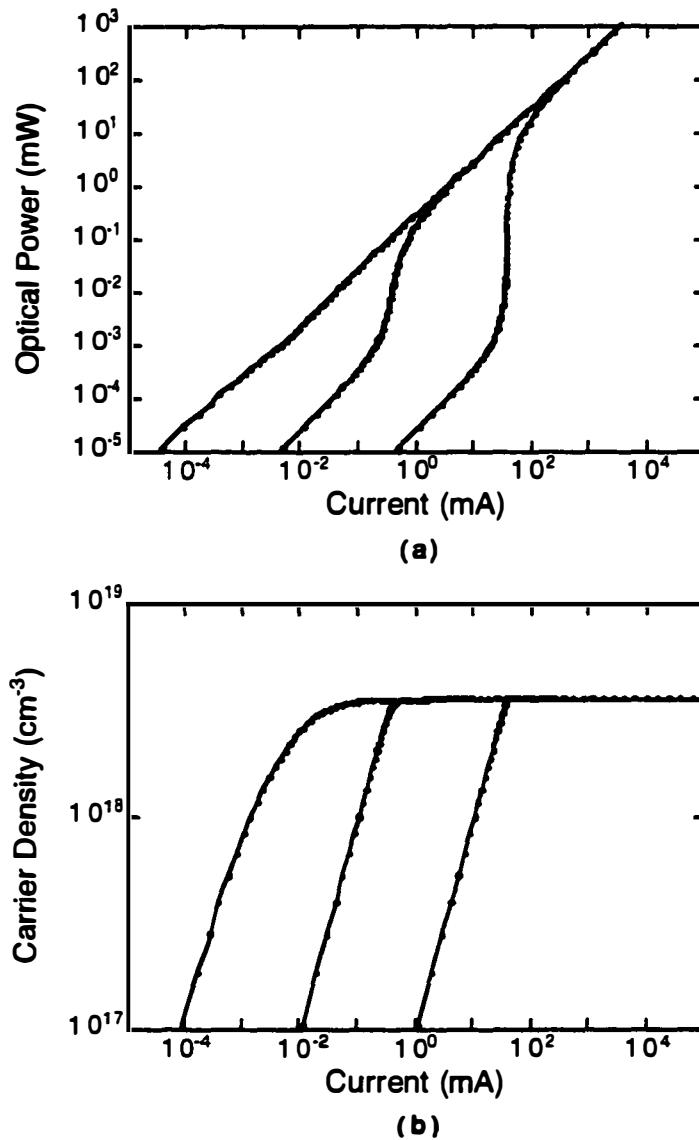


Fig. 3.6 (a) Optical power and (b) excited electron density versus the injection current. The results for various spontaneous emission factors ($\beta=1, 10^{-2}$, and 10^{-4}) are plotted.

The flaw in the above threshold condition is that it neglects the contribution to the steady state photon number coming from spontaneous emission into the lasing

mode. As we stated above, laser threshold is defined by the balance of emission into the lasing mode and optical losses. The 'gain equals loss' condition assumes that the photons are added to the lasing mode only by stimulated emission - in fact there is always some spontaneous emission also contributing photons to the lasing mode. Real lasers never satisfy (3.16) since this would involve having more photon generation (stimulated and spontaneous emission) than loss and would lead to runaway. The steady state photon density in the lasing mode, as obtained from (3.11), can be expressed as

$$p_0 = \frac{\Gamma \beta B' n^2}{\frac{1}{\tau_p} - \Gamma \nu_s g(N)}. \quad (3.17)$$

There is a singularity in the photon number when the net gain equals the loss. In fact, the net gain asymptotically approaches the total optical losses; the kink in the light versus injected current curves always coincides with a net gain smaller than the optical losses.

3.4 Limits to Practical Laser Performance

Reducing the number of accessible optical modes reduces the energy wasted in a laser. The energy saved by eliminating spontaneous emission into nonlasing modes can be used to generate light in the lasing mode. Realizing this in semiconductor lasers requires small cavity volumes and weak nonradiative recombination. Nonradiative processes such as Auger recombination, surface recombination, and carrier diffusion can frustrate any efforts to improve the below threshold efficiency of microcavity lasers. Reducing the number of optical modes is not helpful if a large amount of energy is being wasted through nonradiative

processes. Without nonradiative recombination the fraction of the injected energy appearing the lasing mode below threshold is β . Additional recombination pathways reduce this fraction to $\eta_r\beta$ – where η_r is the fraction of the excited electrons that relax by emitting photons

$$\eta_r = \frac{\sum_m W_{sp,m}}{W_{Auger} + W_{surface} + W_{diffusion} + \sum_m W_{sp,m}}. \quad (3.18)$$

Figure 3.7 shows the photon number versus injection current for a laser with a radiative efficiency less than one. There is a distinct threshold even for a true single mode laser.

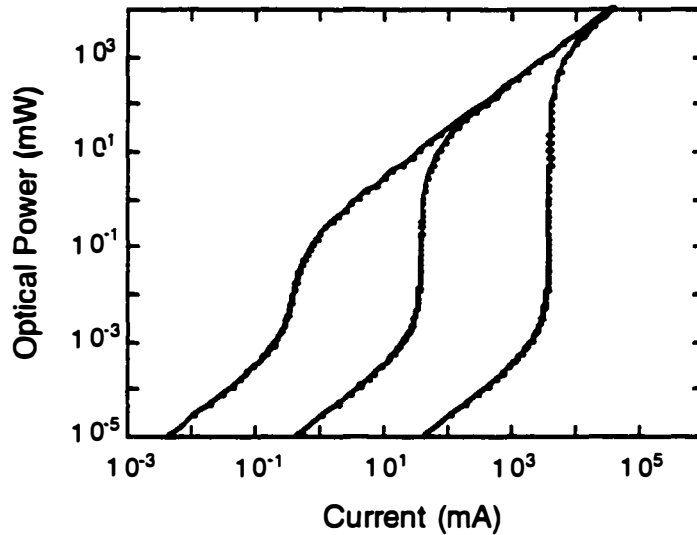


Fig. 3.7 Optical power versus injection current for microcavities with various spontaneous emission factors ($\beta=1, 10^{-2}$, and 10^{-4}). The below-threshold radiative efficiency is 1%.

In the following section, we study laser threshold in small surface emitting lasers. These lasers were grown and processed by Matt Peters at UCSB (Goobar,

1995). The measured devices have cylindrical post geometries where the top mirror has been etched to the top cladding layer (Fig. 3.8). Etching only to the cladding layer provides optical confinement of the spontaneous emission while avoiding non-radiative surface recombination (Peters, 1994). The n-type bottom mirror consists of 16.5 AlAs/GaAs periods. The p-type mirror consists of 30 periods of $\text{Al}_{0.67}\text{Ga}_{0.33}\text{As}/\text{GaAs}$ layers. In order to lower operating voltages and minimize heating effects, the mirrors have utilized graded heterointerfaces and dipole doping. The active region consists of $0.12\ \mu\text{m}$ $\text{Al}_{0.5}\text{Ga}_{0.5}\text{As}$ confinement layers surrounding a gain region with three $8\ \text{nm}$ $\text{In}_{0.185}\text{Ga}_{0.815}\text{As}$ QWs with $8\ \text{nm}$ GaAs barriers.

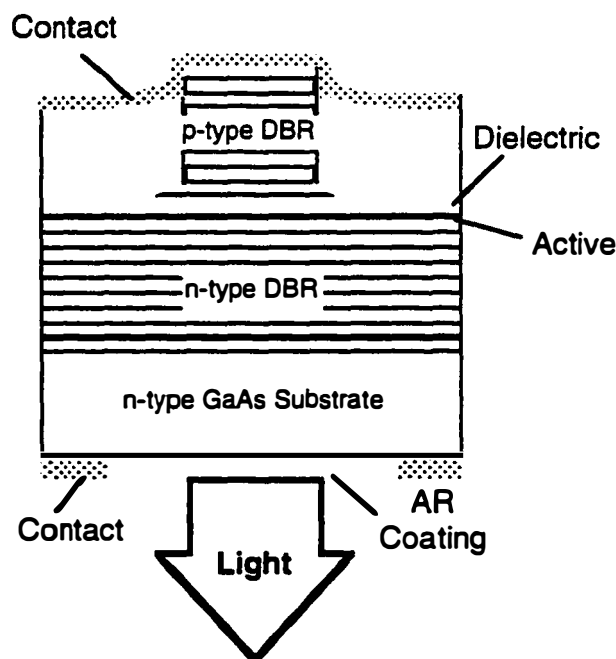


Fig. 3.8 Schematic of the measured device.

These devices were designed for low temperature operation in the 71-150 K range. Optimization for low temperatures requires adjusting the cavity length so as to ensure that the cavity mode is aligned to the strongest electronic transition at the desired operating temperature. In Appendix II, we summarize the temperature dependence of the cavity's resonant wavelength and the peak wavelength of the electronic transition. Low temperature operation helps to increase both β and η_i . The range of kinetic energies over which the excited electrons are distributed is reduced at low temperature. This, in turn, reduces the width of the spontaneous emission spectra and limits the number of accessible optical modes. The reduction in the number of high kinetic energy electrons also reduces the rate of Auger and trap assisted nonradiative recombination. The cryogenic operating temperature and the absence of surfaces near the active region eliminates many undesirable recombination pathways. This cavity design is expected to improve the below threshold efficiency of the semiconductor laser.

Measuring Spontaneous Emission Factor

In order to measure β , the lasers are mounted (top-side down) on a cold finger cryostat. The measurement geometry is shown in Figure 3.9. A 50 μm multimode optical fiber (NA=0.2) is positioned several millimeters below the sample to spatially filter the spontaneous emission. Spectral filtering is achieved by adjusting the resolution bandwidth (RBW=0.2 nm) of an optical spectrum analyzer. This allows us to measure only the spontaneous emission into the lasing mode. The measurements performed using large resolution bandwidths are underfiltered so that light from several nonlasing modes is also collected. In this

case, the light versus injection current exhibits smaller discontinuities at threshold. On the other hand, overfiltering the laser mode (i.e. reducing the resolution bandwidth until the above threshold emission is cutoff) does not affect the shape of the light versus injected current curve. Figures 3.10 and 3.11 display the light versus current characteristics of two devices with 9- and 3- μm diameters, respectively.

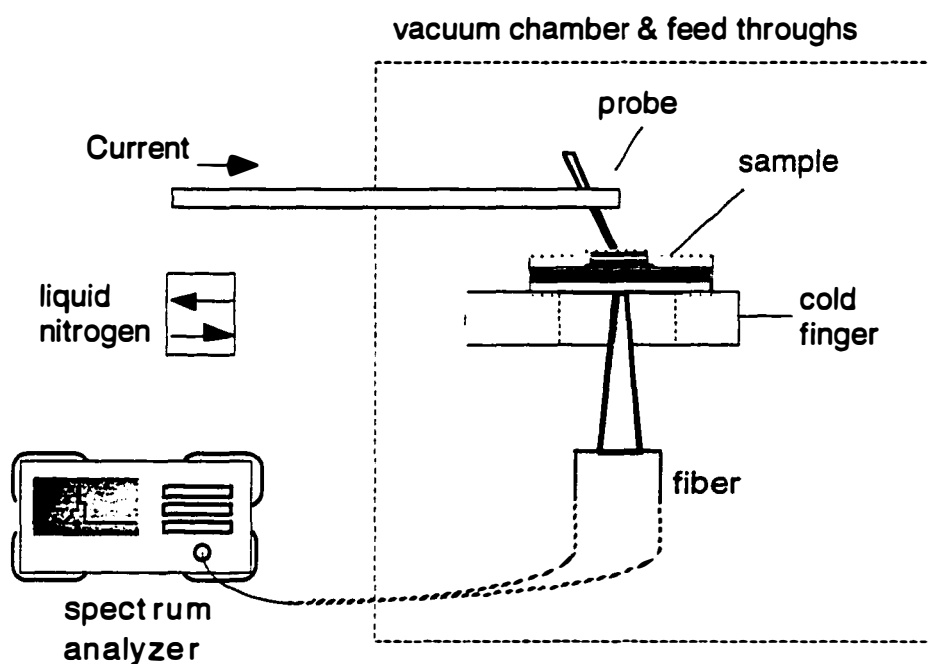


Fig. 3.9 The measurement set-up

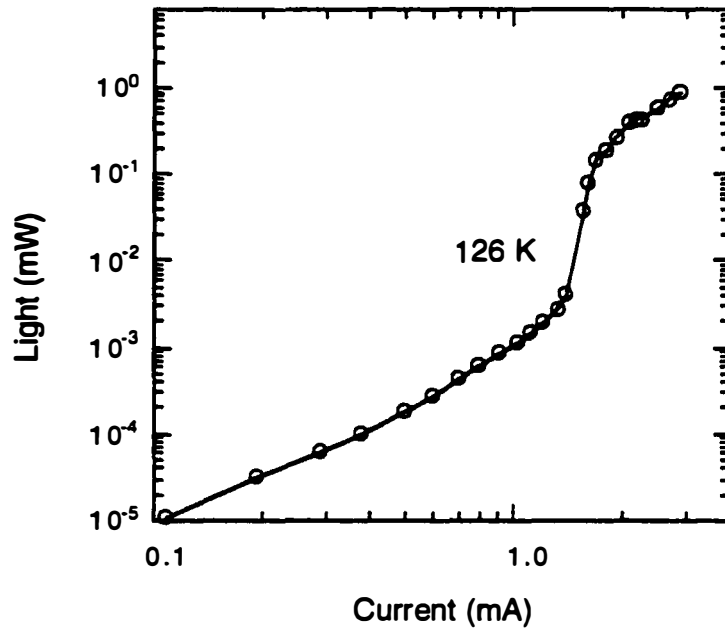


Fig. 3.10 Light versus current for a 9- μm diameter device at a heat-sink temperature of 126 K (optimal detuning).

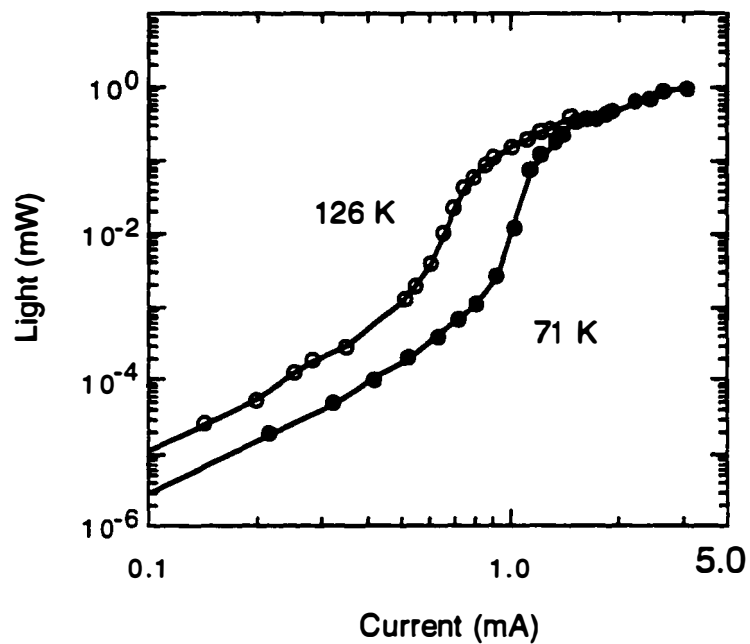


Fig. 3.11. Light versus current for a 3- μm diameter device at a heat-sink temperature of 126 K (optimal detuning) and 71 K.

It can be seen from Equation (3.15) that β is a bias dependent quantity. Below threshold the differential efficiency is the product of the injection efficiency, the radiative efficiency (η_r), and the spontaneous emission coupling factor. The radiative efficiency of the measured lasers is limited by carrier diffusion out of the cavity. The carrier lifetime decreases as the photon number and stimulated recombination rate increase. At the lasing threshold the radiative efficiency changes abruptly to nearly one; the carrier lifetime becomes so short that the excited electrons do not have time to diffuse out of the active region. Since the threshold transition takes place over a small change in carrier density

(for $\beta < 0.1$), β at threshold can be estimated by measuring the ratio of the differential efficiency immediately above and below the lasing threshold. $\eta_r \cdot \beta$ is one-half the change in the differential efficiency since light from two orthogonally polarized modes is collected below threshold whereas lasing occurs in a single polarization.

Fig. 3.10 shows light versus bias current measurements for a cavity with a 9 μm diameter post. $\eta_r \cdot \beta$ is $2(\pm 1) \times 10^{-3}$ with optimal gain-cavity detuning (at a heatsink temperature of 126 K). Optimal detuning is determined by measuring the threshold current as a function of temperature (Fig. 3.12). Optimal detuning occurs for the temperature at which the cavity mode is aligned to the peak of the gain spectrum. In Fig. 3.11 light versus current measurements are shown for a cavity with a 3 μm diameter post. $\eta_r \cdot \beta$ is $4(\pm 1) \times 10^{-3}$ at 126 K (also optimal gain-cavity coupling). In order to determine β , the influence of carrier diffusion must be considered.

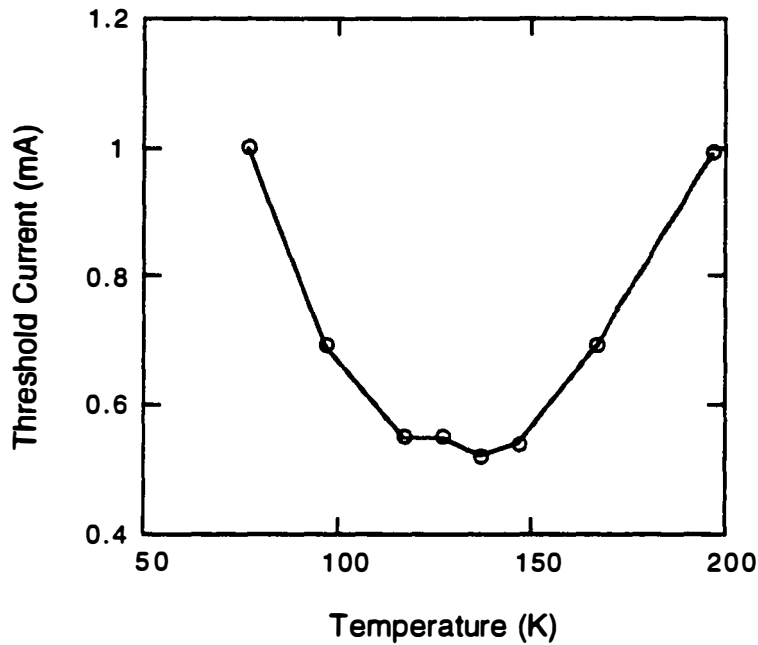


Fig. 3.12. Measured threshold current versus heat-sink temperature for a 3- μm diameter device. The optimal detuning is realized at a temperature of 126 K.

Extraction of Radiative Efficiency and Spontaneous Emission Factor

The radiative efficiency is the fraction of the total injected current that supports the generation of light,

$$\eta_r = \frac{I_{rad}}{I} = \frac{I_{rad}}{I_{rad} + I_{diff}}. \quad (3.19)$$

I is the measured injection current and I_{rad} is the current supporting the spontaneous and stimulated emission of light. Equation (3.19) assumes that diffusion is the only nonradiative carrier loss mechanism. As the device diameter becomes larger, $\eta_r \rightarrow 1$ and $I \rightarrow I_{rad}$. The above experiments measure $\eta_r \cdot \beta$ at threshold. η_r at threshold is the ratio of the current needed to maintain the

threshold carrier density in the absence of diffusion to the measured threshold current. The threshold carrier density can be extracted from the measured differential efficiency and the estimated gain dependence on the carrier density. The current required to maintain this threshold density (I_{rd}) can be approximated by using a model for the carrier losses in the absence of diffusion, i.e. the bimolecular recombination model.

Using extracted optical losses and established gain curves (Corzine, 1990) we obtain the threshold carrier density. The total optical losses (L_{tot}) versus device diameter (d) were extracted from the measured differential efficiencies (η_d)

$$L_{tot}(d) = T \left(\frac{\eta_i}{\eta_d(d)} - 1 \right). \quad (3.20)$$

T is the transmission calculated for a planar 16.5 period AlAs/GaAs mirror. η_i is again the injection efficiency which is typically a weak function of the device diameter. Figure 3.13 shows the extracted optical losses along with a numerical fit (Thibeault, 1995)

$$L_{tot} = L_{bu} + L_{scat} = 0.74 + \frac{9.56}{d^2} [\%]. \quad (3.21)$$

Here L_{bu} is the broad area round trip cavity loss and L_{scat} is the size dependent cavity loss. The total optical losses are 1.6 % and 0.9 % for the 3 μm and 9 μm devices, respectively. These are in agreement with scattering losses for similar devices at room temperature. These optical losses can be attributed to the scattering at the perimeter of the etched post (Fig. 3.14). The chemical component of the etch used to define the post results in unequal etch rates for AlAs and GaAs. This etching results in a scalloped profile which efficiently scatters light out of the optical cavity.

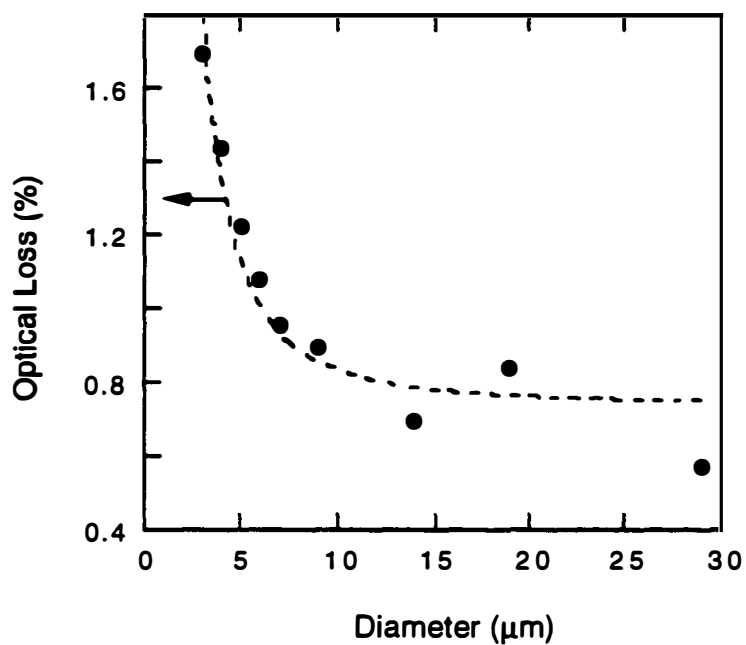


Fig. 3.13 The estimated optical losses versus post diameter. The optical losses follow an inverse square law with the device diameter (shown as a dotted line).

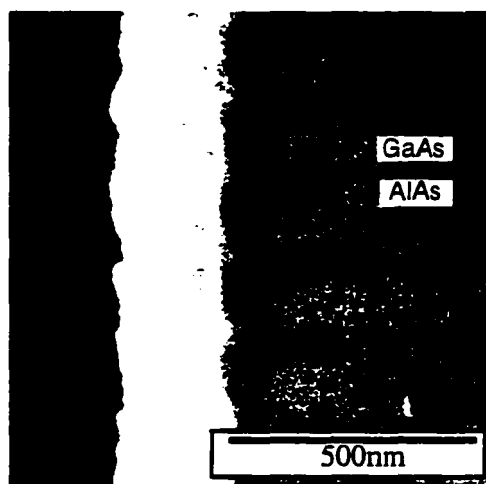


Fig. 3.14 A scanning electron micrograph of an etched post. The micrograph clearly shows roughness due to the different etch rates in GaAs and AlAs.

The threshold carrier densities can be estimated from the gain model described earlier; this gain model has been verified by low temperature measurements on conventional edge-emitting lasers (Hu, 1995). The current required to maintain the threshold carrier density without diffusion is estimated using the established bimolecular recombination model and the extracted threshold carrier density. The radiative efficiency is the ratio of this estimated threshold current with the measured threshold current. Figure 3.15 shows the radiative efficiencies for various device diameters. The estimated efficiencies are in agreement with diffusion currents predicted by a self-consistent numerical model for this device structure (Thibeault, 1995).

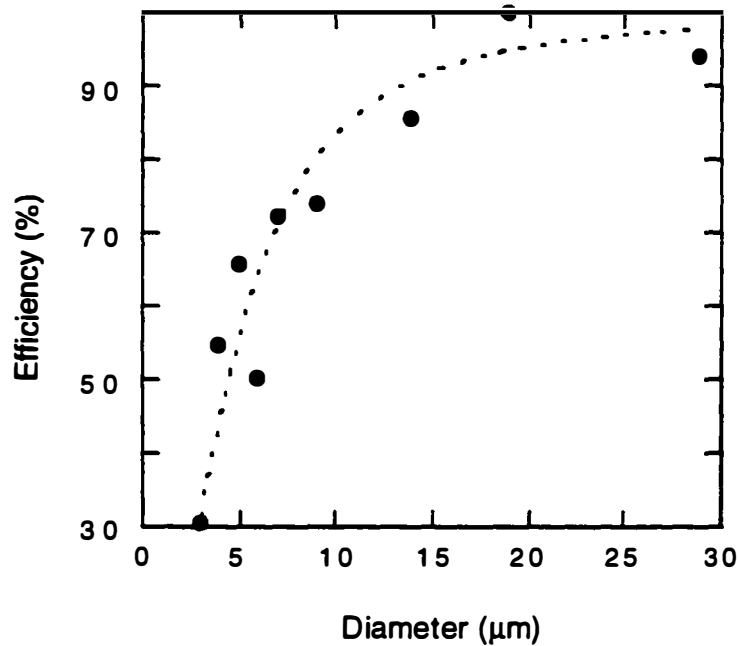


Fig. 3.15 The estimated radiative efficiency versus post diameter. The dotted line is intended only as a guide to the eye.

The extracted β are 1×10^{-2} and 2.5×10^{-3} for the $3 \mu\text{m}$ and $9 \mu\text{m}$ devices, respectively. Figure 3.16 shows the measured values of β as well as the values predicted by Equation (3.15) utilizing the estimated threshold carrier densities. The bimolecular recombination coefficient used in the model was independent of device diameter, i.e. microcavity effects are insignificant. The measured values appear to be in reasonable agreement with the predictions of Equation (3.15). All of the parameters that appear in (3.15) are required to model the threshold and differential efficiency of semiconductor lasers. The spontaneous emission factor is not a fitting parameter; the threshold carrier density and therefore β – from Equation (3.15) – can be extracted from the measured threshold current and differential efficiency.

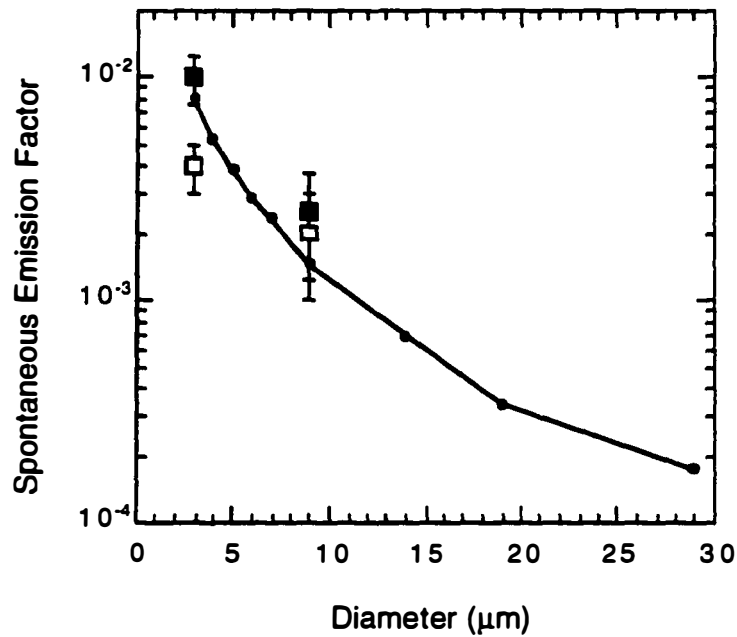


Figure 3.16. Calculated β incorporating measured values for optical losses and radiative efficiencies. Also shown are measured values of β for 3- μm and 9- μm diameter devices (filled squares) and the measured values of η, β (empty squares).

3.5 Summary

In conclusion, we have measured the spontaneous emission coupling factor in electrically-pumped post vertical cavity lasers. We have examined limitations to the enhancement of β in practical microcavities. Reducing the lateral dimensions of the optical cavity increases the frequency separation between neighboring optical modes and reduces the number of accessible optical modes within a given frequency bandwidth. This results in a decrease in the bimolecular recombination coefficient as the volume decreases. We find that even though the bimolecular

recombination coefficient may decrease with the cavity volume, the total spontaneous emission rate does not decrease. The small diameter lasers are strongly influenced by scattering losses in the etched post. The increased optical losses for smaller diameter devices require larger threshold carrier densities. The spontaneous emission spectrum broadens as the carrier density increases and the resulting number of accessible modes actually increases. Also, the larger carrier density increases the probability for an excited electron to find an empty valence band state into which it can relax. Both effects increase the total spontaneous emission rate and also the total amount of energy wasted by spontaneous emission into nonlasing optical modes. A second limitation to scaling the optical resonator is carrier losses due to surface recombination or diffusion. In the measured devices, we saw that the fraction of current contributing to radiative transitions decreases with the device dimensions. This reduction in the radiative efficiency frustrates the central goal of microcavity laser research which is to increase the below threshold efficiency of semiconductor lasers.

Our analysis suggests that improvements to device geometry which reduce the threshold carrier densities will naturally increase the spontaneous emission coupling factor. In the immediate future, enhancement of the spontaneous emission factor in the new class of 'oxide hole' surface emitting lasers is expected (Choquette, 1996). These devices realize extremely low threshold currents by successfully scaling the active region diameter to micron dimensions. These devices rely primarily on current confinement and not on optical confinement. As such they neither introduce significant optical losses nor do they alter the bimolecular recombination coefficient. Even without microcavity effects the low

86

threshold carrier densities translate into lower total spontaneous emission rates and higher spontaneous emission factors.

Chapter 4

MICROCAVITY POLARITON LASERS

4.1 Polariton Matter Lasers

Excited electrons in a small enough optical cavity spontaneously emit light into a single optical mode. Photons generated by spontaneous emission into this single mode exhibit the directionality and spectral purity characteristic of laser light. Restricting the interaction of the excited electrons to only a single mode eliminates the usual turn-on associated with single mode emission resulting from laser action. The electrons in typical microcavity semiconductor lasers interact more strongly with other electrons at different momenta than with the optical mode – momentum scattering times are typically 1 ps (Wang, 1995) and spontaneous emission times are 5 ns in GaAs. When the interaction between the electrons and the optical mode is sufficiently strong, the nature of spontaneous emission by the electrons changes drastically. In Chapter 2, we showed that the strong-coupling limit could be achieved by placing excitons in a small DBR microcavity. The system of coupled excitons and cavity photons is called a

polariton. There are two polariton branches that represent the additive and subtractive superposition of exciton and photon states. Creating a polariton requires the simultaneous generation of an exciton and a photon that are coupled together. Destroying a polariton means destroying a coupled exciton and photon. Light emission from a strong-coupling microcavity, therefore, involves the annihilation of polaritons. The microcavity polariton laser, or boser, is a device that uses polaritons to generate coherent light.

Coherent light emission from a conventional multimode laser requires stimulated photon emission. Stimulated emission causes an excited electron to emit a duplicate of an existing, nearby photon; the rate of this stimulated emission is proportional to the number of nearby photons. In the microcavity polariton laser, photons exist only as constituents of polaritons. Stimulated emission of a polariton requires the relaxation rate into a polariton state to be enhanced by the presence of polaritons already in that state. In this section we explore this concept of final state stimulation. Section 4.2 presents a rate equation analysis for a simple polariton boser. Section 4.3 extends this discussion to the experimentally realizable case of nonresonant excitation. The dynamics of microcavity polaritons have been studied by both continuous-wave and time-resolved photoluminescence spectroscopy. The results of these experiments are summarized in Section 4.3 and 4.4.

Bose Statistics

The indistinguishability of bosons results in their propensity to collect in a single quantum state. Here, we have adapted Feynman's discussion (Feynman,

1963) of scattering between bosons to the problem of polariton relaxation into a ground state. We first consider two polaritons – labeled (1) and (2) in Figure 4.1 – that are initially in different states, for example states of different momentum k and k' . Both polaritons relax into the same final state, 0. The probability of polariton (1) at k scattering into the state with momentum 0 is $|a_{k0}^{(1)}|^2$. The probability of polariton (2) at k' scattering into a state with momentum 0 is $|a_{k'0}^{(2)}|^2$. The complementary scattering events can also happen where polariton (1) is at k' ($|a_{k'0}^{(1)}|^2$) and polariton (2) is at k ($|a_{k0}^{(2)}|^2$). If the complementary relaxation pathways are distinguishable, then the probability of the two polaritons relaxing into the same ground state is $|a_{k0}^{(1)}a_{k'0}^{(2)}|^2 + |a_{k0}^{(2)}a_{k'0}^{(1)}|^2$. We can drop the labels since they have been assigned arbitrarily. The resulting probability for two distinguishable polaritons relaxing into the same ground state is $2|a_{k0}a_{k'0}|^2$. If the two polaritons are indistinguishable, then the probability of the two polaritons relaxing into the ground states is $|a_{k0}^{(1)}a_{k'0}^{(2)} + a_{k0}^{(2)}a_{k'0}^{(1)}|^2$ which is $4|a_{k0}a_{k'0}|^2$ when the labels are dropped. The indistinguishability of the two polaritons actually enhances their probability of relaxing into the same ground state. This is final state stimulation. If we, instead, have three polaritons with initial momenta k , k' , and k'' scattering into a single ground state, then there are six (3!) ways that these three polaritons can be distributed into the three initial states: $a_{k0}^{(1)}a_{k'0}^{(2)}a_{k''0}^{(3)}$, $a_{k0}^{(1)}a_{k'0}^{(3)}a_{k''0}^{(2)}$, $a_{k0}^{(2)}a_{k'0}^{(1)}a_{k''0}^{(3)}$, $a_{k0}^{(2)}a_{k'0}^{(3)}a_{k''0}^{(1)}$, $a_{k0}^{(3)}a_{k'0}^{(1)}a_{k''0}^{(2)}$, and $a_{k0}^{(3)}a_{k'0}^{(2)}a_{k''0}^{(1)}$. The probability of three *distinguishable* polaritons relaxing into the same ground state is $3!|a_{k0}^{(1)}a_{k'0}^{(2)}a_{k''0}^{(3)}|^2$. The probability of three *indistinguishable* polaritons relaxing into the same ground state is $|3!a_{k0}^{(1)}a_{k'0}^{(2)}a_{k''0}^{(3)}|^2$ – the indistinguishability of the polaritons enhances their relaxation probability by 3!. There are $n!$ ways that n

polaritons can be distributed into n initial states – an $n!$ enhancement in the relaxation rate. If we consider the particular case where n polaritons are already present, then adding one more polariton changes the relaxation rate enhancement from $n!$ to $(1+n)!$. The probability of an additional polariton relaxing into the ground state is enhanced by a factor of $1+n$.

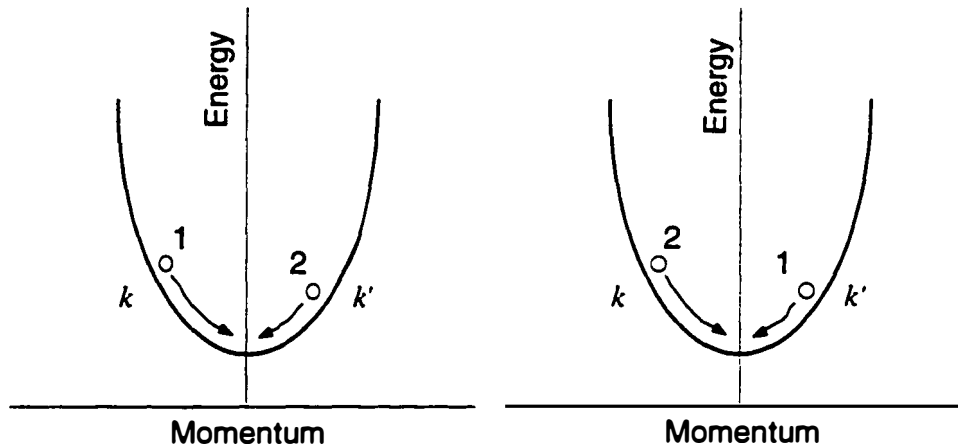


Fig. 4.1 The relaxation pathways for two polaritons with momenta k and k' that relax into the same ground state. These two pathways constructively interfere resulting in an enhancement in the relaxation rate known as final-state stimulation.

This same final state stimulation is responsible for stimulated photon emission. Photon stimulated emission occurs only because photons are bosons. If photons were fermions, the Pauli exclusion principle would prevent more than a single photon from occupying a cavity mode; build-up of the photon number in the laser cavity would effectively prevent any further relaxation of excited electrons. The probability of a fermion, such as an electron or hole, relaxing into a state with n fermions already present is $1-n$.

The average occupancy (n) of a quantum state must be close to one to see either final-state stimulation or Pauli exclusion. The temperature of these particles describes their distribution between different energy states. A high temperature implies that the probability of finding a particle at a specific energy is relatively small - the particles are spread over a large range of energy ($k_B T$). As the temperature decreases, the probability of occupying a specific, low energy state increases. The density of states describes the number of distinct states within a range of energies. A high temperature with a small density of states can translate into a large occupancy in each state. Likewise, a large density of states can prevent the occupancy of any given state from becoming large even at low temperatures. A useful measure of the density of states is the particle mass. Heavy mass particles have a large number of momentum states within a small energy range – the bands are relatively flat in E - k space. The thermal de Broglie wavelength describes the ratio of the density of states to the thermal energy spread (Lewenstein, 1994),

$$\Lambda_T = \sqrt{\frac{h^2}{3mk_B T}}, \quad (4.1)$$

and is a useful measure of the state occupancy. If the 2D particle density is smaller than Λ^{-2} then neither final state stimulation (for bosons) or Pauli exclusion (for fermions) is observable.

4.2 Resonant Polariton Laser

The microcavity polariton laser that we consider in this chapter uses final-state stimulation, as a laser uses photon stimulated emission, to ‘place’ polaritons

in a single quantum state. As a starting point, we consider the near-resonant generation of polaritons in the lower polariton branch. Figure 4.2 shows a schematic illustrating the relevant scattering processes in a polariton laser. Light from a pump laser generates excited polaritons. These polaritons relax by emitting acoustic phonons (lattice vibrations) to populate the $k=0$ lower polariton state (Tassone, 1996). It is this phonon emission rate into the polariton ground state that is enhanced by final-state stimulation.

$$\begin{aligned} \frac{dN_{l,o}}{dt} &= K_{ph} N_{l,k} (1 + N_{l,o}) (1 + \bar{N}_{ph}) - K_{ph} N_{l,o} (1 + N_{l,k}) \bar{N}_{ph} - \frac{N_{l,o}}{\tau} \\ &= K_{ph} (N_{l,k} - \bar{N}_{ph}) N_{l,o} - \frac{N_{l,o}}{\tau} + K_{ph} (1 + \bar{N}_{ph}) N_{l,k} \end{aligned} \quad (4.2)$$

where

$$K_{ph} (1 + \bar{N}_{ph}) = \sum_q |g_q|^2 (1 + N_{ph,q}) \delta(\omega_k - \omega_0 - c|q|) \quad (4.3)$$

for lower branch polaritons with center-of-mass momentum k and energy $\hbar\omega_k$. phonon modes q with phonon energy $\hbar c|q|$. g_q is the coupling constant of the polaritons to the phonon modes q . τ represents spontaneous annihilation of ground state polaritons. At exact resonance between the constituent cavity mode and exciton, the polariton lifetime is (Abram, 1996)

$$\frac{1}{\tau} = \frac{1}{\tau_p} + \frac{1}{\tau_{sp}}. \quad (4.4)$$

The first term in the (4.2) represents an exponential growth of the ground state polariton population (gain), the second term represents an exponential reduction of the ground state population (loss) and the last term is a linear increase in ground state population that is analogous to spontaneous emission. Similar models have neglected either the linear term or finite phonon occupancies

(Tikhodeev, 1990 and Yura, 1994); the inclusion of these effects has important implications for condensate formation in the polariton boser.

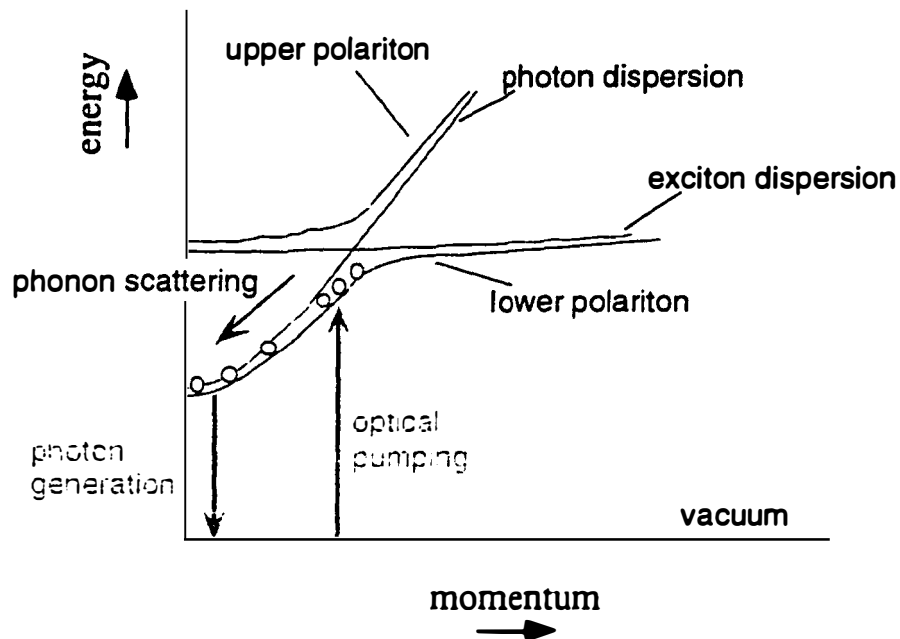


Fig. 4.2. Schematic of the energy flow in a 'resonant' polariton laser.

Polaritons with excess in-plane, center-of-mass momentum are generated by an optical pump beam. These polaritons relax by acoustic phonon emission into the polariton ground state. The ground state polaritons annihilate into photons

This polariton boser is analogous to an optical laser where the relevant electronic states are fermionic (electron/hole) instead of bosonic (polariton). Relaxation of electrons from the conduction band to the valence band in a conventional laser is described by

$$\begin{aligned}
\frac{dP_0}{dt} &= KN_0(1 - N_v)(1 + P_0) - KN_v(1 - N_c)P_0 - \frac{P_0}{\tau_p} \\
&= K(N_c - N_v)P_0 - \frac{P_0}{\tau_p} + KN_c(1 - N_v)
\end{aligned} \tag{4.5}$$

Comparison of Eq. (4.2) and (4.5) demonstrates the analogy between the polariton matter laser and a conventional semiconductor laser. The polariton ground state population is the analog of the photon number in an optical laser. Final-state stimulated relaxation of polaritons into the ground state is the analog of stimulated photon emission. Spontaneous annihilation of the ground state polaritons is analogous to photon loss from the optical resonator.

Equation (4.2) indicates an exponential growth in polariton number when $N_{l,k} > \bar{N}_{ph}$ – this is the inversion condition for the polariton laser. This inversion condition arises from the need for entropy to increase as energy is stored in the form of coherent polaritons. Non-resonant generation of polaritons increases both the energy and the entropy of the polariton system. In the limit of a high temperature optical source, the entropy produced by the optical pumping is $\Delta S = \hbar\omega_{pump}/T_{pump} = k_B/N_{l,k}$. The relaxation of the high-momentum polaritons to the ground state reduces the entropy by $\Delta S = \hbar\omega_{ph}/T_{ph} = k_B/\bar{N}_{ph}$. Thermodynamic inversion occurs when all of the entropy added to the system by pumping is removed by phonons $N_{l,k} = \bar{N}_{ph}$. At pump levels higher than inversion, coherent energy can be extracted from the pump reservoir. We see that the polariton laser, like the optical laser, is essentially a heat engine that does work by virtue of heat exchange between the optical pump and the phonon reservoirs.

As is the case with a conventional laser, inversion is not sufficient for the generation of a coherent state in the polariton laser. As we saw in Chapter 3, a well-defined laser threshold must be accompanied by an abrupt change in the differential efficiency as the pump increases above threshold. A small below threshold differential efficiency requires competing dissipation channels (K_{loss}). These competing loss channels ensure that the pump is depleted immediately above threshold and that there is a well defined discontinuity in the rate of condensate formation above and below threshold. This condition is equivalent to the requirement for a small spontaneous emission factor to observe threshold in a conventional semiconductor laser. The effective β for the polariton laser is simply $\beta = K_{ph}/K_{loss}$. The dominant loss term for the resonant polariton laser is loss of high-momentum polaritons due to spontaneous recombination of the constituent excitons or from the escape of constituent photons out of the microcavity. Figure 4.3 shows the polariton number in the ground state versus the pump rate of excited polaritons for various β .

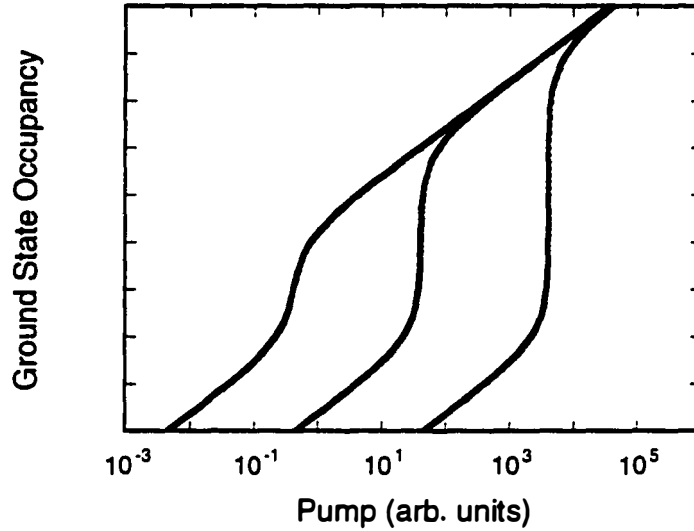


Fig. 4.3. The number of ground state polaritons versus the number of optically generated polaritons for various β .

In this limit of the polariton laser system, an ordered state is realized when annihilation of polaritons from the ground state (loss) is completely balanced by final state stimulated relaxation into the ground state (gain) –

$$K_{ph}(N_{l,k} - \bar{N}_{ph}) = \frac{1}{\tau}. \quad (4.6)$$

As with the conventional laser, this ‘gain equals loss’ threshold condition strictly applies only as $\beta \rightarrow 0$. In the polariton laser with a finite β , the net gain asymptotically approaches the total loss. Equation (4.6) overestimates the excited polariton number at the measured threshold.

4.3 Non-resonant Polariton Laser

Now that we have established the inversion and threshold condition for the simple case where only polaritons in the low energy branch are excited, we can consider the experimentally relevant case of nonresonant pumping. Experimentally we will be exciting polaritons with a short 150 fs laser pulse. A short optical pulse allows us to obtain time-resolved spectra and avoids the problem of heating associated with intense continuous-wave pumping. The broad spectral width of such a short pulse means that both polaritons and free electron-hole pairs are generated for resonant pumping; the spectral width is as large as the exciton binding energy 10 meV. In order to eliminate the uncertainty in the type of carrier generated, the pump light is tuned to the electron-hole resonance. This ensures that the pump primarily excites free electron-hole pairs.

Polariton Dynamics

Figure 4.4 illustrates the energy flow through a nonresonantly pumped polariton laser. The light from the pump laser generates free electron and holes in a quantum well. These electron-hole pairs subsequently form excitons with large center-of-mass momenta. There are three distinct regions of momentum space over which exciton/polariton states are distributed (Figure 4.4). Exciton states are distributed across the Brillouin zone from $-\pi/a$ to $+\pi/a$, where a is the crystal lattice constant. When the constituent exciton's in-plane, center-of-mass momentum k is larger than the total photon momentum,

$$k > \frac{2\pi n}{\lambda_{opt}}, \quad (4.7)$$

a photon cannot carry away the exciton's momentum. These excitons do not recombine and radiate light. Since the optical wavelength is typically 500 times larger than the lattice constant only a small fraction of the exciton states – near the zone center – couple to light. The initially excited excitons lose their energy to the crystal lattice as phonons (or lattice vibrations). When the exciton momentum is sufficiently small, where Eq.(4.7) is satisfied, they also lose energy by radiating light. Of these few exciton states that radiate, only about ten percent are able to form polaritons. The remaining excitons spontaneously emit light into the passband of the DBR microcavity (Tassone, 1996). The excitons cool towards the zone center and eventually into the two polariton branches. These excited polaritons relax into the polariton ground state ($k=0$) by acoustic phonon emission. The entire process from free electron-hole generation to relaxation into the polariton ground state requires the dissipation of approximately 12 meV into the crystal lattice; more than one hundred individual acoustic phonon emission events.

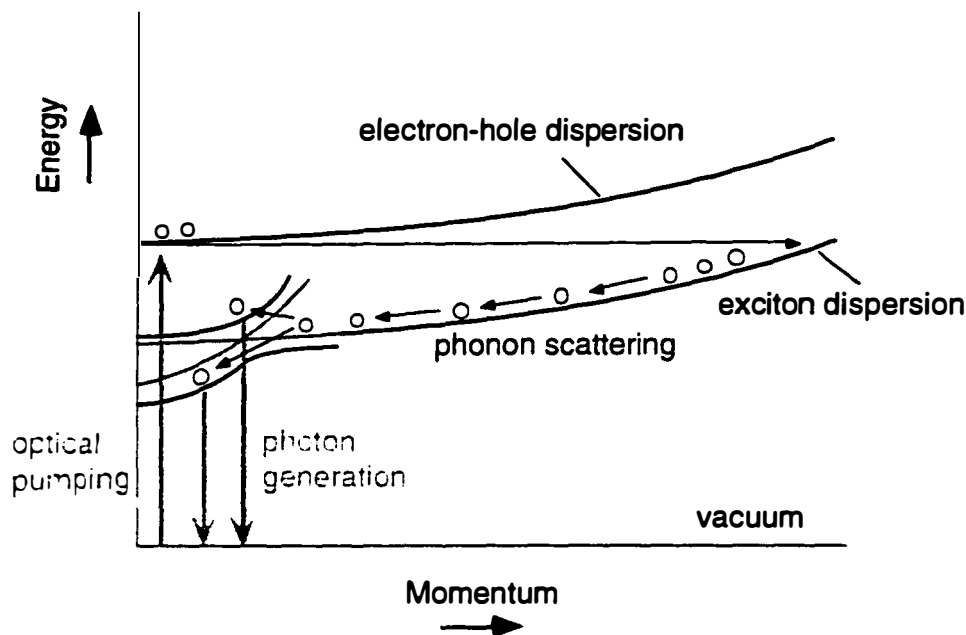


Fig. 4.4 Schematic of the energy flow in a nonresonant polariton laser: (a) free electron-hole pairs are generated by an optical pump beam, (b) the free carriers elastically scatter and form excitons with excess in-plane, center-of-mass momentum, (c) the excitons relax by acoustic phonon emission to (d) eventually populate both polariton branches, and (e) the polaritons annihilate into photons.

Photoluminescence Spectroscopy

In Chapter 2, a system of microcavity polaritons was characterized by continuous-wave spectroscopy and reflection measurements (Goobar, 1996). This sample, grown using molecular beam epitaxy by Jack Ko at UCSB, is also used for the polariton laser experiments discussed below. A scanning electron micrograph of the grown wafer is shown in Figure 4.5. The cavity consists of a top mirror with 15 $\text{Al}_{0.11}\text{Ga}_{0.89}\text{As}/\text{AlAs}$ periods, a $\text{Al}_{0.3}\text{Ga}_{0.7}\text{As}$ cavity of thickness $L_c = \lambda$ and a bottom mirror with 20.5 $\text{Al}_{0.11}\text{Ga}_{0.89}\text{As}/\text{AlAs}$ periods. A single GaAs quantum well (QW) of thickness $L_{\text{QW}} = 150 \text{ \AA}$ is placed at the center

of the cavity which has its resonance aligned to the heavy-hole exciton absorption line at around 10 K. The polariton splitting at minimum detuning between the cavity resonance and exciton transition is 3.7 meV.

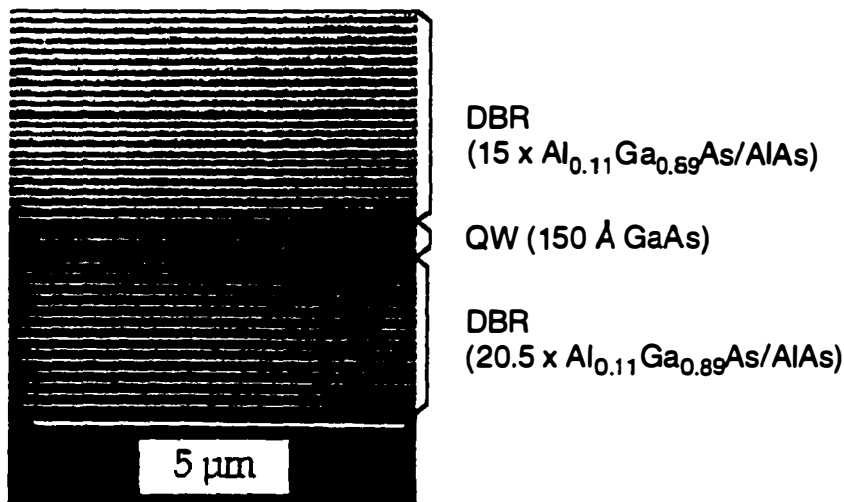


Fig. 4.5 A SEM micrograph of a microcavity sample with a one wavelength optical resonator and high reflectivity distributed Bragg reflectors. The quantum well and cavity are designed for optimal exciton-photon coupling at 10 K.

The microcavity sample was mounted on the cold-finger of an Oxford model CF1104 liquid He flow cryostat (Fig. 4.6). The excitation pulses were generated by a Coherent Mira mode-locked $\text{Ti}:\text{Al}_2\text{O}_3$ laser, with a pulsewidth of 150 fs and a repetition rate of 82 MHz. A continuously variable neutral density filter was used to vary pump power without affecting pulsewidth. The excitation pulses were focused onto the microcavity sample at an incident angle of $\sim 10^\circ$ and an approximate spot size of $100\mu\text{m}$. The photoluminescence was collimated and sent through a SPEX 0.5 meter, single grating spectrometer. For time-integrated

measurements, this spectrally filtered light was collected by a Hamamatsu GaAs photomultiplier tube.

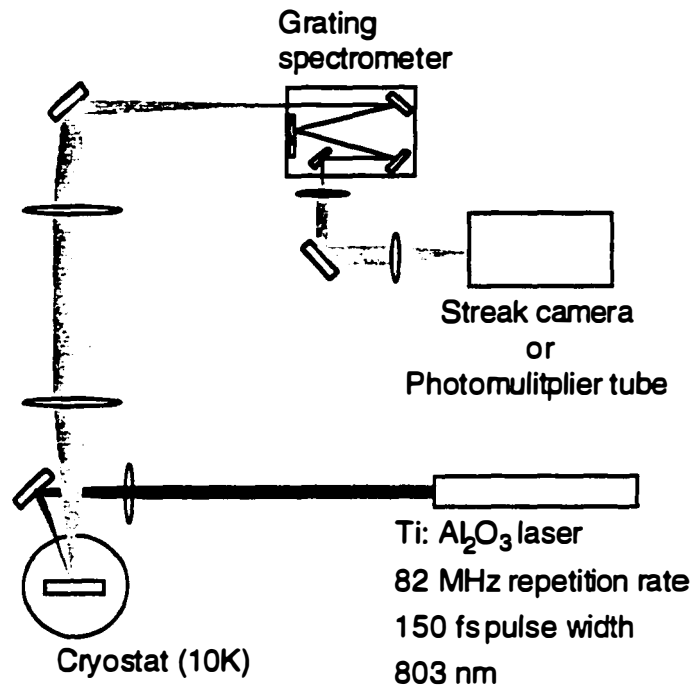


Fig. 4.6 The measurement set-up for time-integrated and time-resolved spectroscopy of polaritons. The sample is pumped with a mode-locked Ti:Al₂O₃ laser and the photoluminescence is collected either by a GaAs photomultiplier or a streak camera.

A typical photoluminescence spectrum for a time-averaged pump power of 30 mW is shown in Figure 4.7. Luminescence from both polariton branches is clearly resolved. The same polariton splitting is observed for these time-integrated measurements as for the continuous-wave pump measurements of Chapter 2. Since the pump pulse is filtered by the microcavity which surrounds the quantum well, the density of excited carriers cannot be directly estimated. We cannot estimate the fraction of the pump absorbed at the quantum well since

neither the reflected pulse nor the transmitted pump pulse can be monitored. In order to estimate the carrier density, we analyze the shift of the polariton transition with incident power and use a many-body model to estimate the exciton density required to generate such a shift. This technique is presented in detail in Section 4.4. The polaritons are not equally distributed between the two branches. The low energy branch is more heavily populated. The relative luminescence intensities can be modeled by a Boltzman distribution (Stanley, 1996). The assumption of thermal equilibrium between the two polariton branches seems plausible given the number of phonon scattering events required for the generated free electron-hole pairs to relax into the polariton states.

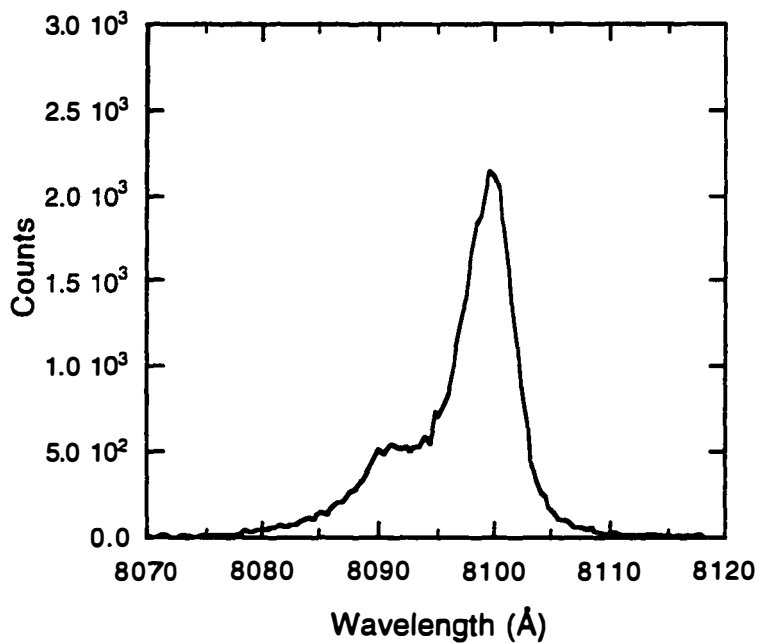
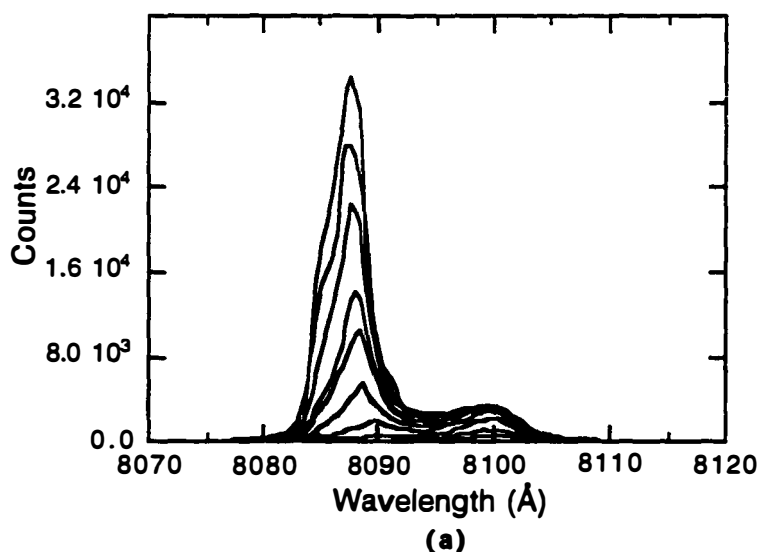


Fig. 4.7 Photoluminescence spectrum at a time-integrated pump power of 30 mW.

As the pump power increases, the relative photoluminescence intensities can no longer be described by an equilibrium Boltzman distribution. The distribution of polaritons between the two branches exhibits a strong dependence on the pump intensity. Figure 4.8a show the time-integrated photoluminescence spectra as a function of pump power. Beyond a pump level of 40 mW, the luminescence from the lower polariton clamps whereas the luminescence from the upper polariton increases rapidly. A distinct laser-like threshold for the upper polariton is visible. Clearly, the polariton distribution between these two branches is not described by a Boltzman distribution. Figure 4.8b shows the peak intensity versus pump power for the polariton transitions. The rapid increase in the slope efficiency of the upper polariton is suggestive of some sort of laser action.



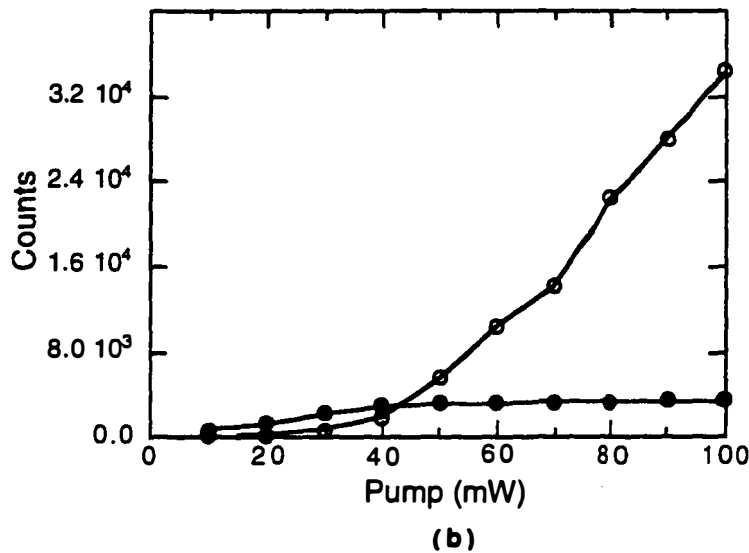


Fig. 4.8 (a) Photoluminescence spectra at various optical pump powers. (b) Peak photoluminescence intensity in the upper (open circles) and lower (closed circles) polariton branches.

Time-resolved measurements were made by collecting the output of the spectrometer with a Hamamatsu streak camera. The streak camera was triggered by a slow detector within the Mira laser. Triggering the streak camera with the excitation pulse eliminated the effects of long-time jitter inherent to the Mira. The temporal resolution of these measurements was limited by chirp introduced by the spectrometer and by residual jitter in the mode-locked laser. The resolution was estimated by sampling the 150 fs excitation pulse with the streak camera – the measured resolution was 60 ps.

Figure 4.9 shows the time-resolved photoluminescence for the upper polariton line and an exponential fit at a time-averaged pump power of 30 mW. The time-dependence of the luminescence can be approximated as a single decaying

exponential – this single exponential describes the data over two decades of intensity. The extracted decay time is 170 ps. The peak of the luminescence occurs approximately 300 ps after the excitation pulses. Both the long rise- and decay-time reflect the large number of acoustic phonon emission events required to relax the excited excitons into the polariton states. The measured times are in agreement with previously published relaxation times for bare excitons (Eccleston, 1991).

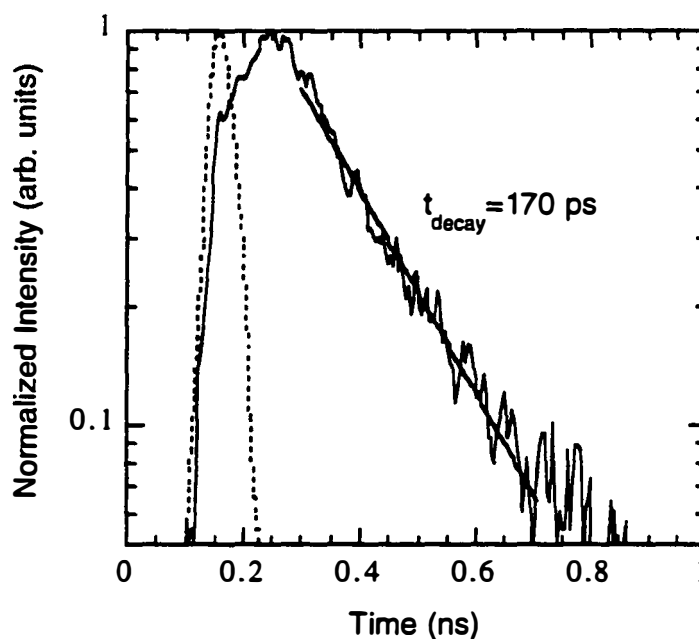


Fig. 4.9 Time-resolved photoluminescence intensity versus time for the upper polariton branch at an optical pump power of 30 mW.

The time-resolved measurements indicate an increase in the decay rate that is coincident with the change in the measured slope efficiency. Figure 4.10 shows

the time-resolved photoluminescence from the upper polariton versus pump power. The decay rate increases when the pump power is greater than 40 mW – this is the threshold pump power observed in Figure 4.8 . Figure 4.11 shows the luminescence intensity versus time for a pump power of 60mW. The luminescence decay can no longer be described by a single exponential. The decay rate is observed to decrease as the intensity decreases, i.e. as the polariton density decreases. The fast initial decay is approximately 95ps and the slow decay is approximately 165ps. At long times, the relaxation rate returns to the value below threshold. The data clearly describe an enhanced relaxation rate as the polariton density increases. Both the observed threshold behavior and the enhanced relaxation rate are consistent with the polariton laser described in this chapter.

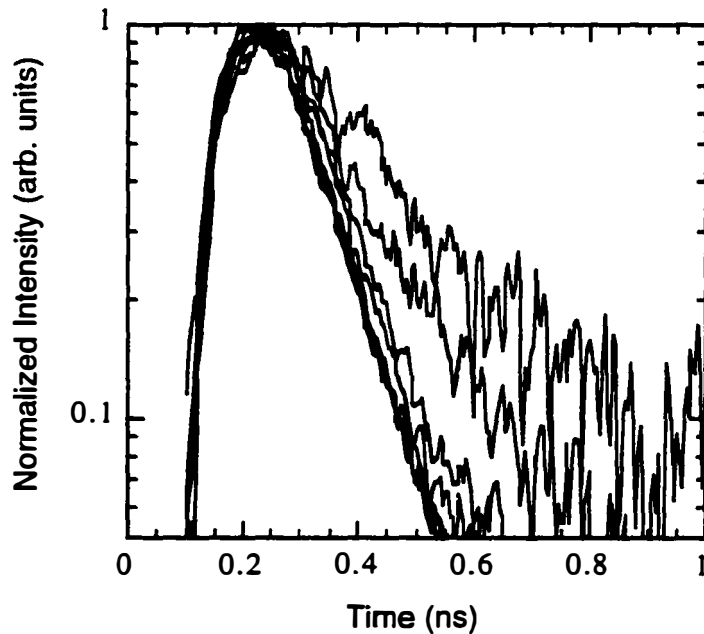


Fig. 4.10 Time-resolved photoluminescence at various optical pump powers from the upper polariton.

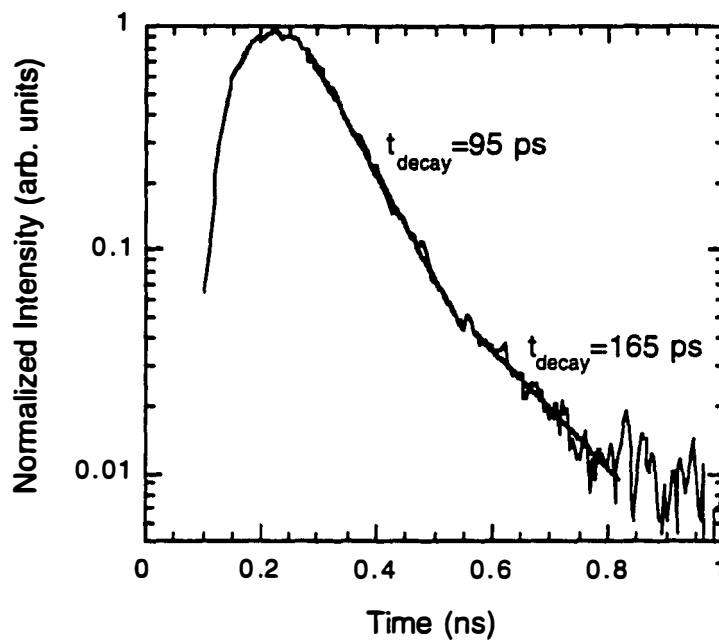


Fig. 4.11 Time-resolved photoluminescence intensity versus time for the upper polariton branch at an optical pump power of 60 mW.

The luminescence from the lower polariton branch, however, exhibits no dependence on the pump power. From Figure 4.12, we see that the time dependence of the luminescence is completely independent of the polariton density. The luminescence decay cannot be described by a single exponential. The decay rate appears to increase with time independent of the polariton density. There is no evidence for any sort of final state stimulation for this polariton branch.

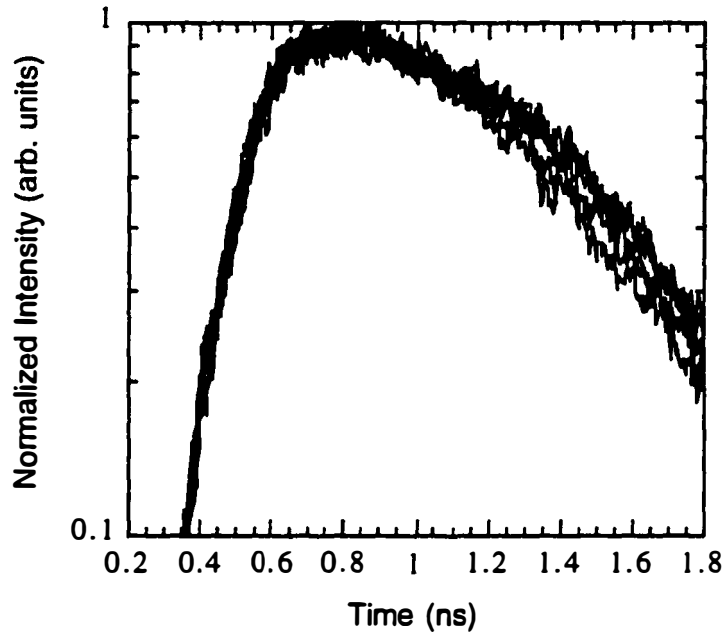


Fig. 4.12 Time-resolved photoluminescence at various optical pump powers from the lower polariton.

4.4 High-Density Polaritons

While final-state stimulation of polaritons is the hoped for explanation for the observed threshold there are several causes for concern. The shift in the energy of the luminescence peaks with pump power is an indication that the density of polaritons is high. A high particle density can frustrate final-state stimulated relaxation of polaritons. Polaritons consist of photons, electrons and holes, where the latter two are bound together as excitons. At high polariton densities, the constituent electrons and holes in neighboring polaritons interact with each other. Pauli exclusion between neighboring electrons and holes limits the growth of the

polariton density. The constituent exciton density saturates at approximately (Schmitt-Rink, 1985)

$$n_{sat} = \frac{1}{4\pi a_B^2}, \quad (4.8)$$

where a_B is the bare exciton Bohr radius. This interaction between constituent fermions effectively saturates the 'gain' in the polariton laser. This process is similar to spatial holeburning where the growth in the photon number saturates the net optical gain.

The saturation of exciton density also reduces the interaction between the constituent excitons and photons. The coherent absorption and reemission of photons that is responsible for polariton formation cannot occur if the exciton states saturate or become 'full.' The polariton splitting decreases as the polariton density increases (Houdre, 1995)

$$\Omega = \frac{\Omega_{n=0}}{\sqrt{1 + n/n_{sat}}}. \quad (4.9)$$

Figure 4.13 shows the peak of the polariton luminescence versus position for two pump powers – the cavity resonance varies with the position as described in Chapter 2. There is a dramatic reduction in the splitting observed at a time-averaged pump power of 2.7 mW and 50 mW; the measured splittings are 3.8 meV and 0.7 meV, respectively. Using Equation (4.9) and the measured splittings gives an estimated polariton/exciton density of $n \approx 30 n_{sat}$ at 50 mW. At this density there is significant overlap between neighboring excitons. Since the measured splitting is the same size as the measured luminescence linewidth the polariton picture is no longer valid. Recent measurements by H. Wang, *et al.* have recently confirmed the observed collapse of the polariton line that is

coincident with 'lasing' (Wang, 1996). These measurements monitored the reflectivity of a probe pulse that had a variable delay relative to the pump pulse. At densities corresponding to 'lasing' the avoided crossing was no longer observable by probe reflection. Both measurements indicate that polaritons do not survive at the observed threshold densities.

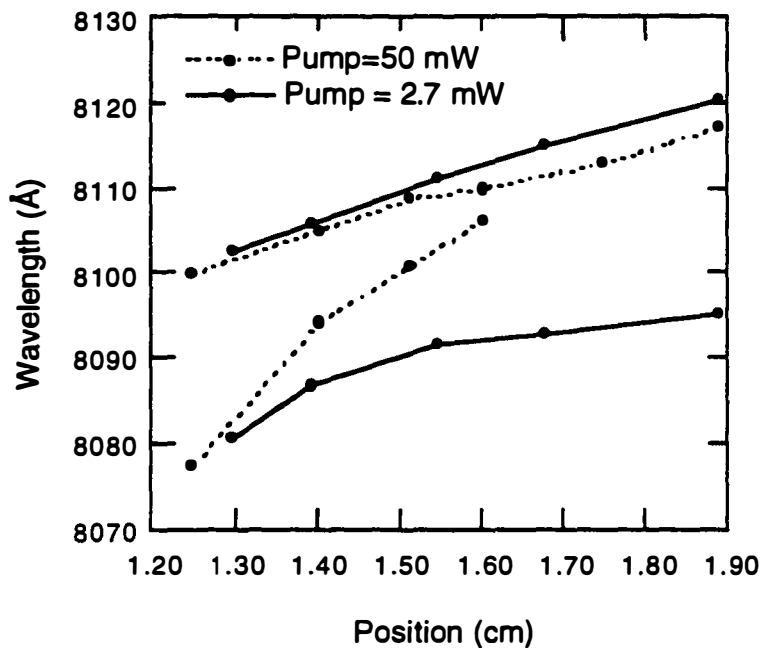


Fig. 4.13 The peak photoluminescence intensity from the upper and lower polariton branches at various positions on the wafer.

At high densities, the dynamics of polaritons and excitons is not well understood. Equation (4.9) is not valid at densities as high as $n \approx 30 n_{sar}$. This is, however, our best tool for establishing an approximate exciton density. Equation (4.9) does not incorporate bandgap renormalization which occurs as the carrier

density increases. The free electron-hole levels change as the large carrier populations screen the crystal lattice potential. Since the excitons are neutral particles their energy levels are not strongly effected by the increase in total carrier density. This screening leads to a reduction in the bandgap that is referred to as bandgap renormalization (Haug, 1994). When the bandgap has narrowed by the exciton binding energy, the exciton energies and the free electron-hole energies are equal. At this point, no energy is required to ionize an exciton. The resulting carrier population consists only of free electron-hole pairs. These free electron-hole pairs are able provide optical gain and can supply energy for a conventional optical laser. Future work on the polariton laser system must explore this transition from the polariton laser to the optical laser that occurs at high density. As of yet, the existence of such a transition in the experiments presented above is indeterminate.

4.5 Summary

In this chapter, we have extended the conventional theory of lasers to massive bosons. In a conventional laser, stimulated light emission establishes a coherent photon population in the optical cavity. These coherent photons leak out of the cavity and appear as propagating light. This light maintains the coherence and spectral purity of the intracavity photons. In the polariton laser or boaser, the coherence is established within a population of massive polaritons. These cavity polaritons eventually annihilate and emit a photon which propagates outside the cavity. Again, the emitted light maintains the coherence properties of the intracavity polaritons. The inversion and threshold conditions for the polariton

laser are in direct analogy with the optical laser. A similar output behavior is predicted for the polariton laser and the conventional optical laser.

Experimentally, the system of microcavity polaritons exhibits a threshold that is consistent with the theory of the polariton laser. Unfortunately, the densities required to achieve threshold in this laser system make the interpretation of the experimental data difficult. The most important difference between photons and massive polaritons is that photons are nearly ideal bosons and polaritons are constituent bosons constructed from fermions. The interactions of the constituent fermions in massive bosons limits the build-up of large populations. In the experiments, the loss rate (5ps) most likely was so high that the weak acoustic phonon relaxation processes could not maintain large steady-state populations in the ground state. As a result, the threshold population density was sufficiently large that the constituent electron-hole interactions drastically altered the polariton system. Not only did the polariton branches collapse, but the constituent excitons may have ionized. In this limit, conventional photon stimulated emission could be responsible for the observed threshold. This interpretation is not entirely consistent with the observation of two emission lines, but the dynamics of excitons/polaritons at these high densities has still to be explored in detail.

The interactions between the constituent fermions inside the polariton can frustrate final state stimulation. Photons are intrinsically robust bosons. They are able to survive collisions with other particles remarkably well. In addition, the typically weak interactions between photons allows the build-up of very large photon numbers. While the underlying interactions – final state stimulation resulting from the indistinguishability of bosons – provides gain for both the boson

and the laser, it is the photon's robust nature that allows a laser to be realized so easily.

•

Chapter 5

COHERENT MATTER AND LIGHT

5.1 Summary

We have attempted to improve the efficiency of semiconductor lasers by reducing the number of radiative pathways for spontaneous emission. The total spontaneous emission rate decreases as the number of accessible modes decreases. The removal of all but the single lasing mode from the optical cavity eliminates a significant fraction of the energy wasted in a conventional semiconductor laser. Microcavity lasers offer the benefits of lower threshold currents and higher below-threshold efficiencies. In Chapter 2, we discussed serious limitations to our ability to reduce the spontaneous emission rate for free electron-hole pairs. Electron-hole pairs typically radiated in all directions. A semiconductor microcavity constructed with DBRs only provides optical confinement for a few degrees so that the electron-hole recombination rate is only weakly altered by the cavity. The weak optical confinement arises from both the large penetration depth - which makes the cavity seem large - and the passband emission. We need to engineer a system where the deficiencies of the DBR resonator can be mitigated. The two approaches that we have considered are: (1) to use a narrow post resonator which would provide transverse optical

confinement and thereby confine the spontaneous emission to a small angular spectrum and (2) to inhibit scattering between neighboring momentum states, which couple to light in different directions, by using a strong-coupling induced energy shift.

Chapter 3 investigated the benefits of true single mode lasers and explored the limitations to achieving such lasers with free electron-hole pairs in small diameter optical cavities. A cavity with a small etched-post resonator was used to provide strong transverse confinement. The small transverse cavity alleviates the problems associated with a large DBR penetration depth and passband emission but introduces optical scattering losses and carrier diffusion. Increased optical losses require larger threshold carrier densities. These high density electrons are distributed over a large range of kinetic energies and subsequently radiate a broader spontaneous emission spectra. The broad frequency distribution of the participating electronic transitions makes the demands on the optical cavity even more severe. In addition, carrier diffusion (or surface recombination) of excited electrons out of the narrow post resonator nullifies the advantages of a high β structure; increasing the fraction of electrons emitting photons in the desired optical modes cannot result in high efficiencies if we are unable to efficiently deliver excited electrons to the active region. Engineering the optical resonator offers only limited control of the spontaneous emission processes of the electron-hole pairs.

Additional control can be realized by exploiting strong-coupling induced energy shifts. The coupling of a dipole oscillator to an optical mode shifts the resonant energy of the dipole oscillator. The magnitude of the shift is

proportional to the coupling strength between the dipole and the cavity mode. This energy shift is a function of the detuning between the bare dipole and cavity resonances. Since the transition energy is dependent on the carrier momentum, neighboring momentum states experience different strong-coupling energy shifts. For sufficiently large dipole-cavity coupling it is possible to isolate neighboring momentum states. Suppression of scattering between neighboring momentum states effectively prevents carriers from probing the microcavity response at different angles. These 'isolated' carriers see only the high reflectivities associated with reflection at resonance from the DBR. Such 'momentum space engineering' is effective only when the coupling induced energy shift is sufficiently strong. This is the case for excitons where the large electron-hole overlap – due to Coulomb interactions – increases their coupling strength to the electromagnetic field. The coupling is large enough to stabilize the polariton states that are the 'true' eigenenergy states for the dipole-cavity (exciton/photon) system. In Chapter 2 we saw that indeed single mode coupling could be realized.

Single mode operation without stimulated emission therefore requires the 'momentum space engineering' embodied by polaritons. Unfortunately, the bosonic nature of the excitons and polaritons does not allow for conventional optical gain. A system of ideal bosons cannot be used to provide gain in a conventional optical laser. In Chapter 4, we proposed a polariton boser which is a device that generates coherent light by first generating coherence in massive polaritons. The theoretical analysis shows that the polariton boser is not the high efficiency source for which we are looking. The effective β in a nonresonantly pumped polariton boser can be very low, so that thresholdless lasing behavior is

not realized in the boson. Energy in the boson is wasted because of spontaneous annihilation of excitons and polaritons in high momentum states. Even though single mode emission is realized, the polariton boson and the microcavity laser still face serious challenges on the road to realizing truly high efficiency and low threshold.

5.2 The Future Development of the Boson

The polariton boson and the microcavity laser both generate coherent light by analogous processes in similar structures. The similarity makes differentiating between laser and boson action nontrivial. This is the issue that future research must address. In the experiments presented here, the problem has been that the threshold density is too high for us to have a system of noninteracting bosons. At sufficiently high densities final-state stimulation saturates and the constituent excitons ionize into free electron-hole pairs. The two directions for future research are to characterize the boson-laser transition in detail and to lower the necessary threshold density for a polariton boson.

Laser to Boson Transition

Polaritons are composite bosons constructed from superpositions of electron, hole and photon states. At low density, the polaritons can be treated as weakly interacting bosons. As such, they are expected to exhibit final-state stimulated relaxation that provides the 'gain' for the polariton laser. Since polaritons are composite particles, their treatment as bosons is always approximate. The constituent electrons and hole interactions cannot be neglected at high polariton

density. In the experiments presented in Chapter 4, an approximate density was calculated from the measured shift in the time-integrated luminescence peaks with the pump power. A more accurate implementation of this technique would be to monitor the movement of the polariton peaks as the luminescence intensity decays. We expect to see a recovery of the polariton avoided crossing as the exciton density decreases. Such a time-resolved measurement would allow us to continuously monitor the particle density and to carefully examine the transition from polariton to exciton and possibly to electron-hole luminescence. After our experimental results, several groups have indeed begun preliminary investigation of such time-resolved PL spectra. Recently, H. Wang has performed pump-probe spectroscopy of a similar microcavity sample and confirmed the collapse in polariton splitting at threshold that we observe (Wang, 1996).

In addition to carefully monitoring the exciton/polariton density, we can monitor the total free carrier density by performing pump-probe spectroscopy on the free electron-hole bandedge absorption. Monitoring the energy of the bandedge absorption would enable us measure the bandgap renormalization and hence the free carrier density. This would allow a direct confirmation that the threshold density in the polariton bozer is below the Mott density. If this is the case, the gain mechanism is not expected to be photon stimulated emission (conventional gain) since there is no population inversion below the Mott density (Imamoglu, 1996).

Reducing Polariton Laser Threshold

While accurate determination of the particle density is necessary, our preliminary estimates have indicated that the threshold polariton density for boson threshold is high. The threshold density can be lowered by reducing the loss rate of polaritons from the condensate state and by increasing the effective β of the polariton boson.

The polariton loss rate is the mean of the constituent exciton spontaneous emission rate and the photon lifetime in the microcavity. The short cavity lengths in microcavity structures result in a short time between successive mirror bounces and a subsequently short photon lifetime. The estimated photon lifetime in our microcavity structure is approximately 5ps, whereas the exciton lifetime is 20ps. Increasing the mirror reflectivity and the photon lifetime can reduce the threshold density by almost a factor of four. The easiest way to increase the mirror reflectivity is to increase the refractive index discontinuity between successive layers within the DBRs. A simple way to achieve this is by selective thermal oxidation of the AlAs layers. The resulting oxide is a nearly lossless dielectric with a refractive index of approximately $n=1.5$ compared to an AlAs refractive index of $n=2.98$.

In addition to reducing the condensate loss rate, we can improve the efficiency at which we are supplying excitons/polaritons to the condensate. Large effective β s in the polariton boson can be realized using near-resonant instead of nonresonant pumping. Near resonant pumping eliminates the long journey the carriers must make on their way from the free electron-hole pairs to ground state polaritons. Since a large fraction of the generated carriers are lost either by

exciton emission into the passband or by polariton emission into various directions, the total density of carriers generated by optical pumping is much larger than that needed to support a coherent polariton condensate. Resonant pumping of polaritons requires picosecond, not femtosecond, mode-locked lasers. These lasers have a sufficiently narrow spectral width so as to excite polaritons in only one branch; no free electron-hole pairs or excitons are generated. This increased β will lower the threshold pump power and help us reach the eventual goal of high efficiency, coherent optical sources.

5.3 Lasers are Bosers

The polariton boser that we have proposed is, in many ways, a generalization of the optical laser. Fundamentally a laser relies on the nonequilibrium condensation of photons into a single optical mode. The indistinguishability of photons is solely responsible for stimulated emission. This is true for all bosons. The essential difference between photons and other bosons is that massive bosons directly interact with each other. This makes maintaining coherent populations at sufficiently high densities very difficult. Optical coherence is a great deal more robust. Since photons do not directly interact with one another they are able to collect in large numbers even when the wavelength of light is small compared to the confining volume. While the boser and laser both rely on the same underlying physics the laser was realized first since photons are a clean, nearly ideal Bose particle.

References

- Abram, I., B. Sermage, S. Long, J. Bloch, R. Planel, and V. Thierry-Mieg, "Spontaneous emission dynamics in planar semiconductor microcavities," J. Rarity and C. Weisbuch, ed., *Microcavities and Photonic Bandgaps: Physics and Applications*. Dordrecht: Kluwer Academic Publishers (1996).
- Andreani, L. C., "Radiative lifetimes of free excitons in quantum wells," *Solid State Communications*, vol. 77, no. 9, pp. 641-645 (1991)
- Andreani, L.C., A. Pasquarello, "Accurate theory of excitons in GaAs-Ga_{1-x}Al_xAs quantum wells," *Phys. Rev. B*, vol.42, no.14, pp. 8928-38 (1990).
- Baba, T. T. Hamano, F. Koyama, K. Iga, "Spontaneous emission factor of a microcavity DBR surface emitting laser," *IEEE J. Quantum Electron.*, vol. 27, no. 6, pp. 1347-1358 (1991).
- Babic, D. I., Y. Chung, N. Dagli, J. E. Bowers, "Modal reflection of quarter-wave mirrors in vertical cavity lasers," *IEEE J. Quantum Electron.*, vol. 29, no. 6, pp. 1950-1962 (1993).
- Balanis, C. A., *Antenna theory: Analysis and Design*. New York: John Wiley & Sons (1982).
- Bjork, G. and Y. Yamamoto, "Analysis of semiconductor microcavity lasers using rate equations," *IEEE J. Quantum Electron.*, vol. 27, no. 11, pp. 2386-2396 (1991)
- Bjork, G. Y. Yamamoto, S. Machida, K. Igeta, "Modification of spontaneous emission rate in planar dielectric microcavity structures," *Phys. Rev. A*, vol. 44, no. 1, pp. 669-681 (1991).
- Bjork, G., H. Heitmann, and Y. Yamamoto, "Spontaneous emission coupling factor and mode characteristics of planar dielectric microcavity lasers," *Phys. Rev. A*, vol. 47, no. 5, pp. 4451-4463 (1993).

- Butov, L.V., A. Zrenner, G. Abstreiter, G. Bohm, and G. Weiman, "Condensation of indirect excitons in coupled AlAs/GaAs quantum wells," *Phys. Rev. Lett.*, vol. 73, pp. 304-307 (1994).
- Choquette, K.D., W. W. Chow, M. H. Crawford, K. M. Geib, and R. P. Schneider, Jr, "Threshold investigation of oxide-confined vertical-cavity laser diodes," *Appl. Phys. Lett.*, vol. 68, no. 26, pp. 3689-91 (1996).
- Coldren, L. A. and S. W. Corzine, *Diode Lasers and Photonic Integrated Circuits*, New York: John Wiley & Sons, Inc. (1995).
- Corzine, S. W., R. H. Yan, and L. A. Coldren, "Theoretical gain in strained InGaAs/AlGaAs quantum well lasers including valence-band mixing effects," *Appl. Phys. Lett.*, vol. 57, no. 26, pp. 2835-2837 (1990).
- Damen, T.C., J. Shah, D. Y. Oberli, D. S. Chemla, J. E. Cunningham, and J. M. Kuo, "Dynamics of exciton formation and relaxation in GaAs quantum wells," *Phys. Rev. B*, vol. 42, pp. 7434-7438 (1990).
- Deppe, D. G. and C. Lei, "Spontaneous emission from a dipole in a semiconductor microcavity," *J. of Appl. Phys.*, vol. 70, no. 7, pp. 3443-3448 (1992).
- DiGiorgio, V. and M. O. Scully, "Analogy between laser threshold region and second-order phase transition," *Phys. Rev. A*, vol. 2, pp. 1170-7 (1970).
- Drexhage, K. H., "Interaction of light with monomolecular dye layers," E. Wolfe, ed., *Progress in Optics vol XII*. New York: North Holland (1974).
- Eccleston, E., R. Strobel, W. W. Ruhle, J. Kuhl, B. F. Feuerbacher, K. Ploog, "Exciton dynamics in a GaAs quantum well," *Phys. Rev. B*, vol. 44, no. 3, pp. 1395-8 (1991).
- Feynman, R. P., R. B. Leighton, and M. Sands, *The Feynman Lectures on Physics: Volume 3*. Reading, Massachusetts: Addison-Wesley (1963).
- Fisher, T.A.; A. M. Afshar, D. M. Whittaker, M. S. Skolnick, J. S. Roberts, G. Hill, and M. A. Pate, "Electric-field and temperature tuning of exciton-photon coupling in quantum microcavity structures," *Phys. Rev. B*, vol.51, no.4, pp. 2600-3 (1995)
- French, A. P. and E. F. Taylor, *An Introduction to Quantum Physics*. New York: W. W. Norton Company (1978).
- Goobar, E., M. G. Peters, G. Fish, and L. A. Coldren, "Highly efficient vertical cavity surface-emitting lasers optimized for low temperature operation," *IEEE Photonics Technol. Lett.*, vol. 7, no. 8, pp. 851-853 (1995).

- Goobar, E., R. J. Ram, J. Ko, G. Bjork, M. Oestreich, and A. Imamoglu, "Vacuum fieldinduced mixing of light and heavy hole excitons in a semiconductor microcavity," *Appl. Phys. Lett.*, vol. 69, no. 23, pp. 3465-7 (1996).
- Griffin, A. D. W. Snoke, S. Stringari, eds., *Bose-Einstein Condensation*. New York: Cambridge University Press (1995).
- Hanamura, E., H. Haug, "Condensation effects of excitons," *Phys. Rep.*, vol. 33, no. 4, pp. 209-284 (1976)
- Haroche, S., "Cavity quantum electrodynamics," J. Dalibard, J.-M. Raimond and J. Zinn-Justin, ed., *Fundamental Systems in Quantum Optics*. Amsterdam: North Holland (1992).
- Haug, H. and S. Koch, *Quantum theory of the optical and electronic properties of semiconductor*, 3rd ed. Singapore: World Scientific (1994).
- Houdre, R., J. L. Gibernon, P. Pellandini, R. P. Stanley, U. Oesterle, C. Weisbuch, J. O'Gorman, B. Roycroft, and M. Illegems, "Saturation of the strong-coupling regime in a semiconductor microcavity: free-carrier bleaching of cavity polaritons," *Phys. Rev. B*, vol.52, no.11, pp. 7810-13 (1995).
- Hu, S.-Y., S. W. Corzine, K. K. Law, D. B. Young, A. C. Gossard, J. L. Merz, and L. A. Coldren, "Lateral carrier diffusion and surface recombination in InGaAs/AlGaAs quantum-well ridge-waveguide lasers," *J. Appl. Phys.*, vol. 76, pp. 4479-4487 (1995).
- Imamoglu, A., R. J. Ram, S. Pau, Y. Yamamoto, "Nonequilibrium condensates and lasers without inversion: exciton-polariton lasers," *Phys. Rev. A*, vol.53, no.6, pp. 4250-3 (1996)
- Keldysh, L.V., Kozlov, A. N., "Collective properties of excitons in semiconductors," *Sov. Phys. JETP*, vol. 27 no. 3, pp. 521-528 (1968).
- Lewenstein, M., L. You, J. Cooper, and K. Burnett, "Quantum field theory of atoms interacting with photons: foundations," *Phys. Rev. A*, vol.50, no.3, pp. 2207-31 (1994)
- Lin, J. -L., and J. P. Wolfe, "Bose-Einstein condensation of paraexcitons in stressed Cu_2O ," *Phys. Rev. Lett.*, vol. 71, no. 8, pp. 1222-5 (1993)
- Loudon, R., *The Quantum Theory of Light*. Oxford: Oxford University Press (1992).
- Mohideen, U., W. S. Hobson, S. J. Pearton, F. Ren, R. E. Slusher, "GaAs/AlAs microdisk lasers," *Appl. Phys. Lett.*, vol. 64, no.15, pp. 1911-1913 (1994).

- Paquet, D., T. M. Rice, K. Ueda, "Two-dimensional electron-hole fluid in a strong perpendicular magnetic field: exciton Bose condensate or maximum density two-dimensional droplet," *Phys. Rev. B*, vol. 32, no.8, pp. 5208-21 (1985).
- Pau, S., H. Cao, J. Jacobson, G. Bjork, Y. Yamamoto, and A. Imamoglu, "Observation of a laserlike transition in a microcavity exciton polariton system," *Phys. Rev. A*, vol.54, no.3, pp. R1789-92 (1996)
- Peters, M. G., B. J. Thibeault, D. B. Young, A. C. Gossard, and L. A. Coldren, "Growth of beryllium doped AlGaAs/GaAs mirrors for VCSELs," *J. Vac. Technol. B*, vol. 12, no. 6, pp. 3075-3083 (1994).
- Purcell, E. M., "Spontaneous emission probabilities at radio frequencies," *Phys. Rev.*, vol. 69, no. , p. 681 (1946).
- Ram, R. J., D. I. Babic, R. A. York and J. E. Bowers, "Spontaneous emission in microcavities with distributed mirrors," *IEEE J. of Quant. Electron.*, vol. 31, no. 2, (1995).
- Ram, R. J., E. Goobar, M. Peters, L. A. Coldren and J. E. Bowers "Spontaneous emission factor in post microcavity lasers," *IEEE Photon. Tech. Lett.*, vol. 8, no. 5, pp. 599-601 (1996).
- Ram, R. J., R. A. York, "Parametric oscillation in non-linear dipole arrays," *IEEE Trans. on Antennas and Propagat.*, vol.42, no.3, pp. 406-11 (1994).
- Rice, P.R. and H. J. Carmichael, "Photon statistics of cavity-QED laser: A comment on laser-phase transition analogy," *Phys. Rev. B*, vol. 50, pp. 4318-4329 (1994).
- Savona, V., L. C. Andreani, P. Schwendimann, and A. Quattropania, "Quantum well excitons in semiconductor microcavities: unified treatment of weak and strong coupling regimes," *Solid State Comm.*, vol.93, no.9, pp. 733-9 (1995).
- Schmitt-Rink, S., D. S. Chemla, and D. A. B. Miller, "Theory of transient excitonic optical nonlinearities in semiconductor quantum-well structures," *Phys. Rev. B* , vol. 32, pp. 6601-6609 (1985).
- Schmitt-Rink, S., J. B. Stark, W. H. Knox, D. S. Chemla, W. Schafer, "Optical properties of quasi-zero-dimensional magneto-excitons," *App. Phys. A*, vol. 53, no.6, pp.491-502 (1991).
- Shtengel, G., H. Temkin, T. Uchida, M. Kim, P. Brusenbach, and C. Parsons, "Spontaneous emission factor and its scaling in vertical cavity surface emitting lasers," *Appl. Phys. Lett.*, vol. 64, no. 9, pp. 1062-4 (1994).

- Shubair, R. M., and Y. L. Chow, "A closed-form solution of vertical dipole antennas above a dielectric half-space," *IEEE Trans. Antennas. Propagat.*, vol. 41, no. 12, pp. 1737-1740 (1993).
- Siegman, A., *Lasers*, Mill Valley, Calif.: University Science Books (1986).
- Stanley, R.P., R. Houdre, C. Weisbuch, U. Oesterle, and M. Ilegems, "Cavity-polariton photoluminescence in semiconductor microcavities: experimental evidence," *Phys. Rev. B*, vol.53, no.16, pp. 10995-1007 (1996)
- Tassone, F., C. Piermarocchi, V. Savona, A. Quattropani, and P. Schwendimann, "Photoluminescence decay times in strong-coupling microcavities," *Phys. Rev. B*, vol. 53, pp. R7642-7645 (1996).
- Thibeault, B., T. A. Strand, M. G. Peters, T. Wipejowski, D. B. Young, J. W. Scott, and L. A. Coldren, "Limitations of surface related optical and carrier losses in microcavity lasers," *J. Appl. Phys.* (1995).
- Thompson, R.J.; G. Rempe, and H. J. Kimble, "Observation of normal-mode splitting for an atom in an optical cavity," *Phys. Rev. Lett.*, vol.68, no.8, 1132-5 (1992).
- Tikhodeev, S.G., "Bose-condensation of finite-lifetime particles with excitons as an example," *Sov. Phys. JETP*, vol. 70, pp. 380-387 (1990).
- Vinattieri, A, J. Shah, T. C. Damen, L. N. Kim, Pfeiffer, M. Z. Maialle, L. J. Sham, "Exciton dynamics in GaAs quantum wells under resonant excitation," *Phys. Rev. B*, vol. 50, no.15, pp. 10868-79 (1994).
- Vurgaftman, I., and J. Singh, "Steady-state and transient characteristics of microcavity surface-emitting lasers with compressively strained quantum-well active regions," *IEEE J. Quantum Electron.*, vol. 31, no. 5, pp. 852-863 (1995).
- Wang, H., J. Shah, T. C. Damen, and L. N. Pfeiffer, "Spontaneous emission of excitons in GaAs quantum wells: the role of momentum scattering," *Phys. Rev. Lett.*, vol.74, no.15, pp. 3065-8 (1995)
- Weisbuch, C., M. Nishioka, A. Ishikawa, Y. Arakawa, "Observation of the coupled exciton-photon mode splitting in a semiconductor quantum microcavity," *Phys. Rev. Lett.*, vol. 69, no.23, pp. 3314-17 (1992).
- Weisbuch, C., B. Vinter, *Quantum semiconductor structures: fundamentals and applications*. Boston: Academic Press, (1991).
- Yamanoto, Y., S. Machida, K. Igeta, G. Bjork, "Controlled Spontaneous emission in microcavity semiconductor lasers," Y. Yamamoto, ed., *Coherence, Amplification and Quantum Effects in Semiconductor Lasers*. New York.: John Wiley (1991).

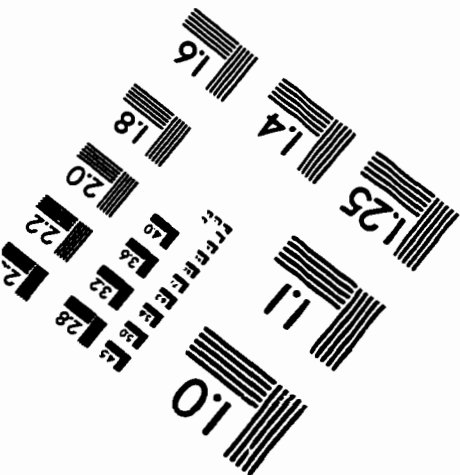
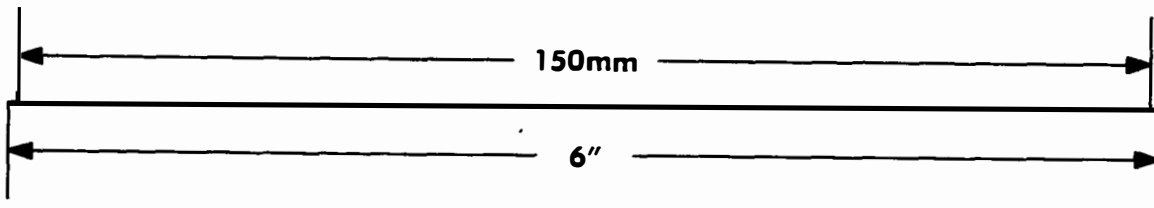
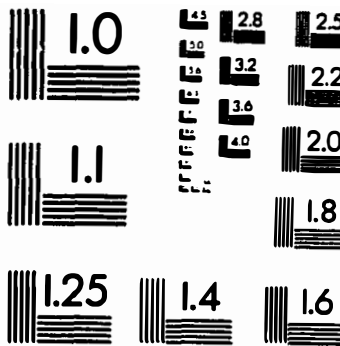
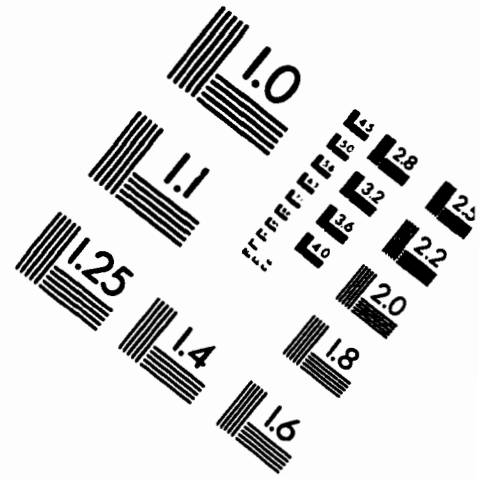
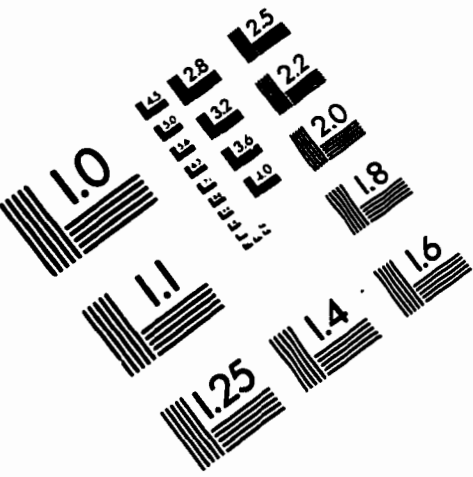
Yeh, P., *Optical Waves in Layered Media*. New York: John Wiley & Sons (1991).

Yokoyama, H., K. Nishi, T. Anan, Y. Nambu, E. Ippen, Brorson, "Controlling spontaneous emission and threshold-less laser operation with optical microcavities," *Optical and Quantum Electron.*, vol. 24, no. 2, pp. S245-S272 (1992).

Yura, F. and E. Hanamura, "Coherent light emission from condensing polaritons," *Phys. Rev. B*, vol. 50, no.20, pp. 15457-60 (1994).

Zhao, B., T. R. Chen, L. E. Eng, Y. H. Zhaung, A. Shakouri, and A. Yariv, "Sub μ A current operation of strained InGaAs quantum well laser at low temperature," *Appl. Phys. Lett.*, vol. 65, no.14, pp. 1805-7 (1994).

IMAGE EVALUATION TEST TARGET (QA-3)



APPLIED IMAGE, Inc
 1653 East Main Street
 Rochester, NY 14609 USA
 Phone: 716/482-0300
 Fax: 716/288-5989

© 1983, Applied Image, Inc.. All Rights Reserved

